

Semileptonic decays of heavy+light pseudoscalar mesons

by
Zhao-Qian Yao (姚照千)

Supervised by
Professor Craig D. Roberts

A dissertation submitted to
the graduate school of Nanjing University
in partial fulfilment of the requirements for the degree of
DOCTOR OF PHILOSOPHY
in
Theoretical Physics



Department of Physics
Nanjing University

May 2, 2022

The first page paper for abstract of Nanjing University dissertation

THESIS: Semileptonic decays of heavy+light pseudoscalar mesons

SPECIALIZATION: Theoretical Physics

POSTGRADUATE: Zhao-Qian Yao (姚照千)

MENTOR: Professor Craig D. Roberts

ABSTRACT

Quantum chromodynamics (QCD) is a fundamental theory about strong interactions which is employed to study the physics of hadrons. Different from Quantum Electrodynamics (QED), which calculations can reliably be completed using perturbation theory at accessible energies, QCD is non-perturbative in the low energy domain, bringing difficulties as well as many interesting phenomena. There are two typical features of low energy QCD: color confinement and dynamical chiral symmetry breaking (DCSB), which make it a challenging work to describe non-perturbative QCD. In the work described herein, we employed the Dyson-Schwinger equations (DSEs) which provide a symmetry-preserving, nonperturbative continuum framework for the systematic analyses of hadron observables. DSEs are a system of coupled integral equations, which link all of a theory's Green functions.

One particular field of intense interest encompasses hadron semileptonic decays, which have long played a crucial role in testing the Standard Model and constraining its parameters. For instance, such decays are widely exploited to determine the elements of the Cabibbo-Kobayashi-Maskawa (CKM) quark-flavour mixing matrix. The calculation of hadron semileptonic decays, however, requires good knowledge of hadron structure.

In this work, DSEs are used to deliver Poincaré invariant predictions for properties of light+light, heavy+light, and heavy+heavy mesons. This approach has been employed successfully by many practitioners to provide a unified explanation for the properties of hadrons with 0 – 3 heavy quarks, viz. from the lightest (almost) Nambu-

Goldstone bosons to triply heavy baryons. Each semileptonic transition is conventionally characterized by the value of the dominant form factor and we present predictions for transition form factors and decay widths for heavy+light mesons, including $B_{(s)} \rightarrow \pi(K), D_s \rightarrow K; D \rightarrow \pi, K$ and $B_c \rightarrow \eta_c, J/\Psi$. The form factors are a leading source of uncertainty in all such calculations: our results agree quantitatively with available data and provide benchmarks for the hitherto unmeasured $D_s \rightarrow K^0, \bar{B}_s \rightarrow K^+$ form factors. The analysis delivers a value of $|V_{cs}| = 0.974(10)$ and also predictions for all branching fraction ratios in the pseudoscalar meson sector that can be used to test lepton flavour universality. Quantitative comparisons are provided between extant theory and the recent measurement of $\mathcal{B}_{B_s^0 \rightarrow K^- \mu^+ \nu_\mu}$. Here, further, refined measurements would be useful in moving toward a more accurate value of $|V_{ub}|$.

Continuing with the theme of lepton flavor universality, we calculated the branching fractions for $B_c \rightarrow \eta_c, J/\Psi$, using which the following values of the ratios for τ over μ final states are obtained: $R_{\eta_c} = 0.313(22)$ and $R_{J/\psi} = 0.242(47)$. Our analysis confirms a 2σ discrepancy between the Standard Model prediction for $R_{J/\psi}$ and the single available experimental result.

Contents

Abstract	i
Contents	iii
Figure lists	v
Table lists	ix
1 Introduction	1
1.1 Background	1
1.2 Dyson-Schwinger equations	5
1.3 Semileptonic decays and the CKM matrix	7
2 Dyson-Schwinger equations	9
2.1 The gap equation	9
2.2 Bethe-Salpeter equation	16
3 Semileptonic decay for pseudoscalar meson final state	21
3.1 Introduction	21
3.2 Semileptonic transitions	21
3.3 Transition form factors	27
3.3.1 $K^+ \rightarrow \pi^0$	27
3.3.2 $D^0 \rightarrow \pi^-, D_s^+ \rightarrow K^0, D^0 \rightarrow K^-$	28
3.3.3 $\bar{B}^0 \rightarrow \pi^+, \bar{B}_s^0 \rightarrow K^+$	32
3.4 Remarks	35
4 Semileptonic B_c to η_c and J/ψ transitions	37
4.1 Introduction	37
4.2 Transition form factors: definitions	38
4.3 Transition form factors: matrix elements	40
4.4 Computational scheme and results	41
4.5 Transition form factors: predictions and comparisons	44
5 Conclusions and outlook	51
5.1 Conclusions	51
5.2 Outlook	52

5.2.1 Semileptonic transitions of vector meson final states	52
5.2.2 Baryons	52
A Euclidean conventions	55
A.1 Dirac structures	55
A.2 Coordinates	56
B Solving the Bethe-Salpeter equation	57
B.1 Dressed-quark propagators in the complex plane	57
B.2 The Bethe-Salpeter equation in the rest frame	57
B.3 Bethe-Salpeter equation in the moving frame	60
C Schlessinger Point Method	63
C.1 Introduction of Schlessinger Point Method	63
C.2 Examples	63
References	65
Acknowledgements	77
CURRICULUM VITAE	79

Figure lists

1-1	Semileptonic decay of $K^0 \rightarrow \pi^- l^+ \bar{\nu}_l$	1
1-2	Standard model of elementary particles (Image from https://en.wikipedia.org/wiki/File:Standard_Model_of_Elementary_Particles.svg).	3
1-3	Feynman diagrams for the W -mediated decay of a meson which is built from quarks $Q\bar{q}$: (a) semileptonic decay, (b) leptonic decay, (c) hadronic decay whose final states are $\bar{q}q'$ and $\bar{q}_i q_j$ and (d) hadronic decay whose final states are $\bar{q}q_j$ and $\bar{q}_i q'$. For brevity and clarity, we didn't show the exchanges of gluons between the quarks in these feynman diagrams.	4
1-4	QCD's process-independent running-coupling, $\hat{\alpha}(k^2)/\pi$, obtained by combining the best available results from continuum and lattice analyses [1] (image from [2].)	4
1-5	Quark Dyson-Schwinger equation (gap equation). The line with the red ball is the dressed quark propagator; the blue ball is the dressed-quark-gluon vertex; the line with the green ball is the dressed-gluon propagator.	5
1-6	Inhomogeneous Bethe-Salpeter equation for a typical quark+antiquark-hadron vertex. The blue ball means the dressed vertex, and the line with red ball is dressed quark propagator. K is the two particle irreducible quark+antiquark scattering kernel.	6
1-7	Homogeneous Bethe-Salpeter equation for two-body bound states.	6
1-8	Faddeev equation for three-body bound states.	6
2-1	Comparison of $A(p^2)$ at different values of the renormalization point. ..	14
2-2	Comparison of $B(p^2)$ at different values of the renormalization point. We can see $A(p^2)$ and $B(p^2)$ decrease as q^2 increases and this meets the requirement of asymptotic freedom.	14
2-3	Comparison of the mass function and we can see the mass function is renormalization point independent.	14
2-4	Comparison of $A(p^2)$ at different current quark masses.	15
2-5	Comparison of $B(p^2)$ at different current quark masses.	15
2-6	Comparison of the mass function $M(p^2)$ at different current quark masses.	15
2-7	This figure shows the evolution of masses of pseudoscalar and vector mesons with the renormalization group invariant current masses.	19
2-8	Comparison between the two sides of Eq. (2-33).	19

2-9	Inhomogeneous Bethe-Salpeter equation for the weak interaction vector vertex in rainbow-ladder truncation.	20
3-1	The Semileptonic decay of $\bar{B}_s^0 \rightarrow K^+ \ell^- \bar{\nu}_\ell$	22
3-2	The impulse approximation for the semileptonic transition.	23
3-3	$K \rightarrow \pi$ transition form factors, normalised by their $t = 0$ values: $f_+^{K_u}$, solid blue curve; and $f_0^{K_u}$, long-dashed purple curve. Comparison curves within like coloured bands are linear fits to available data described in Ref. [3]: $f_+^{K_u}$, dot-dashed green; and dashed red $f_0^{K_u}$	29
3-4	Transition form factors of $D \rightarrow \pi$. Left panel- A. Data: black stars [4]; purple up-triangles [5]; green gray squares [6]; and down-triangles [7]. Right panel- B. f_0 is depicted as the dark-red squares from [8]. Legend: f_+ is depicted as the solid blue curve and f_0 as the long-dashed grey curve; and the like-coloured shaded bands represent the SPM uncertainty.	30
3-5	Transition form factors of $D_s^+ \rightarrow K^0$. Sole available datum from Ref. [9]. f_+ is depicted as the blue curve and f_0 as the dashed grey curve.	31
3-6	$D \rightarrow K$ transition form factors. Left panel- A. Data: black stars [4]; gray squares [5] and green down-triangles [7]. Right panel- B. f_0 is depicted as the dark-red up-triangles from [8]. Legend: f_+ is depicted as the solid blue curve and f_0 as the long-dashed grey curve.	31
3-7	Transition form factors of $\bar{B}^0 \rightarrow \pi^+$: f_+ - solid blue curve; f_0 - long-dashed grey curve; and the like-coloured shaded bands represent the SPM uncertainty. IQCD results: red squares in both panels come from [27]. Left panel - A. Data: green stars reconstructed from the average [Ref. [10], Tab.81] of data reported in Refs. [11-14].	32
3-8	Transition form factors of $\bar{B}_s^0 \rightarrow K^+$. f_+ - solid blue curve; f_0 - long-dashed grey curve. IQCD results: green up-triangles [15] and red squares [16] in both panel.	33

3-9	<i>Top panel</i> – A. Branching fraction $\mathcal{B}_{\bar{B}_s^0 \rightarrow K^+ \mu^- \bar{\nu}_\mu}$ computed herein, “H”, compared with the value in Eq. (3-15), “E”, viz. a measurement of $\mathcal{B}_{B_s^0 \rightarrow K^- \mu^+ \nu_\mu}$ [17] and some results obtained using other means: continuum I – III [18-20]; and lattice IV – VI [15-16, 21]. <i>Bottom panel</i> – B. Branching fraction ratio $\mathcal{B}_{\bar{B}_s^0 \rightarrow K^+ \tau^- \bar{\nu}_\tau} / \mathcal{B}_{\bar{B}_s^0 \rightarrow K^+ \mu^- \bar{\nu}_\mu}$ computed herein compared with some results obtained using other means. Legend as in Panel A, except “P(E)” is the result from [22], which is an estimate constrained by the datum in Ref. [17]. Both panels – Grey line and like-coloured band: unweighted mean of theory results and related uncertainties. Green dashed line and green band: uncertainty-weighted average of theory results and associated uncertainty.	35
4-1	Ratio $R_{J/\psi}$ in Eq. (4-1) – red circle, empirical result from LHCb Collaboration [23]; blue star – our prediction; grey square – IQCD result [24-25]; and gold band – unweighted mean of central values from contemporary calculations [26-31].	38
4-2	Predicted values of all transition form factors at the maximum recoil point ($t = 0$) - blue stars. Comparisons: IQCD results [25, 32] - grey squares; and unweighted average of each column in Table. 4-4 -red circles.	45
4-3	Predicted $B_c \rightarrow \eta_c$ semileptonic transition form factors. (The shaded bands surrounding each curve express the SPM uncertainty, determined as discussed in the paragraph before that containing Eq. (4-11).) The points in both panels are preliminary IQCD results from Ref. [32].	46
4-4	Predicted $B_c \rightarrow J/\psi$ semileptonic transition form factors – solid blue curves within like-coloured bands, which express the 1σ uncertainty on our SPM results. Comparable IQCD results from Ref. [25] – dashed grey curves within like-coloured bands.	48
B-1	Domain of the complex plane sampled by the dressed-quark propagator.	58
B-2	Evolution with p^2 of the eigenvalues of Eq. B-10 for pion and ρ -meson channels.	59
B-3	$\zeta_m^i(p^2)$ from the pion’s BS amplitudes. Here, we employ a convenient normalization for the zeroth Chebyshev moment by setting $T_0 = 1/\sqrt{2}$ [33].	61
B-4	Pion elastic form factor obtained via two methods introduced above. The interpolation points are given by Eq. (B-16) - analytic continuation; and the curve is obtained from Eq. (B-15) - direct solution.	62

- C-1 Comparison between the function curve and the SPM interpolation.
The green points are the input data extracted from the function curve;
the red dashed line is the interpolation result from SPM. 64
- C-2 Extrapolations in two directions: A. Fix the mass of light quark c and
increase the mass of the other quark, initiating from the value of c quark
mass (SPM (I)); B. Fix the mass of heavy quark b and decrease the mass
of the other quark, initiating from the value of b quark mass (SPM (II)). 64

Table lists

3-1	Static properties of light mesons related to the transitions considered herein, calculated using the current-quark masses in Eq. (3-8). For comparison and where available, values recorded by the particle data group (PDG) [3] are also listed. The mean absolute relative error between central values is 2(2)%.	25
3-2	All results are calculated using the SPM and the current-quark masses in Eq. (3-9). Each listed uncertainty expresses a 1σ confidence level on the SPM extrapolation, i.e., 68% of all SPM approximants give values that lie within the indicated range. The values recorded by the PDG [3] are also listed here. (All quantities in GeV.)	26
3-3	Interpolation parameters for each form factor considered in this chapter, as labelled: Eq. (3-10), α_1 is dimensionless and $\alpha_{2,3}$ have dimension GeV^{-1} . N.B. Symmetry constraints, manifest in our treatment, ensure $\alpha_1^+ = \alpha_1^0$ for all transitions; and as plain from Eq. (3-10), $f_{+,0}(t=0) = \alpha_1^+$. (The SPM uncertainty estimate is discussed in the paragraph after that containing Eq. (3-9).)	28
3-4	Pseudoscalar meson semileptonic branching fractions: each such fraction is to be multiplied by 10^{-3} . The column labelled “ratio” is the ratio of the preceding two entries in the row, so no factor of 10^{-3} is applied in this column. PDG [3] lists the following values for the CKM matrix elements: $ V_{us} = 0.2245(8)$, $ V_{cd} = 0.221(4)$, $ V_{cs} = 0.987(11)$ $ V_{ub} = 0.00382(24)$; and the following lifetimes (in seconds): $\tau_{K^+} = 1.2379(21) \times 10^{-8}$, $\tau_{D^0} = 4.10 \times 10^{-13}$, $\tau_{D_s^\pm} = 5.04 \times 10^{-13}$, $\tau_{\bar{B}^0} = 1.519 \times 10^{-12}$, $\tau_{\bar{B}_s^0} = 1.515 \times 10^{-12}$. All kinematic factors are evaluated using PDG values for meson masses.	29
4-1	Static properties of mesons evaluated using bound-state equations. Normalisation: the empirical value of the pion leptonic decay constant is $f_\pi \approx 0.092 \text{ GeV}$. Empirical values (expt.), where available, drawn from Ref. [3]; and lattice-QCD (lQCD) results for leptonic decay constants from Refs. [34-36]. The mean absolute relative error between our predictions and empirical results is 3.6%. (All dimensioned quantities in GeV.)	41

- 4-2 This table shows SPM interpolation parameters for each transition form factor considered in this chapter, as labelled: Eq. (4-12), α_1 is dimensionless and $\alpha_{2,3}$ have dimension GeV^{-1} . α_i^x represents the parameter α_i for $x(t)$ where $i = 1, 2, 3$ and $x = f_+, f_-, A_0, A_1, A_2, V$. (The SPM uncertainty estimate is discussed in the paragraph before that containing Eq. (4-11)). 42
- 4-3 SPM predictions for meson masses (in GeV) that determine the locations of the timelike pole in the transition form factors computed herein, Eq. (4-12). These masses have not yet been measured; so, we present IQCD results for context [37]. (The SPM uncertainty estimate is discussed in the paragraph before that containing Eq. (4-11).) 42
- 4-4 Maximum recoil ($t = 0$) value of each transition form factor calculated in this chapter. Comparisons are provided with other recent analyses: quark model (QM) [26-27]; phenomenology (ph) [28]; sum rules (SR) [29] modelling based on perturbative QCD (mpQCD) [30]; Salpeter equation (iBS) [31]; and IQCD [25, 32]. As additional context, we list unweighted average values for each of the quantities, evaluated with our prediction excluded (mean-e) and included (mean-i). 45
- 4-5 Branching fractions calculated using our predictions for the semileptonic transition form factors in Eqs. (4-6)-(4-8) and empirical lepton and meson masses: (A) - $B_c \rightarrow \eta_c$; and (B) - $B_c \rightarrow J/\psi$. Two uncertainties are listed with our results: first - 1σ SPM uncertainty; second - from error on $|V_{cb}|$. Column 3 reports the ratio of the first two columns: $|V_{cb}|$ cancels. Comparisons are provided with other analyses: quark model (QM) [26-27]; phenomenology (ph) [28]; sum rules (SR) [29] modelling based on perturbative QCD (mpQCD) [30]; Salpeter equation (iBS) [31]; and IQCD [24-25]. (No IQCD results are available for inclusion in Panel A.) As additional context, we list an unweighted average value for each quantity, evaluated with our prediction excluded (mean-e) and included (mean-i). Branching fractions are to be multiplied by 10^{-3} 47

Chapter 1 Introduction

1.1 Background

In the study of hadron physics, semileptonic decays of mesons play a crucial role, the final-state particles in which include a single charged lepton, a neutrino and a lighter meson. Semileptonic decays, from a theoretical perspective, combine strong and weak interactions and can provide access both to the measurement of fundamental standard-model parameters, e.g., Cabibbo-Kobayashi-Maskawa (CKM) matrix, and to the understanding of quantum chromodynamics (QCD).

As is well known in history, the semileptonic process of nuclear β decay led people to the era of weak-interaction physics, which allowed physicists to explore the secret of the undetected partner of the electron, the neutrino. The W -boson-mediated weak transition $d \rightarrow u W^-$, $W^- \rightarrow e^- \bar{\nu}_e$, which underlies the β decay, transforms a neutron (udd) into a proton (uud) via the decay of a d quark into a u quark. β decay was the only known weak process until the 1940s, when muons, pions, and kaons were found in cosmic rays.

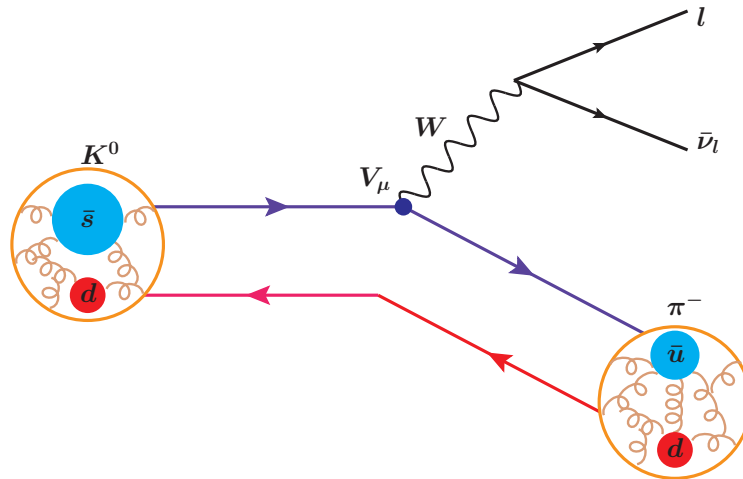


Fig. 1-1: Semileptonic decay of $K^0 \rightarrow \pi^- l^+ \bar{\nu}_l$

With accelerators in many laboratories being improved rapidly, more and more

scientists were attracted to the research of weak decays. For instance, the process $K^0 \rightarrow \pi^- l^+ \bar{\nu}_l$ presented the similarity between the kaon decay and the β decay of nucleons: the strange quark (s) in kaon undergoes the decay $s \rightarrow u W^-$, $W^- \rightarrow e^- \bar{\nu}_e$ as depicted in Fig. 1-1.

In the 1970s, two heavy quarks, charm(c) [38-39] and bottom (b) [40], along with a heavy lepton, τ were discovered [41]. These findings brought people to the mystery of the generation puzzle [42]. Namely, indirect evidence for the top quark (t) from $B^0 \bar{B}^0$ mixing [43] were also found, which, together with the properties of the new heavy quarks, presented the existence of two pairwise-heavier versions of the basic pair of quarks (u, d). In 1995, the t quark was directly observed in pp collisions [44-45]. Thus, we have three quark generations:

$$\begin{pmatrix} u \\ d \end{pmatrix}, \begin{pmatrix} c \\ s \end{pmatrix}, \begin{pmatrix} t \\ b \end{pmatrix}. \quad (1-1)$$

The charge of the upper elements of each quark doublet is $+2/3$ (measured in units of e , with e denoting the positron charge), while the charge of the lower elements is $-1/3$. Quarks are found only in bound states, and such a bizarre phenomenon in QCD is called colour confinement, the understanding of which is a major problem that has existed since the birth of QCD. Much effort is currently being focused on solving this problem.

The three generations of leptons are listed below:

$$\begin{pmatrix} \nu_e \\ e^- \end{pmatrix}, \begin{pmatrix} \nu_\mu \\ \mu^- \end{pmatrix}, \begin{pmatrix} \nu_\tau \\ \tau^- \end{pmatrix}. \quad (1-2)$$

The charged lepton masses also arise with generation ($m_e = 0.0005 \text{ GeV}/c^2$, $m_\mu = 0.106 \text{ GeV}/c^2$, $m_\tau = 1.777 \text{ GeV}/c^2$. Neutrinos are now known to have mass [46-47], which lies outside the Standard Model, but those masses are neglected because they have no measurable impact on this work). These are the elementary particles which constitute the Standard Model Fig. 1-2. As discussed before, semileptonic decays

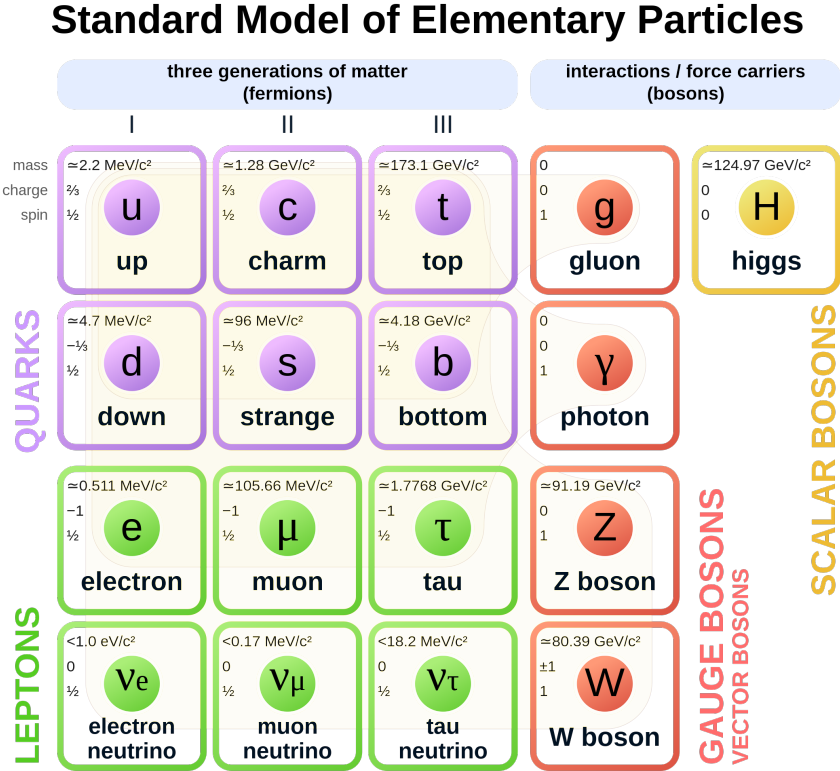


Fig. 1-2: Standard model of elementary particles (Image from https://en.wikipedia.org/wiki/File:Standard_Model_of_Elementary_Particles.svg).

of particles constituted from heavy quarks can be analogous to the nuclear β decay. Fig. 1-3(a) depicts the underlying quark-level transition of the semileptonic decay of a meson which contains a heavy quark denoted by Q . As a result, we can denote the process by $Q \rightarrow q'W, W \rightarrow \ell^- \bar{\nu}$ [Fig. 1-3(a)], while the transition is $Qq \rightarrow W \rightarrow \ell^- \bar{\nu}$ for leptonic decays [Fig. 1-3(b)]. Fig. 1-3(c) and Fig. 1-3(d) present examples of hadronic decays, where the decay products of W are quarks. Theoretically, the weak interactions underlying these processes can be described straightforwardly, but things become complicated since the quarks are bound together by the strong interaction. Described by QCD [48], these interactions are hard for people to make predictions with perturbative approaches due to the large coupling at the typical energy scales in these decays Fig. 1-4. So we seek for a nonperturbative tool – Dyson-Schwinger equations (DSEs), to describe the strong interactions of quarks inside the mesons.

With the discovery of heavy quarks, the research of the properties of heavy-light mesons have been widely considered, especially the studies of the semileptonic decays

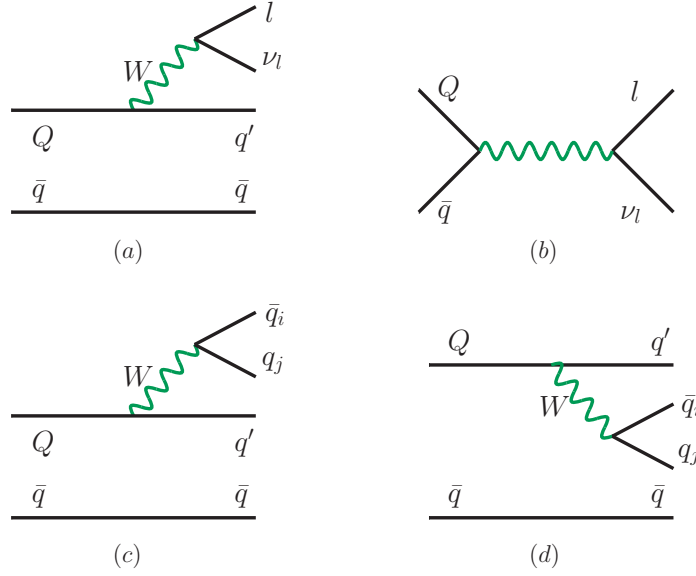


Fig. 1–3: Feynman diagrams for the W -mediated decay of a meson which is built from quarks $Q\bar{q}$: (a) semileptonic decay, (b) leptonic decay, (c) hadronic decay whose final states are $\bar{q}q'$ and $\bar{q}_i q_j$ and (d) hadronic decay whose final states are $\bar{q}q_j$ and $\bar{q}_i q'$. For brevity and clarity, we didn't show the exchanges of gluons between the quarks in these feynman diagrams.

of heavy-light mesons, because it provides a good viewpoint to look at the interference between the Higgs mechanism of Lagrangian-mass generation and emergent hadron mass (EHM), which provides the proton mass-scale and is thought to be understandable within QCD.

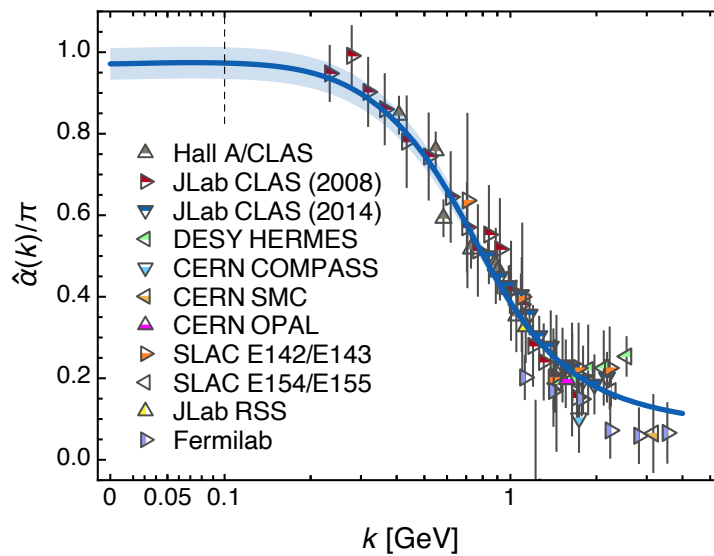


Fig. 1–4: QCD's process-independent running-coupling, $\hat{\alpha}(k^2)/\pi$, obtained by combining the best available results from continuum and lattice analyses [1] (image from [2].)

1.2 Dyson-Schwinger equations

QCD is a fundamental theory about strong interactions. Asymptotic freedom, one of the most important properties of QCD, describes the fact that the coupling (α_s) in the strong interaction runs with the energy scale. In large momentum scale, the coupling is relatively small, where the perturbative QCD performs very well and delivers good agreement with experiments. However, in the low energy domain, the coupling increases rapidly with decreasing momentum (see Fig. 1–4), which invalidates the perturbation expansion. Therefore, many effective theories and models have been used in the low energy domain to study strong interactions. At present, non-perturbative methods, including DSEs, lattice QCD (lQCD), QCD sum rule and quark model, etc., have been developing systematically. We employ the DSEs in this thesis because they are based on the basic principles of quantum field theory and can effectively test the applicability of QCD in low energy domain.

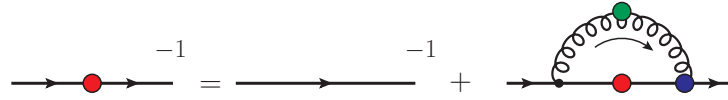


Fig. 1–5: Quark Dyson-Schwinger equation (gap equation). The line with the red ball is the dressed quark propagator; the blue ball is the dressed-quark-gluon vertex; the line with the green ball is the dressed-gluon propagator.

From the field equations of quantum field theory one can derive a system of coupled integral equations, which interrelates all of a theory's Green functions – DSEs. DSEs provide a nonperturbative continuum approach to QCD. In the past two decades, this method has developed rapidly and has been used successfully to expose the character of emergent phenomena in QCD, including the dynamical generation of a gluon mass-scale and dynamical chiral symmetry breaking [2] (DCSB). Many researchers have contributed to this field [49–51] and their efforts have brought this approach to the forefront of hadron physics and brought us closer to understanding the nature of QCD interactions and the formation of hadrons, and, more importantly, the origin of mass [2, 52].

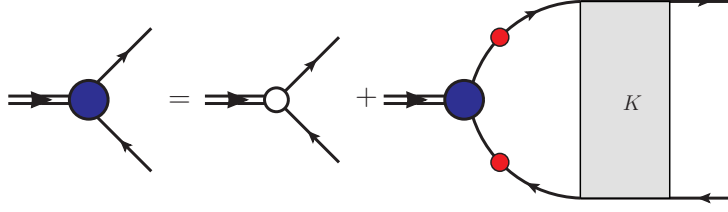


Fig. 1-6: Inhomogeneous Bethe-Salpeter equation for a typical quark+antiquark-hadron vertex. The blue ball means the dressed vertex, and the line with red ball is dressed quark propagator. K is the two particle irreducible quark+antiquark scattering kernel.

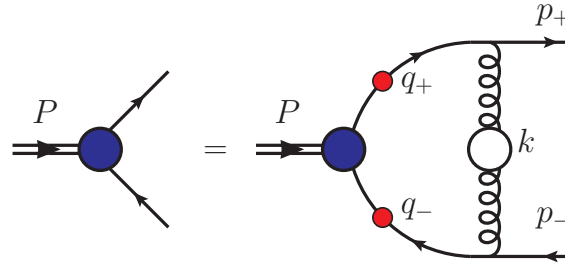


Fig. 1-7: Homogeneous Bethe-Salpeter equation for two-body bound states.

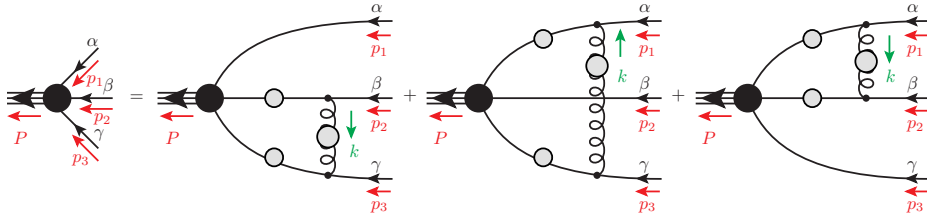


Fig. 1-8: Faddeev equation for three-body bound states.

The DSEs include, for example, the dressed quark propagator, which satisfies a gap equation like Fig. 1-5; the Bethe-Salpeter equation (BSE), describing two-body problems like Fig. 1-6 Fig. 1-7, and the Faddeev equation, which is relevant for three-body bound states, Fig. 1-8. To solve the DSEs, a truncation must be implemented. The renormalization group improved rainbow truncation of the quark DSEs combined with the associated ladder truncation of the BSEs is widely used, keeping the balance between simplicity and accuracy and this truncation has been employed successfully in the analyses of many hadron properties, such as distribution amplitudes (DAs) [53-54], parton distribution functions (PDFs) [55-56], elastic and transition form factors [57-58], etc.

1.3 Semileptonic decays and the CKM matrix

For the decay of a quark q with charge $-1/3$ to a quark q' with charge $+2/3$, the coupling at the W vertex is proportional to $gV_{q'q}$, where $V_{q'q}$ is generally a complex number. Hence the amplitudes of the processes $b \rightarrow c\ell^-\bar{\nu}$ and $b \rightarrow u\ell^-\bar{\nu}$ are proportional to V_{cb} and V_{ub} , respectively, and the amplitudes of $c \rightarrow s\ell^+\nu$ and $c \rightarrow d\ell^+\nu$ decays are proportional to V_{cs}^* and V_{cd}^* .

The 3×3 matrix of these constants, which is known as the Cabibbo-Kobayashi-Maskawa (CKM) matrix [59],

$$V = \begin{pmatrix} V_{ud} & V_{us} & V_{ub} \\ V_{cd} & V_{cs} & V_{cb} \\ V_{td} & V_{ts} & V_{tb} \end{pmatrix}$$

is a generalization of the Cabibbo rotation known since the 1960s [60]. Most of the known CKM elements have been measured via semileptonic decays as listed by the Particle Data Group (PDG) [3]. We make a quick summary here. $|V_{ud}| = 0.97370(10)$, the best determination of which comes from nuclear β decay [61], particularly from special transitions in which the uncertainties resulting from hadronic effects can be minimized. The value of $|V_{us}| (= 0.2245(8))$ is determined from kaon semileptonic decays K_{l3} [62-67] and hyperon semileptonic decays [68] with somewhat larger theoretical errors than $|V_{ud}|$. The magnitude of V_{cd} can be extracted from semileptonic charm decays. The average of the measurements of $D \rightarrow \pi\ell\nu$ decays by *BABAR* [6], *BESIII* [7, 69], *CLEO-c* [5], and *Belle* [4], combined with *lQCD* calculations, produces $|V_{cd}| = 0.2330(029)(133)$. For this value, the first uncertainty is from experimental measurements, while the second is the theoretical uncertainty of the corresponding form factor. Considering another two determinations of V_{cd} , the final estimate of V_{cd} by the PDG [3] is $0.221(4)$. The magnitude of V_{cs} can be determined from semileptonic D decays or leptonic D_s decays. The value $|V_{cs}| = 0.987(11)$ is obtained from averaging these two determinations. For the matrix element $|V_{cb}|$, the value $|V_{cb}| = (42.2(0.8)) \times 10^{-3}$ is determined from exclusive and inclusive semilep-

tonic decays of B mesons to charm. For $|V_{ub}|$, semileptonic decays $\bar{B} \rightarrow \pi \ell \bar{\nu}_\ell$ provide the best determination. Combining with inclusive decay, one finally obtains the value $|V_{ub}| = (3.82(0.24)) \times 10^{-3}$. Hence, with the analyses above, one can draw a conclusion that semileptonic decays play a crucial role in the determination of the CKM elements.

Chapter 2 Dyson-Schwinger equations

In this chapter, we will present the basic framework and the solution schemes of the Dyson-Schwinger equations (DSEs). Solution strategies and algorithms are discussed in the following sections. Sec. 2.1 provides the general form of the quark propagator and introduces an interaction model which is widely used, along with the renormalization scheme employed herein. In Sec. 2.2, we analyse the homogeneous and inhomogeneous vertex Bethe-Salpeter equations (BSEs), which are a natural extension of the Green function formalism to bound-state problems.

2.1 The gap equation

In Euclidean space (i.e., see Appendix A), the quark propagator satisfies the Dyson-Schwinger equation, shown in Fig. 1–5. The formula takes the following form :

$$S^{-1}(p) = Z_2(i\gamma \cdot p + m_f^{bm}(\Lambda^2)) + \int_q^\Lambda g^2 D_{\mu\nu}(p-q) \frac{\lambda^a}{2} \gamma_\mu S(q) \Gamma_\nu^a(q, p), \quad (2-1)$$

where Γ_ν^a is the dressed-quark-gluon vertex, $D_{\mu\nu}$ is the dressed-gluon propagator, \int_q^Λ is a symbol representing a Poincaré invariant regularization of the four-dimensional integral, with Λ the regularization mass scale, and $m_f^{bm}(\Lambda)$ is the Λ -dependent current-quark bare mass, and $Z_2(\zeta^2, \Lambda^2)$ is the quark wave-function renormalization constant, with ζ the renormalization point. $Z_m(\zeta^2, \Lambda^2)$ is the mass renormalization constant, which satisfies $m_f^\zeta = Z_m(\zeta^2, \Lambda^2) m_f^{bm}(\Lambda^2)$, where m_f^ζ is the ζ -dependent current-quark mass. The following relation can be obtained:

$$Z_2(\zeta^2, \Lambda^2) m_f^{bm}(\Lambda^2) = Z_4(\zeta^2, \Lambda^2) m_f^\zeta. \quad (2-2)$$

The dressed-quark propagator is obtained by solving the quark gap equation and takes the form

$$S^{-1}(p) = \frac{1}{Z(p^2, \zeta^2)}(i\gamma \cdot p + M(p^2, \zeta^2)) = i\gamma \cdot p A(p^2, \zeta^2) + B(p^2, \zeta^2). \quad (2-3)$$

wherein the mass function $M(p^2) = B(p^2, \zeta^2)/A(p^2, \zeta^2)$ is renormalization point independent. The scalar functions $A(p^2, \zeta^2)$ and $B(p^2, \zeta^2)$ are solutions of Eq. (2-1). In the following part we will introduce more details and some numerical techniques to solve the gap equation for quark propagators.

Since DSEs are an infinite tower of coupled integral equations, they must be truncated at some point. We apply here the so called renormalization group improved “rainbow approximation”, wherein we absorb into the interaction all corrections to the leading term in the vertex:

$$\Gamma_\nu^a \rightarrow \frac{\lambda^a}{2} \gamma_\nu. \quad (2-4)$$

This approximation is widely used because it is known and understood to be accurate in applications to light-quark ground-state vector and isospin-nonzero-pseudoscalar mesons. Corrections to the leading Dirac structure of the vertex and from gauge sector interactions are absorbed into the renormalization group improved interaction. We employ the Qin-Chang form [70], which can be written as follows:

$$g^2 D_{\mu\nu}(k) = \mathcal{G}(k^2) T_{\mu\nu}(k), \quad (2-5)$$

with $k^2 T_{\mu\nu}(k) = k^2 \delta_{\mu\nu} - k_\mu k_\nu$ and $(u = k^2)$,

$$\frac{1}{Z_2^2} \mathcal{G}(u) = \frac{8\pi^2 D}{\omega^4} e^{-u/\omega^2} + \frac{8\pi^2 \gamma_m \mathcal{F}(u)}{\ln \left[\tau + \left(1 + u/\Lambda_{\text{QCD}}^2 \right)^2 \right]}, \quad (2-6)$$

where $\gamma_m = 4/\beta_0$, $\beta_0 = 11 - (2/3)n_f$, $n_f = 4$, $\Lambda_{\text{QCD}} = 0.234 \text{ GeV}$, $\tau = e^2 - 1$ ($\ln e = 1$), and $\mathcal{F}(u) = \{1 - \exp(-u/[4m_t^2])\}/u$, $m_t = 0.5 \text{ GeV}$. The development of Eqs. (2-5) and (2-6) is reviewed in Ref. [70], and their relation to QCD is introduced in Ref. [71].

With above definitions and approximations, we can now solve the gap equation

numerically. First we rewrite Eq. (2-1) as follows

$$S^{-1}(p) = Z_2 i\gamma \cdot p + Z_4 m_f^\zeta + \Sigma(p, \Lambda), \quad (2-7)$$

wherein $\Sigma(p, \Lambda)$ is the quark self-energy and takes the form

$$\Sigma(p, \Lambda) = Z_2^2 \int_q^\Lambda \frac{\mathcal{G}((p-q)^2)}{(p-q)^2} \frac{\lambda^a}{2} \gamma_\mu S(q) \frac{\lambda^a}{2} \gamma_\nu T_{\mu\nu}(p-q). \quad (2-8)$$

Next, we will introduce the renormalization scheme for solving Eq. (2-7). The starting point of our renormalization is asymptotic freedom, which is one of the most important properties of QCD. That means at large space-like momentum point ζ^2 , we require

$$S^{-1}(p)|_{p^2=\zeta^2} = i\gamma \cdot p + m_f^\zeta. \quad (2-9)$$

Through comparison with Eq. (2-3), the renormalization condition can be readily obtained as follows:

$$\begin{aligned} A(\zeta^2) &= 1, \\ B(\zeta^2) &= m_f^\zeta. \end{aligned} \quad (2-10)$$

In this work, a mass-independent momentum-subtraction renormalization scheme is employed, with each renormalization constant fixed in the chiral limit. However, since the chiral limit will lead to a trivial solution $B(\zeta^2) = 0$, the first derivative of $S^{-1}(p)$ with respect to current-quark mass is taken:

$$\begin{aligned} \frac{\partial S^{-1}(p)}{\partial m_f^\zeta} &= i\gamma \cdot p \frac{\partial A(p^2)}{\partial m_f^\zeta} + \frac{\partial B(p^2)}{\partial m_f^\zeta} \\ &= i\gamma \cdot p C(p^2) + D(p^2), \end{aligned} \quad (2-11)$$

where $C(p^2) = \frac{\partial A(p^2)}{\partial m_f^\zeta}$; $D(p^2) = \frac{\partial B(p^2)}{\partial m_f^\zeta}$. Note that $C(p^2), D(p^2)$ are introduced here to calculate the renormalization constant. Taking the first derivative of Eq. (2-7) with respect to current-quark mass, then through comparison with Eq. (2-11), we obtain the

following expressions:

$$i\gamma \cdot p C(p^2) + D(p^2) = Z_4 + Z_2^2 \int_q^\Lambda \frac{\mathcal{G}((p-q)^2)}{(p-q)^2} \times \frac{\lambda^a}{2} \gamma_\mu \frac{\partial S(q)}{\partial m_f^\zeta} \frac{\lambda^a}{2} \gamma_\nu T_{\mu\nu}(p-q), \quad (2-12)$$

along with

$$\begin{aligned} \frac{\partial S(q)}{\partial m_f^\zeta} &= \partial \left(\frac{1}{S(q)^{-1}} \right) / \partial m_f^\zeta \\ &= -S(q) [i\gamma \cdot p C(p^2) + D(p^2)] S(q). \end{aligned} \quad (2-13)$$

To obtain the four scalar functions, we project Eq. (2-7) and Eq. (2-12) on two tensor structures, \mathbf{I}_D and $-i\gamma \cdot p$ respectively, and insert Eq. (2-8). In total,

$$\begin{aligned} A(p^2) &= Z_2 + Z_2^2 \frac{4}{3p^2} \int_q^\Lambda \frac{\mathcal{G}(k^2)}{k^2} \frac{A(q^2)}{q^2 A(q^2) + B(q^2)} \left(p \cdot q + 2 \frac{(k \cdot p)(k \cdot q)}{(p-q)^2} \right), \\ B(p^2) &= Z_4 m(\zeta^2) + Z_2^2 4 \int_q^\Lambda \frac{\mathcal{G}(k^2)}{k^2} \frac{B(q^2)}{q^2 A(q^2) + B(q^2)}, \\ C(p^2) &= Z_2^2 \frac{4}{3p^2} \int_q^\Lambda \frac{\mathcal{G}(k^2)}{k^2} \frac{C(q^2) (B^2(q^2) - q^2 A^2(q^2)) - 2A(q^2) B(q^2) D(q^2)}{(q^2 A(q^2) + B(q^2))^2} \\ &\quad \times \left(p \cdot q + 2 \frac{(k \cdot p)(l \cdot q)}{k^2} \right), \\ D(p^2) &= Z_4 - Z_2^2 4 \int_q^\Lambda \frac{\mathcal{G}(k^2)}{k^2} \frac{B^2(q^2) D(q^2) + A(q^2) (2B(q^2) C(q^2) - A(q^2) D(q^2)) q^2}{(q^2 A(q^2) + B(q^2))^2}. \end{aligned} \quad (2-14)$$

where $k = p - q$. We proceed to take the first derivative of Eq. (2-9) with respect to current-quark mass, which yields

$$\frac{\partial S^{-1}(p)}{\partial m_f^\zeta} \Big|_{p^2=\zeta^2} = 1. \quad (2-15)$$

Compared with Eq. (2-11) and in combination with Eq. (2-10), one obtains

$$\begin{aligned} A(\zeta^2) &= 1, \\ D(\zeta^2) &= 1. \end{aligned} \quad (2-16)$$

On basis of this, we make a tiny change of $A(p^2)$ and $D(p^2)$ in Eq. (2-14), while keeping

$B(p^2)$ and $C(p^2)$ unchanged:

$$\begin{aligned}
 A'(p^2) &= 1 + Z_2^2 \frac{4}{3p^2} \int_q^\Lambda \frac{\mathcal{G}(k^2)}{k^2} \frac{A(q^2)}{q^2 A(q^2) + B(q^2)} \left(p \cdot q + 2 \frac{(k \cdot p)(k \cdot q)}{(p - q)^2} \right) \\
 B(p^2) &= Z_4 m(\zeta^2) + Z_2^2 4 \int_q^\Lambda \frac{\mathcal{G}(k^2)}{k^2} \frac{B(q^2)}{q^2 A(q^2) + B(q^2)} \\
 C(p^2) &= Z_2^2 \frac{4}{3p^2} \int_q^\Lambda \frac{\mathcal{G}(k^2)}{k^2} \frac{C(q^2) (B^2(q^2) - q^2 A^2(q^2)) - 2A(q^2) B(q^2) D(q^2)}{(q^2 A(q^2) + B(q^2))^2} \\
 &\quad \times \left(p \cdot q + 2 \frac{(k \cdot p)(l \cdot q)}{k^2} \right) \\
 D'(p^2) &= 1 - Z_2^2 4 \int_q^\Lambda \frac{\mathcal{G}(k^2)}{k^2} \frac{B^2(q^2) D(q^2) + A(q^2) (2B(q^2) C(q^2) - A(q^2) D(q^2)) q^2}{(q^2 A(q^2) + B(q^2))^2}.
 \end{aligned} \tag{2-17}$$

As a consequence, the renormalization condition becomes:

$$\begin{aligned}
 A(p^2) &= 1 + A'(p^2) - A'(\zeta^2), \\
 D(p^2) &= 1 + D'(p^2) - D'(\zeta^2),
 \end{aligned} \tag{2-18}$$

then the renormalization constants take the following forms:

$$\begin{aligned}
 Z_2 &= 2 - A'(\zeta^2), \\
 Z_4 &= 2 - D'(\zeta^2).
 \end{aligned} \tag{2-19}$$

Based on these preparations, in the chiral limit, the numerical solutions for the scalar functions $A(p^2)$, $B(p^2)$, $C(p^2)$ and $D(p^2)$ along with the renormalization constants Z_2, Z_4 are straightforward to solve via direct iteration. In terms of the non-chiral limit, only $A(p^2)$ and $B(p^2)$ need to be solved. We present the numerical results of $A(p^2)$, $B(p^2)$ and $M(p^2)$ with varied renormalization points ζ and different renormalization-group invariant (RGI) current-quark masses \hat{m} , viz.

$$\hat{m} = \lim_{p^2 \rightarrow \infty} \left(\frac{1}{2} \ln[p^2 / \Lambda_{\text{QCD}}^2] \right)^{\gamma_m} M(p^2). \tag{2-20}$$

The Figs. 2-1, 2-2, 2-3 show the comparisons between $\zeta = 2 \text{ GeV}$ and $\zeta = 19 \text{ GeV}$ in the chiral limit. In Figs. 2-4, 2-5, 2-6, we exhibit the comparisons between $\hat{m} = 0$, 6.8 MeV , 168 MeV at $\zeta = 19 \text{ GeV}$.

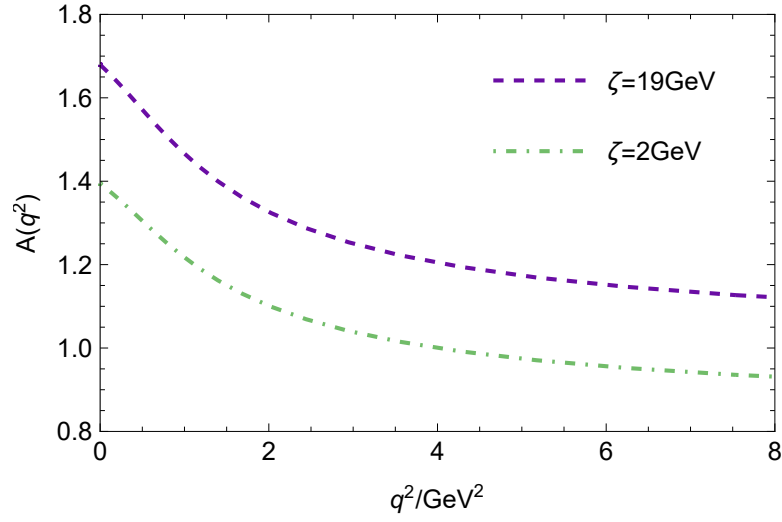


Fig. 2-1: Comparison of $A(p^2)$ at different values of the renormalization point.

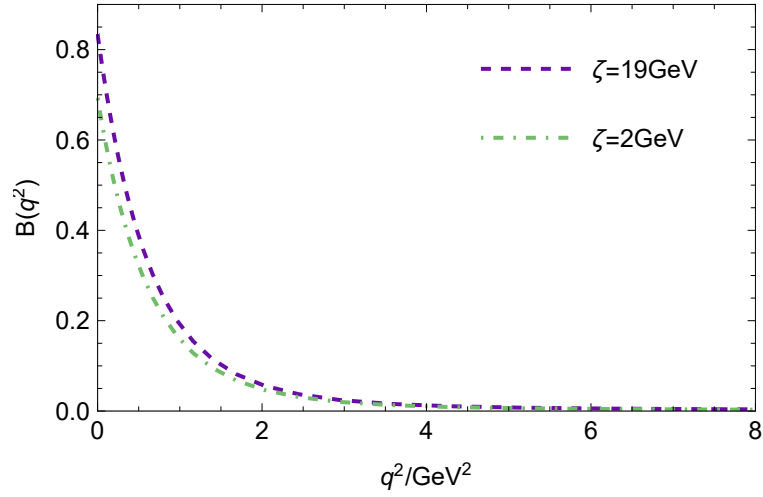


Fig. 2-2: Comparison of $B(p^2)$ at different values of the renormalization point. We can see $A(p^2)$ and $B(p^2)$ decrease as q^2 increases and this meets the requirement of asymptotic freedom.

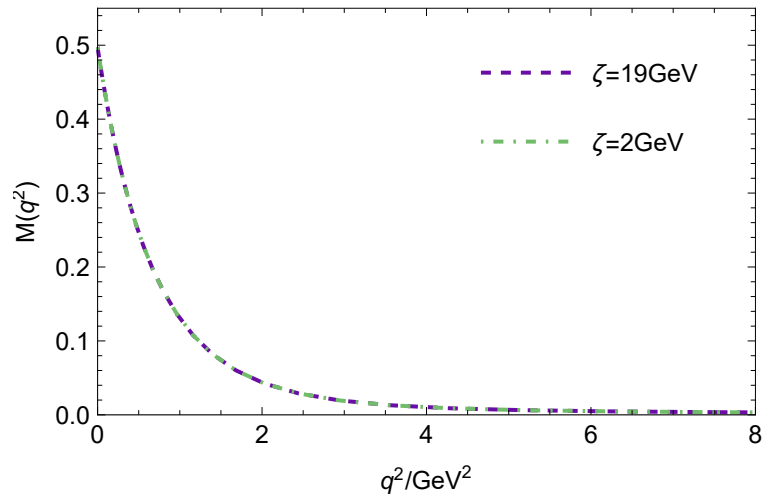
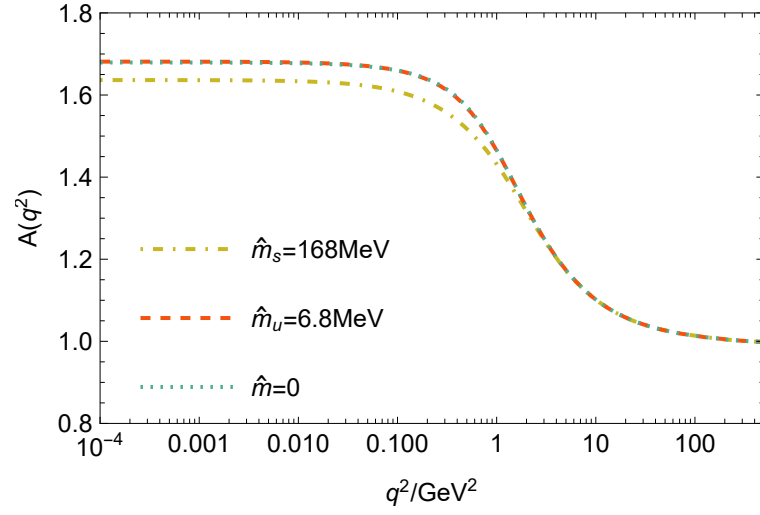
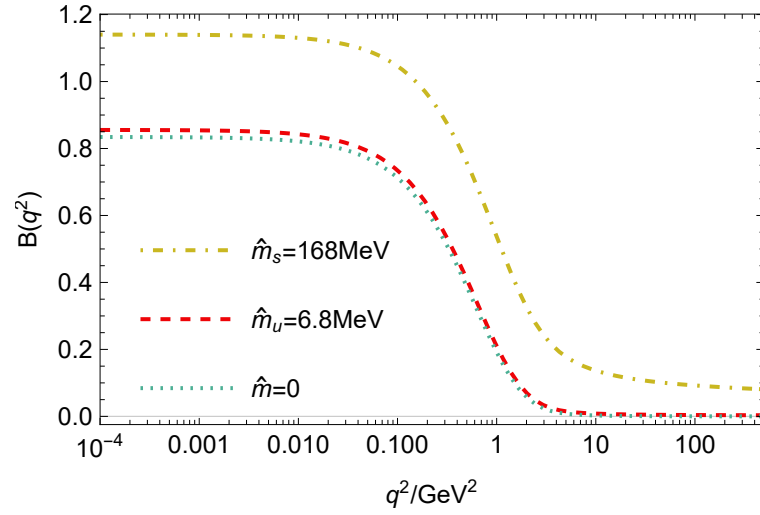
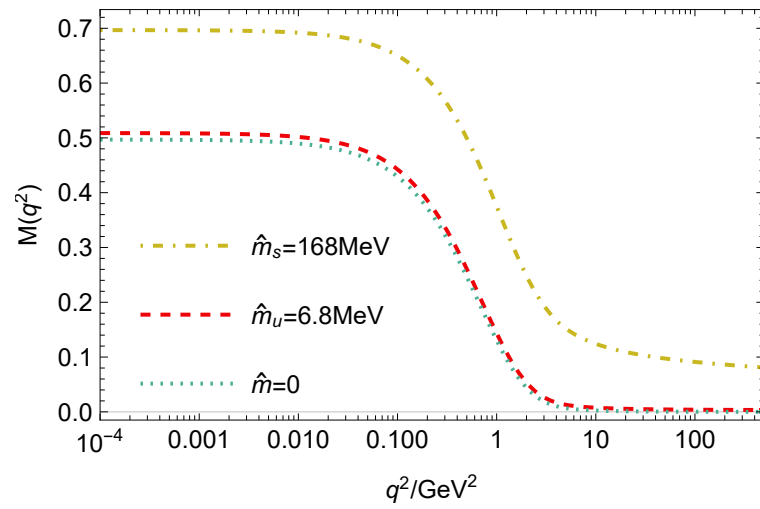


Fig. 2-3: Comparison of the mass function and we can see the mass function is renormalization point independent.

Fig. 2-4: Comparison of $A(p^2)$ at different current quark masses.Fig. 2-5: Comparison of $B(p^2)$ at different current quark masses.Fig. 2-6: Comparison of the mass function $M(p^2)$ at different current quark masses.

2.2 Bethe-Salpeter equation

The quark-antiquark bound state amplitude can be obtained by solving a homogeneous Bethe-Salpeter equation (BSE) Fig. 1-7, with f and g the flavour indices,

$$\Gamma^{f\bar{g}}(p; P) = Z_2^2 \int_q^\Lambda K(p, q; P) S^f(q_+) \Gamma^{f\bar{g}}(q; P) S^g(q_-), \quad (2-21)$$

where $p_+ = p + \eta P$ and $p_- = p - (1 - \eta)P$ are, respectively, the right- and left-directed momenta in Fig. 1-7, and similarly for q_\pm , and $P^2 = -m^2$. The relative momentum partitioning parameter $\eta \in [0, 1]$ is arbitrary; and since no observable can depend on η , its value can be chosen with a view to simplifying a given calculation. For mass-degenerate quarks, the value $\eta = 1/2$ is typically used. Employing the ladder truncation yields

$$K(p, q; P) \rightarrow -\mathcal{G}(k^2) T_{\mu\nu}(k) \frac{\lambda^a}{2} \gamma_\mu \otimes \frac{\lambda^a}{2} \gamma_\nu, \quad (2-22)$$

where $k = p - q$. The rainbow approximation, Eq. (2-4), combined with the ladder truncation [72] can describe the properties of many hadrons well, but it still has shortcomings. At present, some progress has been made in truncation schemes that go beyond the rainbow ladder approximation [73-76], but they are not yet ready for use in applications such as those considered herein. We therefore stick with the rainbow-ladder (RL) truncation, so that Eq. (2-21) becomes

$$\Gamma^{f\bar{g}}(p; P) = -Z_2^2 \int_q^\Lambda \mathcal{G}(k^2) T_{\mu\nu}(k) \frac{\lambda^a}{2} \gamma_\mu S^f(q_+) \Gamma^{f\bar{g}}(q; P) S^g(q_-) \frac{\lambda^a}{2} \gamma_\nu. \quad (2-23)$$

The Feynman diagrammatic form of Eq. (2-23) is depicted in Fig. 1-7. Meson bound states are usually ordered according to the values of J^{PC} which characterize them: total angular momentum, parity, and charge-conjugation signature. Since mesons are bosons, the quantum number of total angular momentum can only be integers, i.e. $J = 0, 1, 2, \dots$, which correspond to (pseudo)scalar mesons, (axial-)vector mesons and tensor mesons respectively. In terms of $J = 0, 1$, which have long been the focus of attention, there are four independent Lorentz structures for pseudoscalar and scalar

mesons, while eight for the vector mesons. The basis vectors for scalar mesons can be written as follows,

$$\begin{aligned}
 \tau_{0^+}^1 &= i\mathbf{I}, \\
 \tau_{0^+}^2 &= \gamma \cdot P, \\
 \tau_{0^+}^3 &= \gamma \cdot q, \\
 \tau_{0^+}^4 &= \frac{i}{2}[\gamma \cdot q, \gamma \cdot P].
 \end{aligned} \tag{2-24}$$

The basis for pseudoscalar mesons are listed below:

$$\begin{aligned}
 \tau_{0^-}^1 &= i\gamma_5, \\
 \tau_{0^-}^2 &= \gamma_5 \gamma \cdot P, \\
 \tau_{0^-}^3 &= \gamma_5 (P \cdot q) \gamma \cdot q, \\
 \tau_{0^-}^4 &= \gamma_5 \tau_{0^+}^4.
 \end{aligned} \tag{2-25}$$

In regard to vector mesons, the matrix-valued basis vectors are:

$$\begin{aligned}
 \tau_{1-\mu}^1 &= i\gamma_\mu^T, \\
 \tau_{1-\mu}^2 &= i \left[3q_\mu^T (\gamma^T \cdot q) - \gamma_\mu^T (q^T)^2 \right], \\
 \tau_{1-\mu}^3 &= i(P \cdot q) q_\mu^T \gamma \cdot P, \\
 \tau_{1-\mu}^4 &= i \left[\gamma_\mu^T \gamma \cdot P (\gamma^T \cdot q) + q_\mu^T \gamma \cdot P \right], \\
 \tau_{1-\mu}^5 &= q_\mu^T, \\
 \tau_{1-\mu}^6 &= (P \cdot q) \left[\gamma_\mu^T (\gamma^T \cdot q) - (\gamma^T \cdot q) \gamma_\mu^T \right], \\
 \tau_{1-\mu}^7 &= (q^T)^2 \left(\gamma_\mu^T \gamma \cdot P - \gamma \cdot P \gamma_\mu^T \right) - 2q_\mu^T (\gamma^T \cdot q) \gamma \cdot P, \\
 \tau_{1-\mu}^8 &= q_\mu^T (\gamma^T \cdot q) \gamma \cdot P,
 \end{aligned} \tag{2-26}$$

where the transverse projection is denoted by $X_\mu^T = X_\mu - \frac{(P \cdot X)P_\mu}{P^2}$. Next we decompose the meson amplitudes as

$$\Gamma_X(q, P) = \sum_i \tau_X^i(q, P) F_X^i(q^2, P \cdot q, P^2), \tag{2-27}$$

where $X = 0^-, 1^+, 0^+$.

The leptonic decay constant of pseudoscalar mesons, f_{0^-} , can be written as the following expression:

$$f_{0^-} P_\mu = Z_2 N_c \text{tr}_D \int_{dk}^\Lambda \gamma_5 \gamma_\mu S_f(k_+) \Gamma_{0^-}^{f\bar{g}}(k; P) S_g(k_-), \quad (2-28)$$

with the trace taken over spinor indices. For vector meson, the expression is

$$f_{1^-} = \frac{Z_2 N_c}{3M^{1^-}} \text{tr}_D \int_{dk}^\Lambda \gamma_\mu S_f(k_+) \Gamma_{1^-}^{f\bar{g}}(k; P) S_g(k_-), \quad (2-29)$$

where M^{1^-} denotes the vector meson mass. For the calculations of observables, the canonically normalised amplitude must be employed, viz. the amplitude obtained after rescaling such that

$$1 = \left. \frac{d}{dP^2} \Pi_X(Z, P) \right|_{Z=P}, \quad (2-30)$$

wherein

$$\Pi_{0^-}(Z, P) = 2N_c \text{tr}_D \int_{dk}^\Lambda \bar{\Gamma}_{0^-}^{f\bar{g}}(k; -Z) S_f(k_+) \Gamma_{0^-}^{f\bar{g}}(k; Z) S_g(k_-); \quad (2-31)$$

$$\Pi_{1^-}(Z, P) = \frac{N_c}{3} \text{tr}_D \int_{dk}^\Lambda \bar{\Gamma}_{1^-}^{f\bar{g}}(k; -Z) S_f(k_+) \Gamma_{1^-}^{f\bar{g}}(k; Z) S_g(k_-). \quad (2-32)$$

By inserting Eq. (2-27) into Eq. (2-23), the BSE is straightforward to solve as an eigenvalue problem: $\Gamma_X = \lambda(P^2) K \Gamma_X$ (i.e., see Appendix B). Here, $\lambda(P^2)$ is the eigenvalue of this equation; the Bethe-Salpeter amplitude, Γ_X , is the associated eigenvector. Herein, the Euclidean metric is employed, thus the on-shell mass for the meson lies at $P^2 < 0$. The physical solution can be obtained at $\lambda(P^2 = -M_X^2) = 1$. In Fig. 2-7, we plot the meson masses at different current quark masses.

The chiral-limit Goldberger-Treiman relation [77-78], which is depicted in Fig. 2-8, takes the following form:

$$f_\pi^0 E_\pi^0(p^2; P^2 = 0) = B_0(p^2), \quad (2-33)$$

where B_0 is calculated using gap equation in the chiral limit, and E_π^0 is the dominant

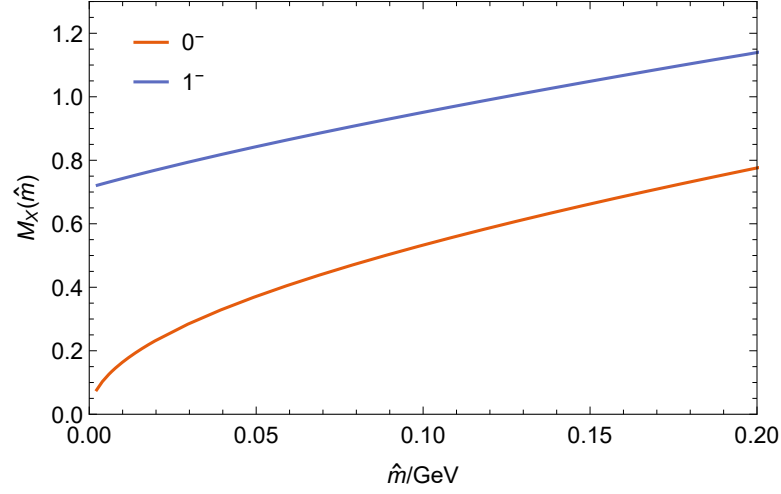


Fig. 2-7: This figure shows the evolution of masses of pseudoscalar and vector mesons with the renormalization group invariant current masses.

term in the pion canonically normalised BS amplitude:

$$\Gamma_\pi(k; P) = \tau_{0-}^1 E_\pi(k; P) + \tau_{0-}^2 F_\pi(k; P) + \tau_{0-}^3 G_\pi(k; P) + \tau_{0-}^4 H_\pi(k; P), \quad (2-34)$$

and f_π^0 is the pion decay constant in the chiral limit.

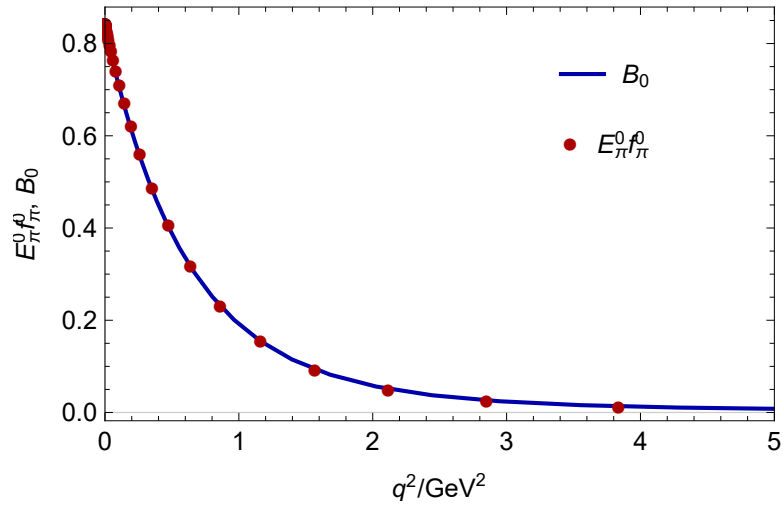


Fig. 2-8: Comparison between the two sides of Eq. (2-33).

The dressed-quark-W-boson vertex, $\mathcal{W}_\mu^{f\bar{g}}(p_+, p_-)$, satisfies the Ward-Green-Takahashi identity:

$$Q_\mu i\mathcal{W}_\mu^{f\bar{g}}(p_+, p_-) = S_f^{-1}(p_+) - S_g^{-1}(p_-) - (m_f - m_g) \Gamma_{0+}^{f\bar{g}}(Q). \quad (2-35)$$

Here, Γ_{0+}^{su} is an analogous Dirac scalar vertex, $p_+ = p + \eta Q$, $p_- = p - (1 - \eta)Q$.

Using the the ladder truncation, the inhomogeneous Bethe-Salpeter equation for the dressed-quark-W-boson vertex becomes

$$\begin{aligned} \mathcal{W}_\mu^{f\bar{g}}(p_+, p_-) &= (\gamma_\mu - \gamma_5 \gamma_\mu) - Z_2^2 \int_q^\Lambda \mathcal{G}(k^2) T_{\mu\nu}(k) \\ &\times \frac{\lambda^a}{2} \gamma_\mu S^f(q_+) \mathcal{W}_\mu^{f\bar{g}}(q_+, q_-) S^g(q_-) \frac{\lambda^a}{2} \gamma_\nu. \end{aligned} \quad (2-36)$$

Making more explicit the illustration in Fig. 1-6, Fig. 2-9 is the Feynman diagrammatic form of Eq. (2-23).

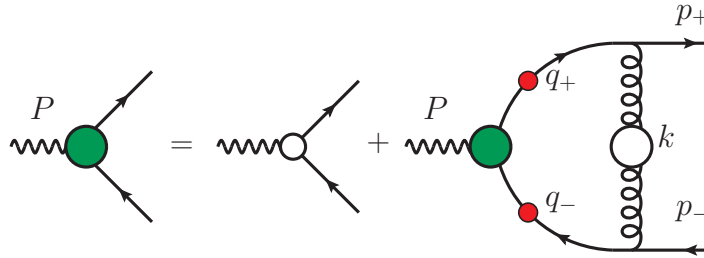


Fig. 2-9: Inhomogeneous Bethe-Salpeter equation for the weak interaction vector vertex in rainbow-ladder truncation.

Chapter 3 Semileptonic decay for pseudoscalar meson final state

3.1 Introduction

Semileptonic decays play a crucial role in testing and constraining the Standard Model of elementary particle physics. Studies of semileptonic decays are exploited to determine the magnitudes of fundamental parameters of the Standard Model, e.g., the CKM matrix elements.

The renormalization group improved rainbow approximation of the quark DSEs combined with the associated ladder truncation of the BSE for the meson bound-state amplitudes, is used to obtain Poincaré invariant predictions for the properties of light+light, heavy+light, and heavy+heavy mesons. This approach has been employed successfully to provide a unified explanation of the properties of hadrons with 0 – 3 heavy quarks, viz. from the lightest (almost) Nambu-Goldstone bosons to triply heavy baryons, e.g., Refs. [54, 58, 79]. Direct applicability to a wide variety of systems is a feature of the approach, which we exploit herein to deliver a coherent, parameter-free treatment of all the following semileptonic transitions: $K \rightarrow \pi$, $D \rightarrow \pi$, K and $D_s \rightarrow K$, $B_{(s)} \rightarrow \pi(K)$; and also the related masses and leptonic decay constants.

3.2 Semileptonic transitions

Weak semileptonic transitions are described by two scalar form factors, which embody all effects of hadron structure; and therefore, express the impact on weak interaction observables of EHM and its modulation by Higgs boson couplings into QCD.

As an instance, we choose $\bar{B}_s^0 \rightarrow K^+ \ell^- \bar{\nu}_\ell$, while others can be analysed analogously (Fig. 3-1). Consider the matrix element

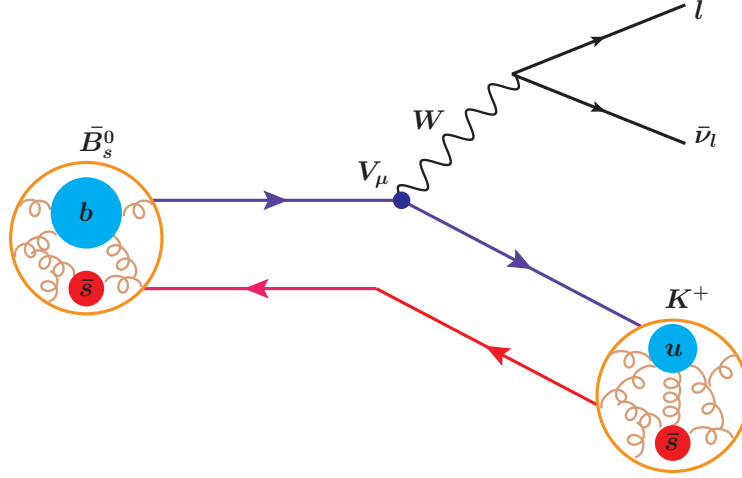


Fig. 3-1: The Semileptonic decay of $\bar{B}_s^0 \rightarrow K^+ \ell^- \bar{\nu}_\ell$.

$$\begin{aligned} M_\mu^{\bar{B}_s^0}(P, Q) &= \langle K^+(p) | \bar{u} i \gamma_\mu b | \bar{B}_s^0(k) \rangle \\ &= f_+(t) T_{\mu\nu}^Q P_\nu + f_0(t) \frac{P \cdot Q}{Q^2} Q_\mu, \end{aligned} \quad (3-1)$$

where $Q^2 T_{\mu\nu}^Q = Q^2 \delta_{\mu\nu} - Q_\mu Q_\nu$, $P = k + p$, $Q = k - q$, $k^2 = -m_{\bar{B}_s^0}^2$ and $p^2 = -m_{K^+}^2$; $t = -Q^2$; and $P \cdot Q = -(m_{\bar{B}_s^0}^2 - m_{K^+}^2)$, $P^2 = -2(m_{\bar{B}_s^0}^2 + m_{K^+}^2) + t$. Symmetries entail $f_+(t = 0) = f_0(t = 0)$, ensuring that there are no kinematic singularities. The physical domain of form factors is restricted by the masses of the hadrons involved: written as $t_\pm = (m_{\bar{B}_s^0} \pm m_{K^+})^2$, t_- is the largest t -value accessed in the decay process.

Once the form factors are obtained, one can calculate the associated branching fractions by integrating the differential decay width,

$$\left. \frac{d\Gamma}{dt} \right|_{\bar{B}_s^0 \rightarrow K^+ \ell^- \bar{\nu}_\ell} = \frac{G_F^2 |V_{ub}|^2}{192 \pi^3 m_{\bar{B}_s^0}^3} \lambda(m_{\bar{B}_s^0}, m_{K^+}, t)^{1/2} [1 - m_\ell^2/t]^2 \mathcal{H}^2, \quad (3-2)$$

over $t \in [m_\ell^2, t_-^{\bar{B}_s^0 K^+}]$, wherein $G_F = 1.166 \times 10^{-5} \text{ GeV}^{-2}$; $\lambda(m_{\bar{B}_s^0}, m_{K^+}, t) = (t_+^{\bar{B}_s^0 K^+} - t)(t_-^{\bar{B}_s^0 K^+} - t)$; and

$$\begin{aligned} \mathcal{H}^2 &= [1 + \frac{m_\ell^2}{2t}] \mathcal{H}_0^2 + \frac{3m_\ell^2}{2t} \mathcal{H}_t^2, \\ \mathcal{H}_0^2 &= \lambda(m_{\bar{B}_s^0}, m_{K^+}, t) |f_+(t)|^2, \mathcal{H}_t^2 = t_+^{\bar{B}_s^0 K^+} t_-^{\bar{B}_s^0 K^+} |f_0(t)|^2. \end{aligned} \quad (3-3)$$

The leading-order approximation to $M_\mu^{\bar{B}_s^0}$ in Eq. (3-1), provided by the rainbow-ladder truncation, takes the following form:

$$M_\mu^{\bar{B}_s^0}(P, Q) = 2N_c \text{tr} \int \frac{d^4s}{(2\pi)^4} S_b(s+k) \Gamma_{\bar{B}_s^0}(s+k/2; k) S_s(s) \times \bar{\Gamma}_{K^+}(s+p/2; -p) S_u(s+p) i\mathcal{W}_\mu^{ub}(s+p, s+k). \quad (3-4)$$

Here the Feynman diagrammatic form of Eq. (3-4) is depicted in Fig. 3-2. This approach has been widely used in the analyses of elastic and transition form factors.

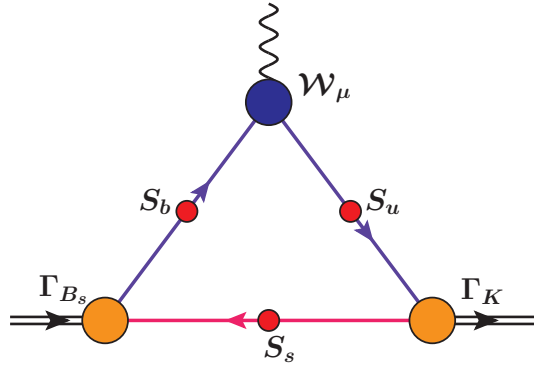


Fig. 3-2: The impulse approximation for the semileptonic transition.

There are three distinct types of matrix-valued function appearing in Eq. (3-4): the dressed-quark propagators involved in the transition process, written as $S_f(s)$ with $f = u, s, b$; Bethe-Salpeter amplitudes for the initial- and final-state mesons, Γ_M with $M = \bar{B}_s^0, K^+$; and the dressed $b \rightarrow u$ vector weak transition vertex, denoted by \mathcal{W}_μ^{ub} . Physically, \mathcal{W}_μ^{ub} must exhibit poles at $Q^2 + m_{B^*, B_0}^2 = 0$.

With the on-shell condition $k^2 = -m_{\bar{B}_s^0}^2$ and $p^2 = -m_{K^+}^2$, we parametrize the momenta of the P, Q explicitly as

$$Q = (0, 0, \frac{i\Delta_m}{\sqrt{-t + 2\Xi_m}}, \frac{\sqrt{\Delta_m^2 - 2\Xi_m t + t^2}}{\sqrt{-t + 2\Xi_m}}), \quad (3-5)$$

$$P = (0, 0, i\sqrt{-t + 2\Xi_m}, 0),$$

where $\Delta_m = m_{\bar{B}_s^0}^2 - m_{K^+}^2$ and $\Xi_m = m_{\bar{B}_s^0}^2 + m_{K^+}^2$ and the meson momenta can be obtained

by

$$\begin{aligned} k &= \frac{P+Q}{2}, \\ p &= \frac{P-Q}{2}. \end{aligned} \tag{3-6}$$

The BS amplitudes with these momenta can be attained by solving BSEs in a moving frame, which has been done explicitly in Ref. [80], or by solving Eq. (2-23) in the rest frame then extrapolating it by analytic continuation [81]. These two methods are introduced in Appendix B. We should keep in mind that the form factors should be frame independent.

For systems built solely from valence degrees-of-freedom chosen from u , d , s quarks (or antiquarks), every integrand involved in the calculation of quantities corresponding to the transition form factors is regular throughout its integration domain. Hence it is straightforward to obtain all results via numerical techniques which are described in Chapter 2. In Eq. (2-6), we employ

$$\begin{aligned} \omega &= 0.5 \text{ GeV}, \\ D \omega &= 0.8^3 \text{ GeV}^3. \end{aligned} \tag{3-7}$$

By this means, with renormalization group invariant light-quark current masses (in GeV),

$$\hat{m}_{u=d} = 0.0068, \hat{m}_s = 0.168, \tag{3-8}$$

which correspond to one-loop evolved values ($\zeta_2 = 2 \text{ GeV}$) $m_u^{\zeta_2} = 0.0044 \text{ GeV}$, $m_s^{\zeta_2} = 0.112 \text{ GeV}$, the meson masses and decay constants can be obtained, see Table 3-1. Remarkably, all masses and decay constants listed in Tables 3-1, 3-2 measure constructive interference between emergent and Higgs-boson mass generation [82-83].

Table 3–1: Static properties of light mesons related to the transitions considered herein, calculated using the current-quark masses in Eq. (3–8). For comparison and where available, values recorded by the particle data group (PDG) [3] are also listed. The mean absolute relative error between central values is 2(2)‰.

A	m_π	f_π	m_K	f_K	m_{K^*}	$m_{K_0^*}$
herein	0.138	0.093	0.494	0.110	0.938	0.877
PDG	0.138	0.092	0.494	0.110	0.892	0.845(17)

As the difference between the current-masses of the valence degrees-of-freedom in the initial-state meson increases, the maximum momentum-squared (t_-) transferred to the lepton pair also increases. At some point of this splitting, the growth in t_- entails that singularities related to the analytic structure of the dressed-quark propagators [84–85] are absorbed into the complex- s^2 integration domain, where straightforward numerical integration techniques fail. For initial states $Q\bar{u}$ and $Q\bar{s}$, this occurs at $\hat{m}_{Q\bar{u}} = 0.38 \text{ GeV}$, $\hat{m}_{Q\bar{s}} = 0.45 \text{ GeV}$, respectively.

A number of systematic methods have been developed so far to overcome this limitation, i.e., the employment of perturbation theory integral representations [57] for the calculation of form factors at large spacelike Q^2 , and the statistical Schlessinger point method (SPM) [54, 86–88], based on interpolation via continued fractions, which we exploit herein.

To proceed, we consider a fictitious pseudoscalar meson $P_{Q\bar{q}}$, $q = u, s$, and calculate its mass and leptonic decay constant as a function of \hat{m}_Q up to the value $\hat{m}_{Q\bar{q}}$. Then, using the SPM, we build interpolations: $m_P(\hat{m}_Q)$, $f_P(\hat{m}_Q)$ on the domains $\hat{m}_Q \in [\hat{m}_u, \hat{m}_{Q\bar{u}}]$, to access D , B initial states, and $\hat{m}_Q \in [\hat{m}_s, \hat{m}_{Q\bar{s}}]$, to reach D_s , B_s mesons. Those interpolations are then used to determine values of $\hat{m}_{c,b}$ such that the central (defined below) extrapolated results for $(m_{D,B} + m_{D_s,B_s})/2$ match the PDG values. This procedure yields (in GeV):

$$\hat{m}_c = 1.45, \hat{m}_b = 6.30. \quad (3-9)$$

Using solutions of the RL gap equations defined by these renormalization group invari-

ant current-quark masses, one obtains the following reference values of the dressed-masses (in GeV): $M_c(\zeta_2) = 1.19, M_b(\zeta_2) = 3.90$.

The meaning of “central” requires detailed explanation of the SPM. For any interpolation, we begin with a set of results for a given quantity, $Q(\hat{m}_Q)$, calculated at $N = 40$ values of \hat{m}_Q distributed evenly throughout the appropriate domain, which is defined above. We choose $M = 20$ current-mass values at random from that 40-element set, and then implement a continued fraction interpolation on this 20-element subset. Thereby, we obtain $C(40, 20) \sim 100$ -billion interpolating functions. From that possible number, the first $n_I = 100,000$ that are singularity free and positive definite $\hat{m}_Q \in [0, 2\hat{m}_b]$ are chosen. On the appropriate trajectory, our prediction for Q at any given value of $\hat{m}_Q > m_{Q\bar{q}}$ is then obtained by extrapolating each one of the chosen n_I SPM interpolants to the required current-mass. The value located at the centre of the band, within which 68% of the interpolants’ values lie, is cited as the result. This 1σ band is identified as the uncertainty in the result. Such an implementation of the SPM yields the predictions in Table 3–2. A detailed explanation of the SPM can be found in Refs. [88-89].

Table 3–2: All results are calculated using the SPM and the current-quark masses in Eq. (3–9). Each listed uncertainty expresses a 1σ confidence level on the SPM extrapolation, i.e., 68% of all SPM approximants give values that lie within the indicated range. The values recorded by the PDG [3] are also listed here. (All quantities in GeV.)

	m_D	f_D	m_{D_s}	f_{D_s}	m_{D^*}	$m_{S_{c\bar{d}}}$
herein	1.87(2)	0.163(4)	1.97(2)	0.181(3)	2.08(5)	2.12(3)
PDG	1.87	0.153(7)	1.97	0.177(3)	2.01	2.30(2)
	m_B	f_B	m_{B_s}	f_{B_s}		
herein	5.26(35)	0.136(17)	5.39(35)	0.160(14)		
PDG	5.28	0.138(19)	5.37	0.161(2)		
	$m_{D_s^*}$	$m_{S_{c\bar{s}}}$	m_{B^*}	$m_{B(0^+)}$		
herein	2.16(4)	2.29(3)	5.38(36)	5.44(36)		
PDG	2.11	2.32	5.33			

3.3 Transition form factors

Each of the form factors characterising a semileptonic transition can reliably be interpolated using the following function:

$$f_{+,0}(\alpha_1, \alpha_2, \alpha_3, m_{\mathcal{W}^+}; t) = \alpha_1^{+,0} + \alpha_2^{+,0}t + \frac{\alpha_3^{+,0}t^2}{m_{\mathcal{W}^+,0}^2 - t}, \quad (3-10)$$

where $m_{\mathcal{W}^+,0}$ is the relevant vector- or scalar-meson mass, respectively. Tables 3-1, 3-2, 3-3 recorded the calculated pole masses and interpolation coefficients for all semileptonic decays considered herein. In terms of the $K^+ \rightarrow \pi^0$ transition, these quantities can be calculated directly, therefore SPM uncertainty is absent in this case. For the remaining transitions, the SPM is used to determine all tabulated quantities, including the interpolation coefficients. Those associated with D, B mesons are obtained directly using this approach. In regard to the D_s, B_s mesons, the SPM is applied to ratios of the individual coefficients computed on the $Q\bar{u}$ and $Q\bar{s}$ trajectories, and then the corresponding D, B coefficients are multiplied by the extrapolation results. This procedure exploited the slow variation of the ratios and returns smaller SPM uncertainties for the D_s, B_s coefficients than direct extrapolation of coefficient values. Within mutual uncertainties, the values obtained via either method agree. Notably, the ratio analysis reveals that, with 99% and 85% confidence, respectively,

$$f_+^{D_s^d}(0)/f_+^{D_u^d}(0) > 1, f_+^{\bar{B}_s^d}(0)/f_+^{\bar{B}_u^d}(0) > 1. \quad (3-11)$$

3.3.1 $K^+ \rightarrow \pi^0$

The $K \rightarrow \pi$ transition form factors are depicted in Fig. 3-3, normalised by their values at $t = 0$. Our prediction is listed in Table 3-3: $f_+^{K_u^u}(0) = 0.964 = f_0^{K_u^u}(0)$. In combination with earlier continuum results obtained using comparable methods [90-91]

Table 3-3: Interpolation parameters for each form factor considered in this chapter, as labelled: Eq. (3-10), α_1 is dimensionless and $\alpha_{2,3}$ have dimension GeV^{-1} . N.B. Symmetry constraints, manifest in our treatment, ensure $\alpha_1^+ = \alpha_1^0$ for all transitions; and as plain from Eq. (3-10), $f_{+,0}(t=0) = \alpha_1^+$. (The SPM uncertainty estimate is discussed in the paragraph after that containing Eq. (3-9).)

	α_1^+	α_2^+	α_3^+	α_2^0	α_3^0
$K^+ \rightarrow \pi^0$	0.964	1.156	1.194	0.723	0.626
$D^0 \rightarrow \pi^-$	0.673(09)	0.151(05)	0.205(12)	0.0876(35)	0.0929(92)
$D_s^+ \rightarrow K^0$	0.681(10)	0.180(06)	0.236(14)	0.0980(39)	0.132(13)
$D^0 \rightarrow K^-$	0.796(09)	0.180(16)	0.217(35)	0.123(18)	0.123(39)
$\bar{B}^0 \rightarrow \pi^+$	0.287(54)	0.0130(11)	0.0170(20)	0.0065(08)	0.0060(16)
$\bar{B}_s^0 \rightarrow K^+$	0.293(55)	0.0175(21)	0.0182(22)	0.0076(09)	0.0062(17)

the average value is

$$f_{+,0}^{K_u^+}(0) = 0.971(9), \quad (3-12)$$

which agrees well with the PDG preferred value: 0.9706(27). As is shown in Fig. 3-3, our predictions for form factors are somewhat nonlinear. This indicates that nonlinear fitting models should be preferred in future analyses of $K \rightarrow \pi$ data.

Branching fractions of $K^+ \rightarrow \pi^0$ semileptonic transitions are listed in Table 3-4. They were computed with Eq. (3-2), amended to account for radiative corrections in this case [Ref. [3], Eq. (66.9)], the $t = 0$ result in Eq. (3-12), and the form factors drawn in Fig. 3-3. The branching fractions agree with the current PDG evaluations within quoted uncertainties.

3.3.2 $D^0 \rightarrow \pi^-, D_s^+ \rightarrow K^0, D^0 \rightarrow K^-$

Whilst overlapping, our final predictions for transition form factors of $D_{(s)}$ - initial states are slightly different from those in our first study [92], with smaller SPM uncertainties. Both outcomes are due to the physical constraint of positivity imposed additionally in our final analysis.

The $D^0 \rightarrow \pi^-$ transition form factors are drawn in Fig. 3-4. With regard to $f_+^{D_u^d}$, data are available from a variety of collaborations [4-7]. The prediction agrees with

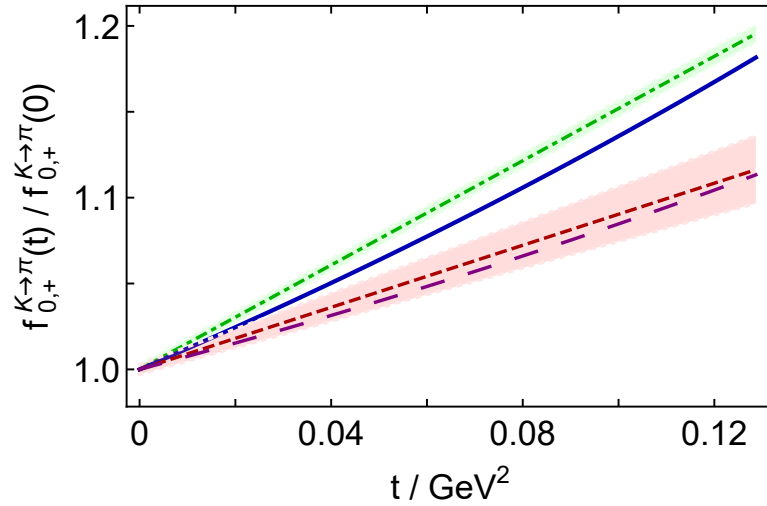


Fig. 3-3: $K \rightarrow \pi$ transition form factors, normalised by their $t = 0$ values: $f_+^{K_u}$, solid blue curve; and $f_0^{K_u}$, long-dashed purple curve. Comparison curves within like coloured bands are linear fits to available data described in Ref. [3]: $f_+^{K_u}$, dot-dashed green; and dashed red $f_0^{K_u}$.

Table 3-4: Pseudoscalar meson semileptonic branching fractions: each such fraction is to be multiplied by 10^{-3} . The column labelled “ratio” is the ratio of the preceding two entries in the row, so no factor of 10^{-3} is applied in this column. PDG [3] lists the following values for the CKM matrix elements: $|V_{us}| = 0.2245(8)$, $|V_{cd}| = 0.221(4)$, $|V_{cs}| = 0.987(11)$, $|V_{ub}| = 0.00382(24)$; and the following lifetimes (in seconds): $\tau_{K^+} = 1.2379(21) \times 10^{-8}$, $\tau_{D^0} = 4.10 \times 10^{-13}$, $\tau_{D_s^+} = 5.04 \times 10^{-13}$, $\tau_{\bar{B}^0} = 1.519 \times 10^{-12}$, $\tau_{\bar{B}_s^0} = 1.515 \times 10^{-12}$. All kinematic factors are evaluated using PDG values for meson masses.

	herein			PDG [3] or other, if indicated		
	$e^+ \nu_e$	$\mu^+ \nu_\mu$	ratio	$e^+ \nu_e$	$\mu^+ \nu_\mu$	ratio
$K^+ \rightarrow \pi^0$	50.0(9)	33.0(6)	0.665	50.7(6)	33.5(3)	0.661(07)
$D^0 \rightarrow \pi^-$	2.70(12)	2.66(12)	0.987(02)	2.91(4)	2.67(12)	0.918(40)
$D_s^+ \rightarrow K^0$	2.73(12)	2.68(12)	0.982(01)	3.25(36) [9]	34.1(4)	0.963(10)
$D^0 \rightarrow K^-$	39.0(1.7)	38.1(1.7)	0.977(01)	35.41(34)		ratio
		$\tau^- \bar{\nu}_\tau$	ratio	$\mu^- \bar{\nu}_\mu$	$\tau^- \bar{\nu}_\tau$	
$\bar{B}^0 \rightarrow \pi^+$	0.162(44)	0.120(35)	0.733(02)	0.150(06)		
$\bar{B}_s^0 \rightarrow K^+$	0.186(53)	0.125(37)	0.667(09)			

this collection, although there may be a hint of tension with the more recent sets [7, 69] at larger values of t . Owing to the presence of $\lambda(m_{D^0}, m_{\pi^-}, t)$ in Eq. (3-2), the contribution to the branching fraction from this domain is kinematically suppressed.

Predictions for $D^0 \rightarrow \pi^-$ branching fractions are shown in Table 3-4. For the ratio, we also computed this quantity from semileptonic transition form factors obtained via

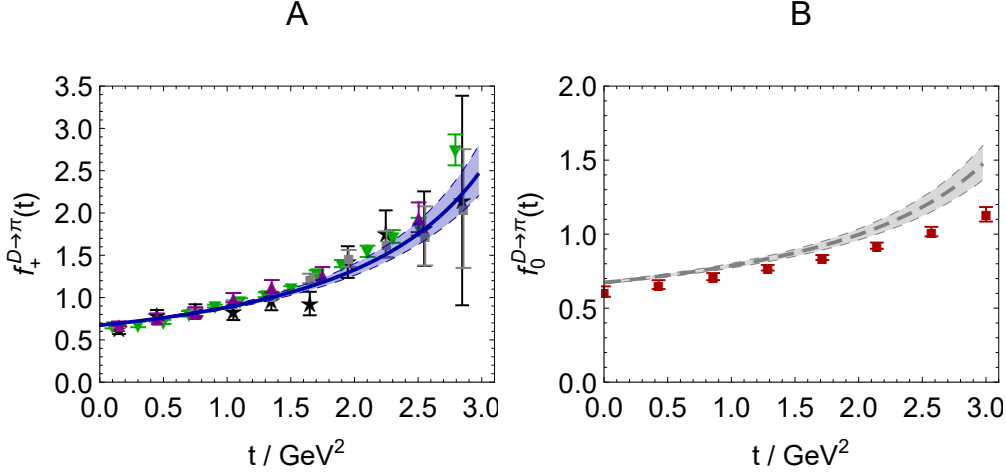


Fig. 3-4: Transition form factors of $D \rightarrow \pi$. Left panel- A. Data: black stars [4]; purple up-triangles [5]; green gray squares [6]; and down-triangles [7]. Right panel- B. f_0 is depicted as the dark-red squares from [8]. Legend: f_+ is depicted as the solid blue curve and f_0 as the long-dashed grey curve; and the like-coloured shaded bands represent the SPM uncertainty.

a symmetry-preserving regularisation of a vector \times vector contact interaction [93], with the result 0.980. Apparently, the ratio is independent of the form factors used to compute the individual fractions. Therefore, considering the minor impact of the μ mass on the t -domain, the empirically determined ratio seems roughly 2σ too small. Our prediction for the $\mu^+ \nu_\mu$ fraction is consistent with that of the PDG [3]. Combining with our prediction for the ratio, one obtains an $e^+ \nu_e$ fraction of $0.271(10)\%$, suggesting that the PDG value for this fraction is approximately 5.1σ too large when measured against its own quoted uncertainty.

The $D_s^+ \rightarrow K^0$ transition form factors are shown in Fig. 3-5. No data are available for these form factors, aside from the $t \approx 0$ datum in Ref. [9]: $f_+^{D_s^d}(0) = 0.720 \pm 0.084_{\text{stat}} \pm 0.013_{\text{syst}}$. As is shown in Fig. 3-5, this value agrees with our prediction within mutual uncertainties, which is listed in Table 3-3. There are no $D_s^+ \rightarrow K^0$ form factor results available yet from lQCD. Predictions for the corresponding branching fractions are recorded in Table 3-4. The difference between the existing measurement of the $e^+ \nu_e$ final state fraction [9] and our value is 1.4σ .

Transition form factors for $D^0 \rightarrow K^-$ are depicted in Fig. 3-6. In terms of $f_+^{D_d^s}$, data are available in Refs. [4-5, 7]. Our result is largely consistent with this collection, but there may be a hint that it sits too high at lower t values. For the branching fractions, the contributions from this domain are very crucial to the final predictions. Notably,

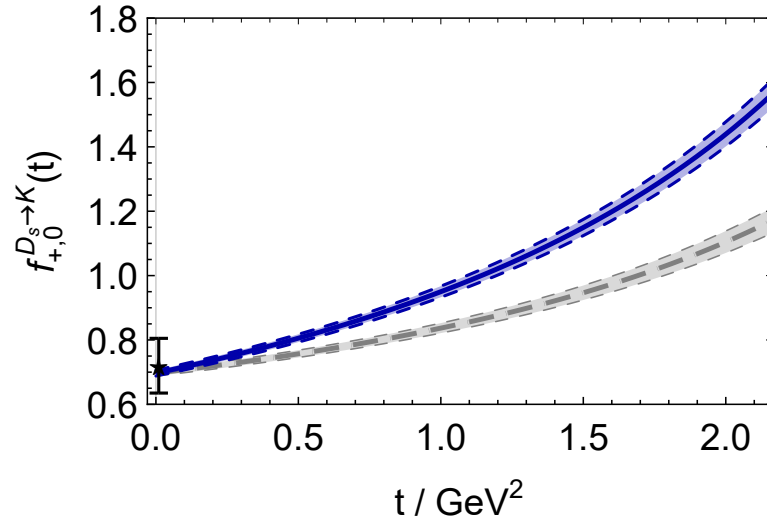


Fig. 3-5: Transition form factors of $D_s^+ \rightarrow K^0$. Sole available datum from Ref. [9]. f_+ is depicted as the blue curve and f_0 as the dashed grey curve.

however, within mutual uncertainties, our value for $f_+^{D_s^d}(0) = 0.796(9)$, recorded in Table 3-3, agrees with the $N_f = 2 + 1 + 1$ IQCD result reported in Ref. [8]: $0.765(31)$.

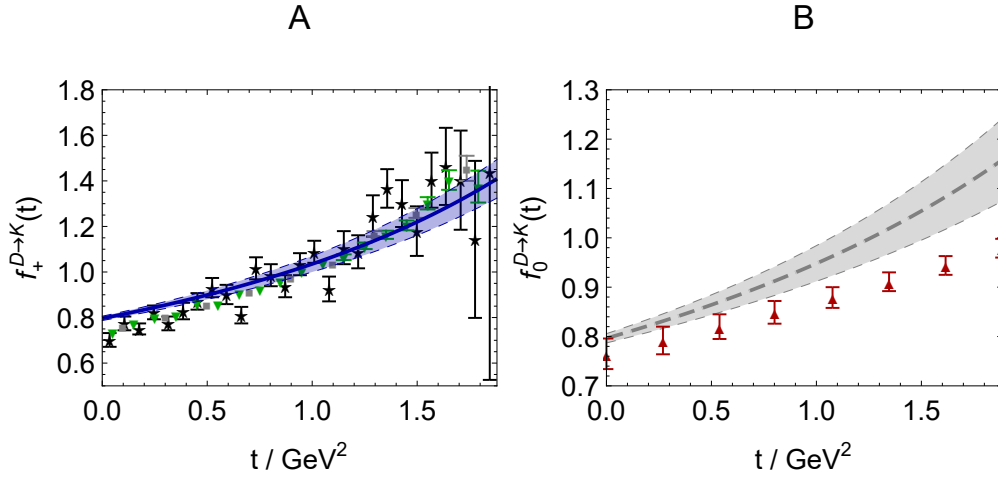


Fig. 3-6: $D \rightarrow K$ transition form factors. Left panel- A. Data: black stars [4]; gray squares [5] and green down-triangles [7]. Right panel- B. f_0 is depicted as the dark-red up-triangles from [8]. Legend: f_+ is depicted as the solid blue curve and f_0 as the long-dashed grey curve.

Our predictions for $D^0 \rightarrow K^-$ branching fractions are listed in Table 3-4. With the value of $|V_{cs}|$ listed in the caption, both the $e^+ \nu_e$ and $\mu^+ \nu_\mu$ fractions exceed their PDG values respectively; but the ratio agrees within 1.4σ , which indicates that a common overall factor should remedy the mismatch. From this perspective, one finds that the value $|V_{cs}| = 0.937(17)$ in combination with our form factors produces branching fractions which agree with the PDG values, viz., $3.52(18)\%$ and $3.44(18)\%$, respectively.

3.3.3 $\bar{B}^0 \rightarrow \pi^+, \bar{B}_s^0 \rightarrow K^+$

A sound, theoretical treatment of these transitions is challenging due to the Nambu-Goldstone boson character of pions and kaons and the large mass disparity between the initial and final state. DSEs have proven particularly effective for the former [76-77, 83, 94-95]. In dealing with the latter, it was highlighted in Ref. [93] that to attain a good description of such transitions throughout the kinematic domain, a realistic representation of the quark+antiquark interaction at large relative momentum is required. Our method expresses this; and since it is capable of producing precise results for the transition form factor on $\hat{m}_Q \in [0, \hat{m}_{Q^s}]$, the problem of mass disparity can also be circumvented.

Results for the $\bar{B}^0 \rightarrow \pi^+$ transition form factors are depicted in Fig. 3-7. With regard to $f_+^{\bar{B}^0 \rightarrow \pi^+}$, data have been collected by various collaborations [11-14]; and our predictions are in agreement with these data within mutual uncertainties. The data support a value

$$f_+^{\bar{B}^0 \rightarrow \pi^+}(t=0) = 0.27(2), \quad (3-13)$$

which is consistent with our prediction, Table 3-3. Using the form factors depicted

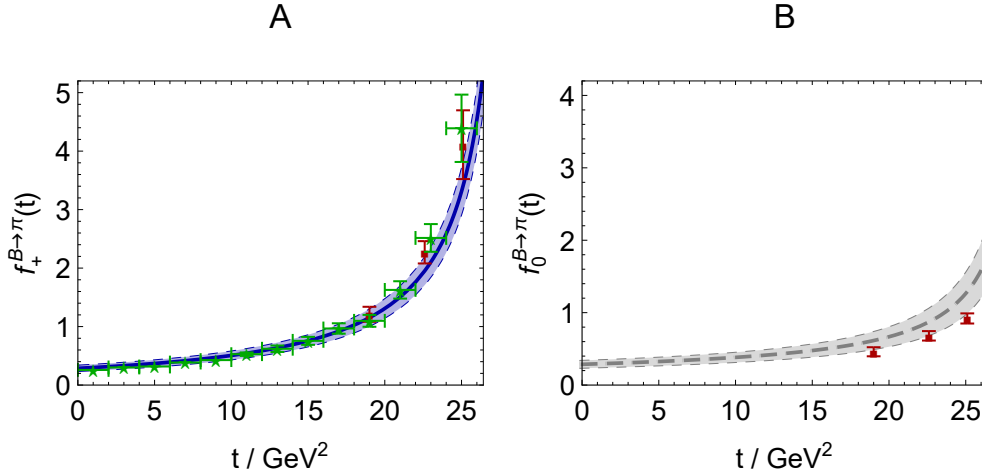


Fig. 3-7: Transition form factors of $\bar{B}^0 \rightarrow \pi^+$: f_+ - solid blue curve; f_0 - long-dashed grey curve; and the like-coloured shaded bands represent the SPM uncertainty. IQCD results: red squares in both panels come from [27]. Left panel - A. Data: green stars reconstructed from the average [Ref. [10], Tab.81] of data reported in Refs. [11-14].

in Fig. 3-7 we obtain the $\bar{B}^0 \rightarrow \pi^+$ branching fractions, listed in Table 3-4. The PDG

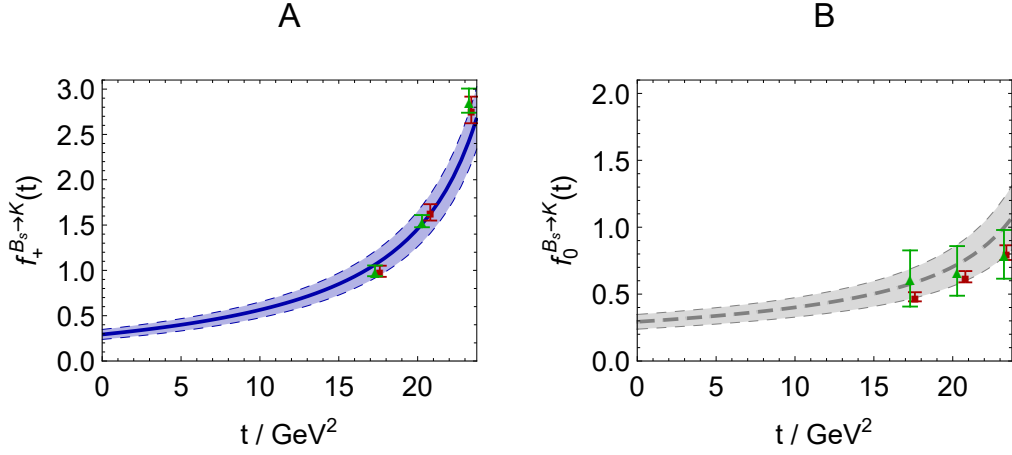


Fig. 3-8: Transition form factors of $\bar{B}_s^0 \rightarrow K^+$. f_+ - solid blue curve; f_0 - long-dashed grey curve. IQCD results: green up-triangles [15] and red squares [16] in both panel.

provides a result for the $\mu^- \nu_\mu$ final state, which matches our prediction within mutual uncertainties. Exact agreement is obtained with

$$|V_{ub}| = 0.00374(44). \quad (3-14)$$

This value agrees well with other analyses of $\mathcal{B}_{\bar{B}^0 \rightarrow \pi^+ \mu^- \bar{\nu}_\mu}$ ([3], Sec. 75.3); hence, increases tension with the higher value inferred from inclusive decays. For the $\tau^- \nu_\tau$ final state, no empirical information is available and, consequently, the $\tau:\mu$ ratio. A $N_f = 2 + 1$ -flavour IQCD study yields 0.69(19) [16], which matches our result 0.733(2) within its uncertainty.

Fig. 3-8 presents our calculated $\bar{B}_s \rightarrow K^+$ form factors. Despite recent observation of the $B_s \rightarrow K^-$ transition [17], no form factor data are yet available. Hence our predictions are compared with results of $N_f = 2 + 1$ -flavour IQCD calculations [15-16]. Due to the difficulties of calculating form factors involving heavy + light mesons with the use of lattice methods, the results of IQCD are restricted to a few points on the domain $t \gtrsim 17 \text{ GeV}^2$, as is shown in Fig. 3-8. Such results are now typically employed by IQCD analyses, using a practitioner-preferred functional form, to develop a least-squares fit to the form factor points. This fit is then used to define the form factor on the entire kinematically accessible domain, $0 \lesssim t \lesssim 25 \text{ GeV}^2$. At this time, in consideration of the sparsity of points and their limited precision, the SPM cannot profitably be used

to develop function-form unbiased representations of the IQCD output.

The $\bar{B}_s^0 \rightarrow K^+$ branching fractions in Table 3-4 are produced by form factors in Fig. 3-8. Ref. [17] reports the following value:

$$\mathcal{B}_{B_s^0 \rightarrow K^+ \mu^+ \nu_\mu} = [0.106 \pm 0.005_{\text{stat}} \pm 0.008_{\text{syst}}] \times 10^{-3}. \quad (3-15)$$

Comparison of this measurement with our prediction is depicted in Fig. 3-9, as well as the results obtained via various other means: experiment and theory are in agreement, but only because the uncertainty of theory is large. The unweighted average of the theoretical results is $0.141(44) \times 10^{-3}$ and the uncertainty weighted mean is $0.139(08) \times 10^{-3}$. Omitting entries V-VI [15, 96], these results increase: unweighted $0.159(38) \times 10^{-3}$ and uncertainty weighted $0.156(10) \times 10^{-3}$. The extrapolations used in Refs. [15, 96] deliver values of $f_+^{B_s^u}(0)$ that are roughly one-half of those recorded in I-IV [18-20, 22]: $0.148(53)$ vs. $0.299(86)$. This is sufficient to explain the difference in branching fractions: V-VI vs. I-IV in Fig. 3-9. An alternate method to fit and extrapolate IQCD results, with the datum in Ref. [17] as an additional constraint, delivers [97]: $f_+^{\bar{B}_s^u}(0) = 0.211(3)$. We note that Ref. [97] also deduces $f_+^{\bar{B}_d^u}(0) = 0.255(5)$ leading to $f_+^{\bar{B}_s^d}(0)/f_+^{\bar{B}_d^u}(0) < 1$, which conflicts with our analyses – Eq. (3-11), and the results in a series of other studies, e.g., Refs. [18-19, 98-104]. Hence, the value for $f_+^{\bar{B}_s^u}(0)$ in Ref. [97] may be too small. There is no available empirical information on the $\tau \nu_\tau$ final state; therefore, none on the $|V_{ub}|$ -independent ratio that would test lepton flavour universality. So, in Fig. 3-9B, our prediction for this ratio, listed in Table 3-4, is compared with results obtained by other means. The unweighted average of the theory results is $0.705(87)$ and the uncertainty weighted mean is $0.678(03)$. Omitting entries V-VI [16, 21], these results are: unweighted $0.653(41)$ and uncertainty weighted $0.677(03)$. Many uncertainties cancel in this ratio within internally consistent analyses; therefore the values should be more reliable than calculating either fraction alone.

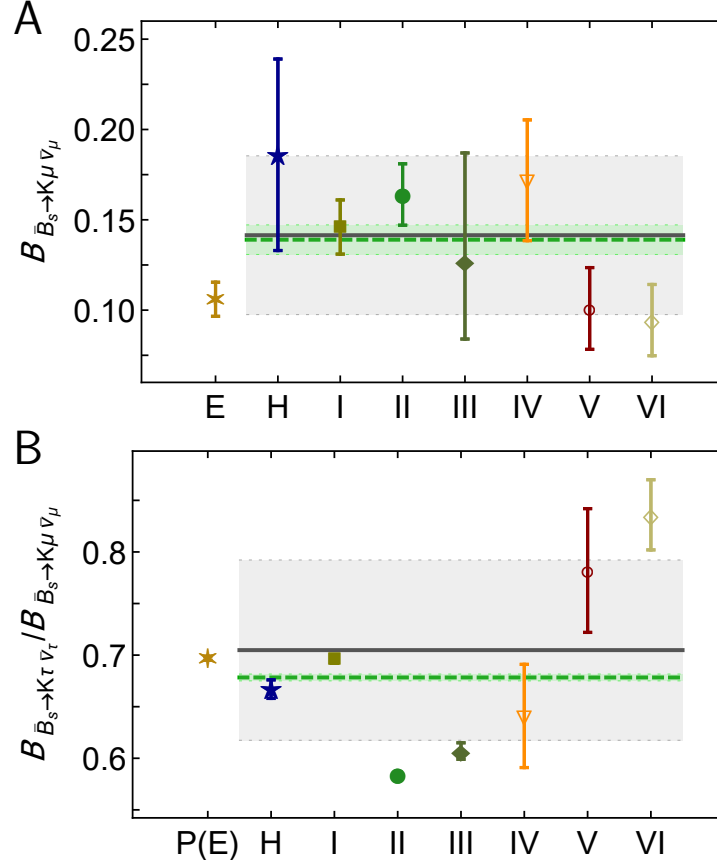


Fig. 3-9: *Top panel*–A. Branching fraction $\mathcal{B}_{\bar{B}_s^0 \rightarrow K^+ \mu^- \bar{\nu}_\mu}$ computed herein, “H”, compared with the value in Eq. (3-15), “E”, viz. a measurement of $\mathcal{B}_{\bar{B}_s^0 \rightarrow K^+ \mu^- \bar{\nu}_\mu}$ [17] and some results obtained using other means: continuum I – III [18-20]; and lattice IV – VI [15-16, 21]. *Bottom panel*–B. Branching fraction ratio $\mathcal{B}_{\bar{B}_s^0 \rightarrow K^+ \tau^- \bar{\nu}_\tau} / \mathcal{B}_{\bar{B}_s^0 \rightarrow K^+ \mu^- \bar{\nu}_\mu}$ computed herein compared with some results obtained using other means. Legend as in Panel A, except “P(E)” is the result from [22], which is an estimate constrained by the datum in Ref. [17]. Both panels – Grey line and like-coloured band: unweighted mean of theory results and related uncertainties. Green dashed line and green band: uncertainty-weighted average of theory results and associated uncertainty.

3.4 Remarks

A systematic, symmetry-preserving approach was employed to deliver a unified set of parameter-free predictions for the masses and leptonic decay constants of π , K , $D_{(s)}$, $B_{(s)}$ mesons, and the semileptonic $K \rightarrow \pi$, $D \rightarrow \pi$, K and $D_s \rightarrow K$, $B_{(s)} \rightarrow \pi(K)$ transition form factors throughout the physical kinematic domain, along with the corresponding branching fractions. Pivotal results include an indication that the PDG value for $\mathcal{B}_{D^0 \rightarrow \pi^- e^+ \nu_e}$ is 5.1σ too large when measured against its own quoted uncertainty; quantitative agreement with all measured transition form factors; improved accuracy on the $|V_{cs}|$ value from semileptonic decays; predictions for the hitherto unmeasured

$D_s \rightarrow K^0, \bar{B}_s \rightarrow K^+$ form factors; and predictions for five as yet unmeasured branching fractions and all branching fraction ratios in this sector that can be applied to test lepton flavour universality.

Notably, a quantitative analysis which compares existing theory and the recent measurement of $\mathcal{B}_{B_s^0 \rightarrow K^- \mu^+ \nu_\mu}$, was also presented. Broadly, there is agreement; however, the paucity of precision in contemporary theory prevents any firm conclusions. Measurements enabling extraction of the transition form factors of $B_s^0 \rightarrow K^-$ would be particularly useful for refining both comparisons with theory and between theory analyses of $|V_{ub}|$.

Efforts are underway to improve the precision of our results. The extension to semileptonic transitions with vector meson final states has been completed, one of which will be discussed in the next Chapter. Such a comprehensive, unified set of parameter-free predictions for leptonic decay constants and heavy-to-light semileptonic transitions allows for a deeper and broader understanding of the roles of emergent hadronic mass, Higgs-boson couplings, and the interference between them in forming observable phenomena; in particular, their impacts on the values of the CKM matrix elements.

Chapter 4 Semileptonic B_c to η_c and J/ψ transitions

4.1 Introduction

The B_c meson was discovered a little over twenty years ago [105]. With mass $m_{B_c} = 6.2749(8) \text{ GeV}$ [3], it lies below the threshold for BD decay; and due to the fact that it is an open flavour state, electromagnetic decays are forbidden. Hence only flavour-changing weak decays are possible within the Standard Model. As a result, B_c has a relatively long lifetime [3]: $0.510(9)\text{ps}$, which is, e.g., ten-billion-times longer than that of the η_c . These features make the B_c a particularly interesting system, i.e., it is the lightest open-flavour bound-state of the two heaviest quarks in Nature that are experimentally pliable; with its lifetime long enough to enable the measurements.

Flavour-changing B_c weak decays involve one of the following transitions: $\bar{b} \rightarrow \bar{u}, \bar{b} \rightarrow \bar{c}, c \rightarrow s, c \rightarrow d$. Specific entries in the CKM matrix modulate the intensity of these decays. Since $|V_{cs}|$ is the largest among the four involved here, we may expect that $B_c \rightarrow B_s$ transitions dominate. Contemporary calculations, e.g., Refs. [93, 97, 106] support this expectation. Another factor is the available phase space, e.g., with $\eta_c, J/\psi$ final states, this is more than ten-times larger than for B ; and such amplification may be sufficient to overwhelm the factor of roughly six suppression from $|V_{cb}|/|V_{cd}|$. This is borne out by the calculation of the branching fractions ratio, for instance [93]: $\mathcal{B}_{B_c^+ \rightarrow \eta_c \ell^+ \nu_\ell} / \mathcal{B}_{B_c^+ \rightarrow B^0 \ell^+ \nu_\ell} \approx 6$, where ℓ is a light lepton. (It is a qualitative prediction of long standing [107-108].) It is therefore not surprising that the B_c was found in decays to J/ψ final states, especially when considering the narrow and prominent decay width for $J/\psi \rightarrow \ell^+ \ell^-$.

Data obtained in the last decade, which may indicate lepton universality violations in b -quark decays [109-115], raise studies of the semileptonic decays of B_c -mesons

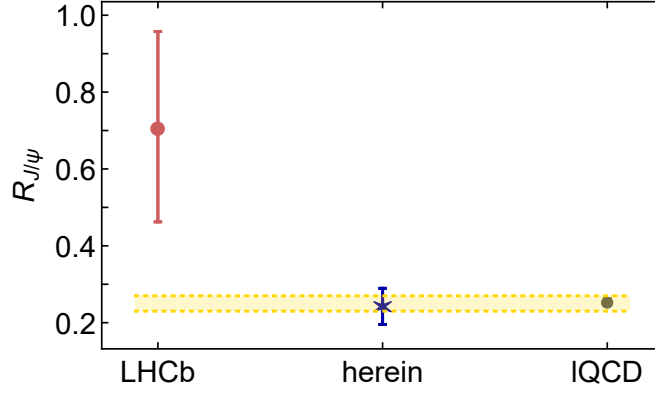


Fig. 4-1: Ratio $R_{J/\psi}$ in Eq. (4-1) – red circle, empirical result from LHCb Collaboration [23]; blue star – our prediction; grey square – IQCD result [24-25]; and gold band – unweighted mean of central values from contemporary calculations [26-31].

with final-states of ground-state charmonia to a new level of importance in searching for physics outside the Standard Model paradigm. As a matter of fact, the LHCb collaboration has obtained [23]:

$$R_{J/\psi} := \frac{\mathcal{B}_{B_c^+ \rightarrow J/\psi \tau \nu}}{\mathcal{B}_{B_c^+ \rightarrow J/\psi \mu \nu}} = 0.71 \pm 0.17(\text{ stat }) \pm 0.18(\text{ syst }). \quad (4-1)$$

It is indicated in Fig. 4-1 that this result lies about two standard deviations (2σ) above the range of central values which is predicted by reliable calculations within the Standard Model. This difference may be a signal of violation of lepton universality in Nature's weak interactions. In this chapter, we analyse $B_c \rightarrow \eta_c, J/\psi$ semileptonic decays within the DSE framework that was introduced above.

4.2 Transition form factors: definitions

The transition matrix elements for $B_c \rightarrow \eta_c$ and J/ψ are, respectively,

$$\begin{aligned} M_\mu^{B_c \rightarrow \eta_c}(P, Q) &= \langle \eta_c(p_{\eta_c}) | \bar{c} i \gamma_\mu b | B_c(k) \rangle \\ &= f_+(t) T_{\mu\nu}^Q P_\nu + f_0(t) \frac{P \cdot Q}{Q^2} Q_\mu, \end{aligned} \quad (4-2)$$

$$\begin{aligned}
M_{\mu;\lambda}^{B_c \rightarrow J/\psi}(P, Q) &= \langle \psi^\lambda(p_\psi; \lambda) | \bar{c} i (\gamma_\mu - \gamma_\mu \gamma_5) b | B_c(k) \rangle \\
&= 2m_{J/\psi} \frac{Q_\mu \epsilon^\lambda \cdot Q}{Q^2} A_0(t) + [m_{B_c} + m_{J/\psi}] T_{\mu\nu}^Q \epsilon_\nu^\lambda A_1(t) \\
&\quad + \left[P_\mu + Q_\mu \frac{m_{B_c}^2 - m_{J/\psi}^2}{Q^2} \right] \frac{\epsilon^\lambda \cdot Q A_2(t)}{m_{B_c} + m_{J/\psi}} \\
&\quad + \varepsilon_{\mu\nu\rho\sigma} \epsilon_\nu^\lambda k_\rho p_{\psi\sigma} \frac{2V(t)}{m_{B_c} + m_{J/\psi}},
\end{aligned} \tag{4-3}$$

where $Q^2 T_{\mu\nu}^Q = Q^2 \delta_{\mu\nu} - Q_\mu Q_\nu$, $P = k + p_{\eta_c, \psi}$, $Q = p_{\eta_c, \psi} - k$, with $k^2 = -m_{B_c}^2$, $p_{\eta_c}^2 = -m_{\eta_c}^2$, $p_\psi^2 = -m_{J/\psi}^2$. Herein $\epsilon_\nu^\lambda(p_f)$ is a polarisation four-vector, with

$$\sum_{\lambda=1}^3 \epsilon_\nu^\lambda(p_f) \epsilon_\mu^\lambda(p_f) = T_{\mu\nu}^{pf}. \tag{4-4}$$

$t = -Q^2$ is the squared momentum-transfer, and $t_\pm^M = (m_{B_c} \pm m_M)^2$, $M = \eta_c, J/\psi$. Again, t_- is the largest accessible value of t in the identified physical decay process. In Eqs. (4-2, 4-3), the semileptonic transition form factors are denoted by the scalar functions. As required by symmetry and ensuring the absence of kinematic singularities, Eqs. (4-2, 4-3) must satisfy the following relations:

$$\begin{aligned}
f_+(0) &= f_0(0), \\
A_0(0) &= \frac{m_{B_c} + m_{J/\psi}}{2m_{J/\psi}} A_1(0) - \frac{m_{B_c} - m_{J/\psi}}{2m_{J/\psi}} A_2(0).
\end{aligned} \tag{4-5}$$

With the obtained predictions for the transition form factors, one can calculate the corresponding branching fractions from the differential decay width for $B_c \rightarrow M l^+ \nu_l$:

$$\left. \frac{d\Gamma}{dt} \right|_{B_c \rightarrow M l \nu_l} = \frac{G_F^2 |V_{cb}|^2}{192\pi^3 m_{B_c}^3} \lambda(m_{B_c}, m_M, t) \frac{(t - m_l^2)^2}{t^2} \mathcal{H}^2. \tag{4-6}$$

The notations of this equation have been discussed in Chapter 3. For $M = \eta_c$, $H_\pm \equiv 0$,

$$H_0 = \lambda(m_{B_c}, m_{\eta_c}, t) f_+(t), H_t = (m_{B_c}^2 - m_{\eta_c}^2) f_0(t). \tag{4-7}$$

For $M = J/\psi$,

$$\begin{aligned}
\frac{1}{\sqrt{t}} H_{\pm} &= (m_{B_c} + m_{J/\psi}) A_1(t) \mp \frac{\lambda(m_{B_c}, m_{J/\psi}, t)}{m_{B_c} + m_{J/\psi}} V(t), \\
H_0 &= \frac{1}{2m_{J/\psi}} [(m_{B_c}^2 - m_{J/\psi}^2 - t)(m_{B_c} + m_{J/\psi}) A_1(t) \\
&\quad - \frac{\lambda(m_{B_c}, m_{J/\psi}, t)^2}{m_{B_c} + m_{J/\psi}} A_2(t)], \\
H_t &= \lambda(m_{B_c}, m_{J/\psi}, t) A_0(t).
\end{aligned} \tag{4-8}$$

4.3 Transition form factors: matrix elements

Using the method introduced in the previous chapters, the matrix elements in Eqs. (4-2, 4-3) can be written as:

$$\begin{aligned}
M_{\mu}^{B_c \rightarrow M}(P, Q) &= N_c \text{tr} \int \frac{d^4 s}{(2\pi)^4} S_b(s+k) \Gamma_{B_c}(s+k/2; k) S_c(s) \\
&\quad \times \Gamma_M(s+p/2; -p) S_c(s+p) i \mathcal{W}_{\mu}^{cb}(s+p, s+k).
\end{aligned} \tag{4-9}$$

Solving the gap equations and BSEs using the following renormalization-point-invariant c and b current-quark masses (in GeV):

$$\hat{m}_c = 1.61, \quad \hat{m}_b = 6.96, \tag{4-10}$$

one obtains the corresponding meson masses and leptonic decay constants in Table 4-1. The mean absolute relative error between our predictions and empirical values is 3.6%. It is worth noting that $r_{b:c} = \hat{m}_b/\hat{m}_c = 4.32$ and, equivalently, $r_{c:b} = 0.23$.

The masses in Eq. (4-10) are in correspondence to the following current masses at our renormalization scale: $m_c^{\zeta_{19}} = 0.82$ GeV, $m_b^{\zeta_{19}} = 3.55$ GeV; and one-loop evolved to $\zeta = \zeta_2 = 2$ GeV, $m_c^{\zeta_2} = 1.22$ GeV, $m_b^{\zeta_2} = 5.26$ GeV. Working with the dressed-quark mass-functions from solving the gap equations, $M_{c,b}(k)$, and defining Euclidean constituent-quark masses as the solutions of $M_{c,b}(M_{c,b}^E) = M_{c,b}^E$, one finds (in GeV): $M_c^E = 1.33$, $M_b^E = 4.12$. These quantities are analogous to the oft-cited “running masses” associated with heavy quarks, and our predictions are within 3% of those in

Ref. [3].

Notably, the mass values in Eq. (4–10), obtained by considering heavy+heavy mesons, are within 10% of those determined in the very different case of heavy+light mesons, Eq. (3–9). This highlights the utility of the SPM as a tool for enabling RL truncation to be used in delivering a combined treatment of such markedly different systems, something that was previously viewed as impossible.

Some important physical aspects of weak transition vertex, \mathcal{W}_μ^{cb} , are worth mentioning. Pseudoscalar-to-pseudoscalar transitions involve only the vector part, possessing poles at $Q^2 + m_{B_c^*, B_{c0}^*}^2 = 0$. Pseudoscalar-to-vector transitions also involve the axial-vector part, with poles at $Q^2 + m_{B_c, B_{c1}}^2 = 0$. It is indicated in our treatment that the presence of these poles is a prerequisite for any valid analyses of $B_c \rightarrow \eta_c, J/\psi$ semileptonic transitions.

Table 4–1: Static properties of mesons evaluated using bound-state equations. Normalisation: the empirical value of the pion leptonic decay constant is $f_\pi \approx 0.092$ GeV. Empirical values (expt.), where available, drawn from Ref. [3]; and lattice-QCD (lQCD) results for leptonic decay constants from Refs. [34–36]. The mean absolute relative error between our predictions and empirical results is 3.6%. (All dimensioned quantities in GeV.)

	m_{η_c}	$m_{J/\psi}$	m_{B_c}	m_{η_b}	m_Υ	f_{η_c}	$f_{J/\psi}$	f_{B_c}	f_{η_b}	f_Υ
herein	2.98	3.12	6.27	9.19	9.28	0.28	0.30	0.43	0.56	0.53
expt.	2.98	3.10	6.27	9.40	9.46	0.24	0.29			0.51
lQCD						0.28	0.29	0.31	0.47	0.46

4.4 Computational scheme and results

In Eq. (4–9), the integration samples the appearing functions on a material domain of their complex-valued arguments. As long as the initial- and final-state meson masses are similar, which means that the ratio of the involved quark current-masses $r_{Q_1:Q_2}$ does not differ too much from unity, the integral can be evaluated via simple numerical techniques straightforwardly. This is due to the fact that t_- and, hence, the maximum momentum of the recoiling meson, remains modest. Notably, however, at some value of $r_{Q_1:Q_2} =: r_f, t_-$ becomes so large that singularities, which are associated

Table 4-2: This table shows SPM interpolation parameters for each transition form factor considered in this chapter, as labelled: Eq. (4-12), α_1 is dimensionless and $\alpha_{2,3}$ have dimension GeV^{-1} . α_i^x represents the parameter α_i for $x(t)$ where $i = 1, 2, 3$ and $x = f_+, f_-, A_0, A_1, A_2, V$. (The SPM uncertainty estimate is discussed in the paragraph before that containing Eq. (4-11)).

$B_c \rightarrow \eta_c$	$\alpha_1^{f_+}$	$\alpha_2^{f_+}$	$\alpha_3^{f_+}$	$\alpha_1^{f_0}$	$\alpha_2^{f_0}$	$\alpha_3^{f_0}$
SPM (I)	0.634(07)	0.0327(05)	0.0550(08)	0.634(07)	0.0243(08)	0.0328(7)
SPM (II)	0.630(17)	0.0318(33)	0.0659(16)	0.630(17)	0.0258(14)	0.0352(6)
mean (III)	0.632(13)	0.0323(24)	0.0605(13)	0.632(13)	0.0251(11)	0.0340(7)
$B_c \rightarrow J/\psi$	$\alpha_1^{A_0}$	$\alpha_2^{A_0}$	$\alpha_3^{A_0}$	$\alpha_1^{A_1}$	$\alpha_2^{A_1}$	$\alpha_3^{A_1}$
SPM I	0.563(13)	0.0331(21)	0.0572(049)	0.546(19)	0.0175(29)	0.0238(54)
SPM II	0.586(44)	0.0269(58)	0.0531(110)	0.557(29)	0.0199(45)	0.0488(68)
mean III	0.574(33)	0.0300(43)	0.0552(085)	0.551(25)	0.0187(38)	0.0363(61)
$B_c \rightarrow J/\psi$	$\alpha_1^{A_2}$	$\alpha_2^{A_2}$	$\alpha_3^{A_2}$	α_1^V	α_2^V	α_3^V
SPM I	0.546(11)	0.0197(43)	0.0508(68)	0.827(26)	0.0439(54)	0.0350(135)
SPM II	0.576(38)	0.0213(24)	0.0238(86)	0.845(51)	0.0463(99)	0.0210(088)
mean III	0.561(28)	0.0205(35)	0.0373(77)	0.836(41)	0.0451(80)	0.0280(110)

Table 4-3: SPM predictions for meson masses (in GeV) that determine the locations of the timelike pole in the transition form factors computed herein, Eq. (4-12). These masses have not yet been measured; so, we present IQCD results for context [37]. (The SPM uncertainty estimate is discussed in the paragraph before that containing Eq. (4-11).)

	$m_{B_c^*}$	$m_{B_{c0}^*}$	$m_{B_{c1}}$
SPM I	6.402(20)	6.767(21)	6.880(20)
SPM II	6.382(26)	6.752(28)	6.851(26)
mean III	6.392(23)	6.760(25)	6.866(23)
IQCD	6.331(07)	6.712(19)	6.736(18)

with the analytic structure of the dressed-quark propagators [84-85], enter the complex- s^2 integration domain. In that case, straightforward numerical techniques fail.

As remarked above, such a problem was addressed in Ref. [57] via the application of perturbation theory integral representations (PTIRs) [116] for each matrix-valued function in the integrand which defines the associated matrix element. However, it is time consuming to construct accurate PTIRs; the challenge is compounded due to the

fact that the complete set of integrands involves 46 distinct scalar functions. Hence, we adopt a different approach like Ref. [92].

(I) - Considering the semileptonic decays of a fictitious $c\bar{Q}$ pseudoscalar meson: $B_{c\bar{Q}} \rightarrow \eta_{c\bar{c}}, J/\psi_{c\bar{c}}$. The corresponding Schwinger functions and the subsequent transition form factors are calculated as a function of \hat{m}_Q as it is increased from $r_{Q:c} = 1$ to $r_f^{\eta_c} = 3.17$ or $r_f^{J/\psi} = 2.93$. Next we employ the SPM, and construct \hat{m}_Q -interpolations of all transition form factors, which are then used to extrapolate every measurable feature of the matrix elements to the physical point $r_{b:c} = 4.32$, as depicted in Eq. (4-10).

(II) - We repeat these procedures from an inverted perspective. That is to say, starting from an analogous initial state, we consider the process $B_{Q\bar{b}} \rightarrow \eta_{Q\bar{Q}}, J/\psi_{Q\bar{Q}}$, with $Q\bar{Q}$ the final states and $\eta_c, J/\psi$ the quantum numbers. Then the transition form factors are calculated as a function of \hat{m}_Q , reducing it from the point $r_{Q:b} = 1$ to $r_f^{\eta_{Q\bar{Q}}} = 0.56$ or $r_f^{J/\psi_{Q\bar{Q}}} = 0.63$. Subsequently, SPM extrapolation is employed to reach the physical value, $r_{c:b} = 0.23$, Eq. (4-10). Here, the SPM uncertainty is greater due to the extrapolations of the initial and final states required.

(III) - Having completed these exercises, the outcomes are combined to produce our final results.

The reliability of our SPM procedure is readily illustrated. In Table 4-1, the meson masses were calculated straightforwardly using the Bethe-Salpeter equation with the current-quark masses in Eq. (4-10). Equally, one may compute masses following the procedures stated in (I) and (II) above. By applying (I) on $r_f^{\eta_{Q\bar{Q}}} \leq r_{Q:b} \leq 1$, one finds $m_{B_c} = 6.259(1)$ GeV; and employing (II) on $1 \leq r_{Q:c} \leq r_f^{\eta_c}$ produces $m_{B_c} = 6.281(6)$ GeV. Therefore, the final SPM result is

$$m_{B_c} = 6.270(4) \text{ GeV}, \quad (4-11)$$

which is in agreement with the directly computed value listed in Table 4-1. Repeating this exercise using the limiting current-masses in the J/ψ channel, the SPM produces the result $6.267(8)$ GeV, which is again consistent with Table 4-1.

Associated with any value of $r_{Q_1:Q_2}$, each of the transition form factors can pre-

cisely be interpolated on the physical domain adopting the following function:

$$f(t) = \alpha_1 + \alpha_2 t + \frac{\alpha_3 t^2}{m^2 - t}, \quad (4-12)$$

wherein $\alpha_{1,2,3}$ and m are functions of $r_{Q:b}$ or $r_{Q:c}$. It is the coefficients $\alpha_{1,2,3}$ for which we develop SPM interpolations. Our predictions are recorded in Table 4-2.

The pole masses in Eq. (4-12) correspond to particular mesons: $f = A_0$, then $m = m_{B_c}$; $f = f_+, V$, then $m = m_{B_c^*}$; $f = f_0$, then $m = m_{B_{c0}^*}$; and $f = A_{1,2}$, then $m = m_{B_{c1}}$. The first of these masses is computed directly with the result in Table 4-1. With our SPM method, the last three masses can be acquired by analysis of the appropriate homogeneous BSEs. Our predictions are listed in Table 4-3. Contrasted with IQCD results in Ref. [37], the mean absolute relative difference is 1.2(0.6)%. Moreover, we find $m_{B_{c0}^*} - m_{B_c^*} = 0.368(13)$ GeV, $m_{B_{c1}} - m_{B_c^*} = 0.474(05)$ GeV, in comparison with the analogous IQCD results 0.381(20) GeV, 0.405(19) GeV. The main differences are that our prediction for $m_{B_c^*}$ is 1% larger than the IQCD result, with the axial-vector-vector mass-splitting 17(6)% larger. Given empirical masses [3], the mean $1^{++} - 1^{--}$ mass-splitting is 0.416(45) GeV. Our result for $m_{B_{c1}} - m_{B_c^*}$ is 15(11)% larger than this. Hence it may be an overestimate.

4.5 Transition form factors: predictions and comparisons

In combination with the appropriate masses in Tables 4-1, 4-3 and coefficients listed in Table 4-2, our predictions for the $B_c \rightarrow \eta_c$ semileptonic transition form factors are given by Eq. (4-12). Table 4-4 records the maximum recoil ($t = 0$) value of each form factor, contrasted with recent continuum and lattice estimates, as is shown in Fig. 4-2. Different methods deliver a range of values for $f_+(0)$; nevertheless, all results fall within $\lesssim 20\%$ of the mean.

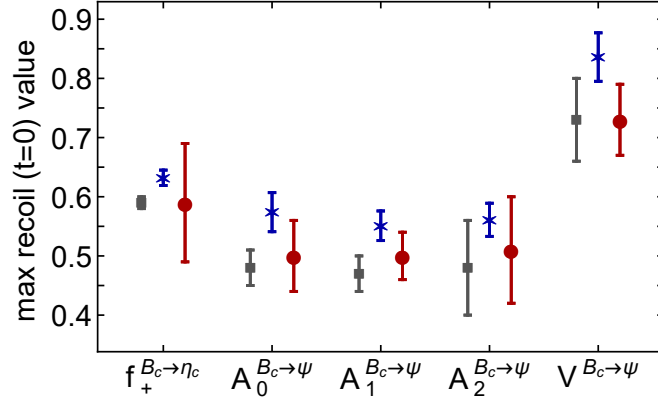


Fig. 4-2: Predicted values of all transition form factors at the maximum recoil point ($t = 0$) - blue stars. Comparisons: IQCD results [25, 32] - grey squares; and unweighted average of each column in Table. 4-4 -red circles.

Table 4-4: Maximum recoil ($t = 0$) value of each transition form factor calculated in this chapter. Comparisons are provided with other recent analyses: quark model (QM) [26-27]; phenomenology (ph) [28]; sum rules (SR) [29] modelling based on perturbative QCD (mpQCD) [30]; Salpeter equation (iBS) [31]; and IQCD [25, 32]. As additional context, we list unweighted average values for each of the quantities, evaluated with our prediction excluded (mean-e) and included (mean-i).

	$f_+^{B_c \rightarrow \eta_c}$	$A_0^{B_c \rightarrow J/\psi}$	$A_1^{B_c \rightarrow J/\psi}$	$A_2^{B_c \rightarrow J/\psi}$	$V^{B_c \rightarrow J/\psi}$
herein	0.63(1)	0.57(3)	0.55(3)	0.56(3)	0.84(4)
QM [26-27]	0.75	0.56	0.55	0.56	0.78
ph [28]	0.56	0.48	0.46	0.49	0.70
SR [29]	0.62(5)	0.54(4)	0.55(4)	0.35(3)	0.73(6)
mpQCD [30]	0.56(7)	0.40(5)	0.47(5)	0.62(6)	0.75(9)
iBS [31]	0.41	0.46	0.48	0.54	0.63
IQCD [32]	0.59(1)		0.49(3)		0.70(2)
IQCD [25]		0.48(3)	0.47(3)	0.48(8)	0.73(7)
mean-e	0.58(11)	0.49(6)	0.50(4)	0.51(9)	0.72(5)
mean-i	0.59(10)	0.50(6)	0.50(4)	0.51(9)	0.73(6)

Our calculated $B_c \rightarrow \eta_c$ transition form factors are depicted in Fig. 4-3. The difference between our predictions and the preliminary IQCD results in Ref. [32] is 10(3)%, with the IQCD values positioned uniformly below our curves. Currently, there is no further information on $B_c \rightarrow \eta_c$ available from IQCD. Hence our interpolations for calculated transition form factors can be of value in analysing future experimental

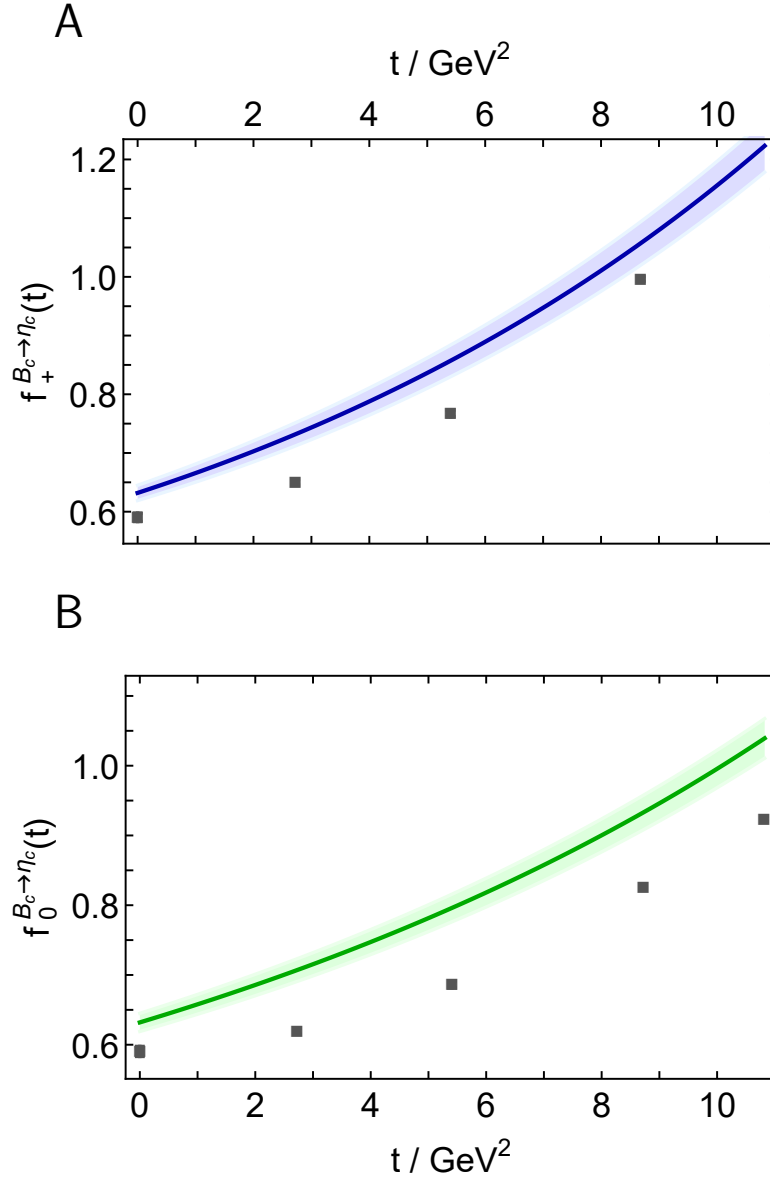


Fig. 4-3: Predicted $B_c \rightarrow \eta_c$ semileptonic transition form factors. (The shaded bands surrounding each curve express the SPM uncertainty, determined as discussed in the paragraph before that containing Eq. (4-11).) The points in both panels are preliminary IQCD results from Ref. [32].

data on the corresponding transitions.

Based on our predictions and Eqs. (4-6)-(4-8) evaluated with empirical lepton and meson masses, the $B_c \rightarrow \eta_c$ branching fractions can be obtained, which are listed in Table 4-5A. Our results agree well with other contemporary estimates.

Our predictions for the $B_c \rightarrow J/\psi$ semileptonic transition form factors are obtained from Eq. (4-12), in combination with the appropriate masses in Tables 4-1, 4-3 and the corresponding coefficients recorded in Table 4-2. Table 4-4 presents the maximum recoil ($t = 0$) value of each form factor, in comparison with the recent continuum

Table 4–5: Branching fractions calculated using our predictions for the semileptonic transition form factors in Eqs. (4–6)–(4–8) and empirical lepton and meson masses: (A) - $B_c \rightarrow \eta_c$; and (B) - $B_c \rightarrow J/\psi$. Two uncertainties are listed with our results: first - 1σ SPM uncertainty; second - from error on $|V_{cb}|$. Column 3 reports the ratio of the first two columns: $|V_{cb}|$ cancels. Comparisons are provided with other analyses: quark model (QM) [26–27]; phenomenology (ph) [28]; sum rules (SR) [29] modelling based on perturbative QCD (mpQCD) [30]; Salpeter equation (iBS) [31]; and IQCD [24–25]. (No IQCD results are available for inclusion in Panel A.) As additional context, we list an unweighted average value for each quantity, evaluated with our prediction excluded (mean-e) and included (mean-i). Branching fractions are to be multiplied by 10^{-3} .

A	$\mathcal{B}_{B_c \rightarrow \eta_c \mu \nu_\mu}$	$\mathcal{B}_{B_c \rightarrow \eta_c \tau \nu_\tau}$	R_{η_c}
herein	8.10(45)(55)	2.54(10)(17)	0.31(2)
QM[26–27]	9.5(1.9)	2.4(0.5)	0.25(7)
ph[28]	6.6(0.2)		0.31(1)
SR[29]	8.2(1.2)	2.6(0.6)	0.32(2)
mpQCD[30]	7.8(1.7)	2.4(0.4)	0.31(1)
iBS[31]	5.3(2.2)	2.2(0.7)	0.38(4)
mean-e	7.5(1.6)	2.4(0.2)	0.31(4)
mean-i	7.6(1.5)	2.4(0.2)	0.31(4)
B	$\mathcal{B}_{B_c \rightarrow J/\psi \mu \nu_\mu}$	$\mathcal{B}_{B_c \rightarrow J/\psi \tau \nu_\tau}$	$R_{J/\psi}$
herein	17.2(1.9)(1.2)	4.17(66)(28)	0.24(5)
QM [26–27]	16.7(3.3)	4.0(0.8)	0.24(7)
ph [28]	14.4(0.2)		0.26(1)
SR [29]	22.4(5.3)	5.3(1.5)	0.23(1)
mpQCD [30]	14.1(2.5)	3.8(0.6)	0.27(1)
iBS [31]	16.2(0.5)	4.3(0.1)	0.27(1)
IQCD [24–25]	15.0(1.1)(1.0)		0.258(4)
mean-e	16.5(3.1)	4.4(0.7)	0.25(2)
mean-i	16.6(2.8)	4.3(0.6)	0.25(2)

and lattice estimates. Again, different methods deliver a range of form factor values at $t = 0$, which is highlighted by Fig. 4–2; but there is no significant tension, with all values falling within $\lesssim 15\%$ of their respective means.

Our results for $B_c \rightarrow J/\psi$ transition form factors are shown in Fig. 4–4. Comparing with IQCD results presented in Ref. [25], there is semi-quantitative agreement, despite minor qualitative differences, most notably with regard to $V^{B_c \rightarrow J/\psi}(t)$ in Fig. 4–4B.

Our interpolations for the calculated transition form factors can be applied to reducing a dominant systematic error in extracting $R_{J/\psi}$ from experiment [23], paving the way to improved accuracy and more rigorous testing of the Standard Model.

Employing Eqs. (4-6)-(4-8) calculated with empirical lepton and meson masses and our predictions in Fig. 4-4, we obtain the branching fractions of $B_c \rightarrow J/\psi$, which are reported in Table 4-5B. The predictions are in good agreement with other contemporary estimates.

Fig. 4-1 emphasizes a pivotal result of our analyses, i.e., contemporary calculations within the Standard Model of the ratio $R_{J/\psi}$ in Eq. (4-1) are in agreement. Combined by the mean of their central values, they deliver $R_{J/\psi} = 0.253(16)$, which is approximately 2σ below the empirical result in Ref. [23].

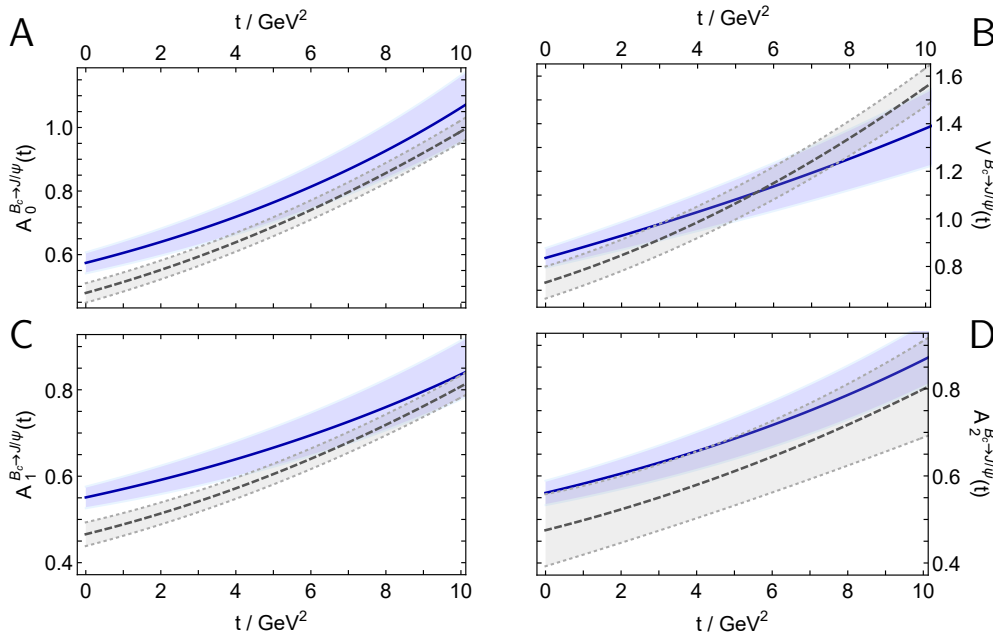


Fig. 4-4: Predicted $B_c \rightarrow J/\psi$ semileptonic transition form factors – solid blue curves within like-coloured bands, which express the 1σ uncertainty on our SPM results. Comparable IQCD results from Ref. [25] – dashed grey curves within like-coloured bands.

If subsequent, precision experiments do not result in a substantial reduction in the central value, we can draw the conclusion of the violation of lepton flavour universality in semileptonic $B_c \rightarrow J/\psi$ decays. Nevertheless, the existing empirical information is not accurate enough to support this claim. Furthermore, a convincing case could only be compiled by including information on semileptonic $B_c \rightarrow \eta_c$ decays. Our prediction

delivers $R_{\eta_c} = 0.313(22)$; while modern continuum analyses reports the mean $0.31(4)$ [Table 4–5A].

Natural extensions of this work include analogous analysis of $b \rightarrow c$ transitions in the $B_{(s)}$ meson semileptonic decays, with $D_{(s)}^{(*)}$ mesons in the final-state.

Existing investigations of Standard-Model-theoretical “ R ” ratios estimation, associated with these additional processes, report values similar to those discussed herein, where the result for pseudoscalar-meson final-state is $\sim 15\%$ larger than that for the vector-meson final-state [117-118]. Augmenting these analyses through the parameter-free unification of the obtained results with predictions for these other “ R ” ratios should contribute to increasing confidence in Standard Model predictions and strengthening any case for or against the lepton flavour universality in Nature. Moreover, the coverage of our study could be extended to include a broader range of measurable quantities [26, 97], so as to provide additional benchmarks for Standard Model tests in B_c decays.

Chapter 5 Conclusions and outlook

5.1 Conclusions

One of the greatest challenges in contemporary physics is the problem of the origin of hadron masses. There are two mass generating mechanisms in the Standard Model of elementary particle physics. One of them is related to the Higgs boson, with its contribution to the proton mass only about 2%. The other, which is more important, is embedded in QCD, the Standard Model's strong interaction piece. However, the source and impacts of this mechanism of emergent hadronic mass (EHM) remain puzzling. Dyson-Schwinger equations (DSEs) provide a nonperturbative continuum approach, which has been used successfully to expose the character of emergent phenomena in QCD. Our work is based on this method.

In the work described herein, we introduced the details of DSEs including the solutions of the quark gap equations in order to obtain the quark propagators. We also analysed the homogeneous BSE which describes the meson, and the inhomogeneous BSE which is employed to calculate the dressed-quark-W-boson vertex. In Chapter 3 we made Poincaré invariant predictions for properties of light+light and heavy+light, using the calculated quark propagators and the meson bound state amplitudes. To make such calculations possible, the statistical Schlessinger point method was employed to overcome difficulties associated with singularities of the dressed-quark propagators which enter the integration domains sampled in the calculation of observables. Using this approach, we presented predictions for transition form factors and decay widths for heavy+light meson semileptonic decays, including $B_{(s)} \rightarrow \pi(K)$, $D_s \rightarrow K$ and $D \rightarrow \pi, K$. These calculated transition form factors can be used to provide increasingly tight constraints on the CKM matrix elements. The semileptonic decays, proceeding from a heavy+light meson in the initial state to a pseudo-Nambu-Goldstone mode in the final state, also provide fresh ways of revealing the interplay between ex-

licit (Higgs-related) mass generation and EHM in the Standard Model. In Chapter 4 we delivered parameter-free predictions for the semileptonic $B_c \rightarrow \eta_c, J/\psi$ transition form factors on the complete domains of empirically accessible momentum transfers. The branching fractions calculated from the transition form factors and the ratios for τ over μ final states are obtained. Combined with other recent results, our analysis confirmed a 2σ discrepancy between the Standard Model prediction for $R_{J/\psi}$ and the single available experimental result.

5.2 Outlook

5.2.1 Semileptonic transitions of vector meson final states

Based on the existing analyses of semileptonic transitions, one can expand this approach to the study of the decays with vector meson final states such as $B_{(s)} \rightarrow \rho(K^*)$ and $D_{(s)} \rightarrow \rho(K^*)$. This is important because it will deliver a comprehensive, unified set of parameter-free predictions for leptonic decay constants and heavy-to-light semileptonic transitions and thereby enable deeper and wider understanding of the roles played by EHM, Higgs-boson couplings, and the interference between them in forming observable phenomena; especially, their effects on the values of the CKM matrix.

5.2.2 Baryons

In the past few decades, continuum field theory methods have made significant progress in the theoretical aspects of bound state problems, especially for mesons. Although the proton has been discovered for nearly a century, the internal structure of which has been extensively investigated, there are still many difficulties in analyzing the proton theoretically. Recent truly three-body computations [119-120] are only accessible for baryons constituted from equal-flavor quarks, hence in the near future we expect to study the following.

1. Faddeev equation with baryons constituted from unequal-flavor quarks.

This work is expected to provide us information for baryons like Λ , Σ , Ξ , and so on,

which is the basis of studying the semileptonic decays of baryons.

2. Distribution amplitudes (DAs) and distribution functions (DFs) of baryons.

DAs are the nearest things in quantum field theory to a Schrödinger wave function, which, combined with the DFs, can provide detailed structural information of baryon.

3. Exotic hybrid states.

Hybrid states have been widely considered in recent years. The simplest examples are exotic mesons, defined as a meson-like system with an additional valence gluon component. This is a three-body problem. It has been tackled using Faddeev equation methods [121], but should ultimately be treated using a fully three-body approach.

Appendix A Euclidean conventions

A.1 Dirac structures

In the work described herein, we use conventions, with the following notations:

$$a \cdot b = \delta_{\mu\nu} a_\mu b_\nu = \sum_{i=1}^4 a_i b_i, \quad (\text{A-1})$$

and

$$\delta_{\mu\nu} = \begin{pmatrix} +1 & 0 & 0 & 0 \\ 0 & +1 & 0 & 0 \\ 0 & 0 & +1 & 0 \\ 0 & 0 & 0 & +1 \end{pmatrix}. \quad (\text{A-2})$$

For Dirac matrix, we have

$$\{\gamma_\mu, \gamma_\nu\} = 2\delta_{\mu\nu}, \quad (\text{A-3})$$

and γ_5 is defined as:

$$\text{Tr} [\gamma_5 \gamma_\lambda \gamma_\mu \gamma_\nu \gamma_\rho] = 4\epsilon_{\lambda\mu\nu\rho}, \quad (\text{A-4})$$

and

$$\gamma_5 = \gamma_1 \gamma_2 \gamma_3 \gamma_4, \quad (\text{A-5})$$

where $\epsilon_{\lambda\mu\nu\rho}$ is Levi-Civita Tensor.

The Dirac-like representation of these matrices used here is

$$\begin{aligned}
 \gamma_1 &= \begin{pmatrix} 0 & 0 & 0 & -i \\ 0 & 0 & -i & 0 \\ 0 & +i & 0 & 0 \\ +i & 0 & 0 & 0 \end{pmatrix} & \gamma_2 &= \begin{pmatrix} 0 & 0 & 0 & -1 \\ 0 & 0 & +1 & 0 \\ 0 & +1 & 0 & 0 \\ -1 & 0 & 0 & 0 \end{pmatrix} \\
 \gamma_3 &= \begin{pmatrix} 0 & 0 & -i & 0 \\ 0 & 0 & 0 & +i \\ +i & 0 & 0 & 0 \\ 0 & -i & 0 & 0 \end{pmatrix} & \gamma_4 &= \begin{pmatrix} 0 & 0 & +1 & 0 \\ 0 & 0 & 0 & +1 \\ +1 & 0 & 0 & 0 \\ 0 & +1 & 0 & 0 \end{pmatrix}.
 \end{aligned} \tag{A-6}$$

A.2 Coordinates

We express four-momenta via hyperspherical coordinates:

$$p^\mu = \sqrt{p^2} \begin{pmatrix} \sqrt{1-z^2}\sqrt{1-y^2}\sin\phi \\ \sqrt{1-z^2}\sqrt{1-y^2}\cos\phi \\ \sqrt{1-z^2}y \\ z \end{pmatrix} = \sqrt{p^2} \begin{pmatrix} \sin\psi\sin\theta\sin\phi \\ \sin\psi\sin\theta\cos\phi \\ \sin\psi\cos\theta \\ \cos\psi \end{pmatrix}, \tag{A-7}$$

wherein p describes the on-shell momentum of a bound state with mass M , $p^2 = -M^2$.

A four-momentum integration reads:

$$\int_p := \int \frac{d^4p}{(2\pi)^4} = \frac{1}{(2\pi)^4} \frac{1}{2} \int_0^\infty dp^2 p^2 \int_{-1}^1 dz \sqrt{1-z^2} \int_{-1}^1 dy \int_0^{2\pi} d\phi. \tag{A-8}$$

Appendix B Solving the Bethe-Salpeter equation

B.1 Dressed-quark propagators in the complex plane

Since in Euclidean space, we have $P^2 < 0$ for all physical systems, the variables q_{\pm}, k_{\pm} in Eq. (2-23) are complex valued. Hence, we need to solve gap equations in the complex plane, which is typically implemented in the rest frame. Namely,

$$P_{\mu} = (0, 0, 0, iM_X). \quad (\text{B-1})$$

The q_{\pm}^2 domain in the complex plane is

$$\text{Re}(q_{\pm}^2) = q^2 - \frac{M_X^2}{4}, \quad \text{Im}(q_{\pm}^2) = \pm P \cdot q M_X. \quad (\text{B-2})$$

For arbitrary momentum q , the complex plane of q_{\pm}^2 can be depicted by the area colored orange in Fig. B-1. A vertical path at the infinite opening of the parabola is taken to form a closed path C. Herein, the Cauchy integral is employed to obtain the value of the dressed-quark propagators in this area, in the case that there are no singularities in this complex plane.

B.2 The Bethe-Salpeter equation in the rest frame

In the rest frame, the momentum of meson, Eq. (B-1) only has one nonzero component, P_4 . Thus, the relative momentum, p_{μ} , can be expressed as

$$p_{\mu} = (0, 0, \sqrt{1 - z_p^2}, z_p) \sqrt{p^2}, \quad (\text{B-3})$$

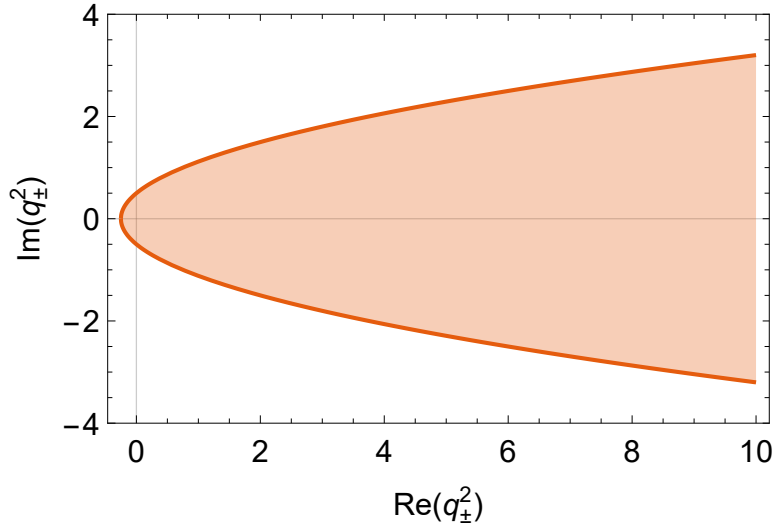


Fig. B-1: Domain of the complex plane sampled by the dressed-quark propagator.

and for loop momentum, the angle ϕ can be integrated analytically first, viz.,

$$q_\mu = (0, \sqrt{1-y_q^2}\sqrt{1-z_q^2}, y_q\sqrt{1-z_q^2}, z_q)\sqrt{q^2}. \quad (\text{B-4})$$

The BS amplitudes, Eq. (2-27), can be rewritten as

$$\Gamma_X(p, P) = \sum_i \tau_X^i(p, P) F_X^i(p^2, z, P^2). \quad (\text{B-5})$$

Inserting the above amplitudes into Eq. (2-23) and projecting both sides on the bases $\tau_X^i(p, P)$, one can obtain

$$\begin{aligned} \sum_j^{N_X} \text{tr}[\tau_X^i(p, P) \tau_X^j(p, P)] F_X^j(p^2, z_p; P^2) &= -\frac{4}{3} Z_2^2 \int \frac{d^4 q}{(2\pi)^4} \mathcal{G}(k^2) T_{\mu\nu}(k) \sum_j^{N_X} F_X^j(q^2, z_q; P^2) \\ &\quad \text{tr}[\tau_X^i(p, P) \gamma_\mu S(q_+) \tau_X^j(q, P) S(q_-) \gamma_\nu]. \end{aligned} \quad (\text{B-6})$$

If we define $\text{tr}[\tau_X^i(p, P) \tau_X^j(p, P)] = M_X^{i,j}(p^2, z_p; P^2)$, the integral can be discretized as

$$M_X^{i,j}(p^2, z_p; P^2) F_X^j(p^2, z_p; P^2) = \sum_{q^2} \sum_{z_q} \mathcal{W}_X^{i,j}(p^2, z_p, q^2, z_q; P^2) F_X^j(q^2, z_q; P^2), \quad (\text{B-7})$$

where

$$\begin{aligned} \mathcal{W}_X^{i,j}(p^2, z_p, q^2, z_q; P^2) = & -\frac{4Z_2^2}{3(2\pi)^3} w[q^2] w[z_q] \sum_{y_q} w[y_q] \mathcal{G}(k^2) T_{\mu\nu}(k) \\ & \times \text{tr}[\tau_X^i(k, P) \gamma_\mu S(q_+) \tau_X^j(q, P) S(q_-) \gamma_\nu], \end{aligned} \quad (\text{B-8})$$

and $\{q^2, z_q, y_q\}$ are discretized integral points; $\{w[q^2], w[z_q], w[y_q]\}$ are the weights of the corresponding integral points. By taking the inverse of $M_X^{i,j}$ in Eq. (B-7), we have

$$\begin{aligned} F_X^j(p^2, z_p; P^2) &= \sum_{q^2} \sum_{z_q} (M_X^{i,j})^{-1}(p^2, z_p; P^2) \omega_X^{i,j}(p^2, z_p, q^2, z_q; P^2) F_X^j(q^2, z_q; P^2) \\ &= \sum_{q^2} \sum_{z_q} K_X^{i,j}(p^2, z_p, q^2, z_q; P^2) F_X^j(q^2, z_q; P^2). \end{aligned} \quad (\text{B-9})$$

After discretizing $\{p^2, z_p\}$ and F_X , the above equation can be regarded as an eigenvalue equation:

$$\lambda(P^2) \vec{F}_X(P^2) = \mathcal{K}_X(P^2) \vec{F}_X(P^2). \quad (\text{B-10})$$

The solution at $\lambda(P^2 = -M_x^2) = 1$ corresponds to meson bound state. The Fig. B-2 shows the evolution of eigenvalues with meson masses.

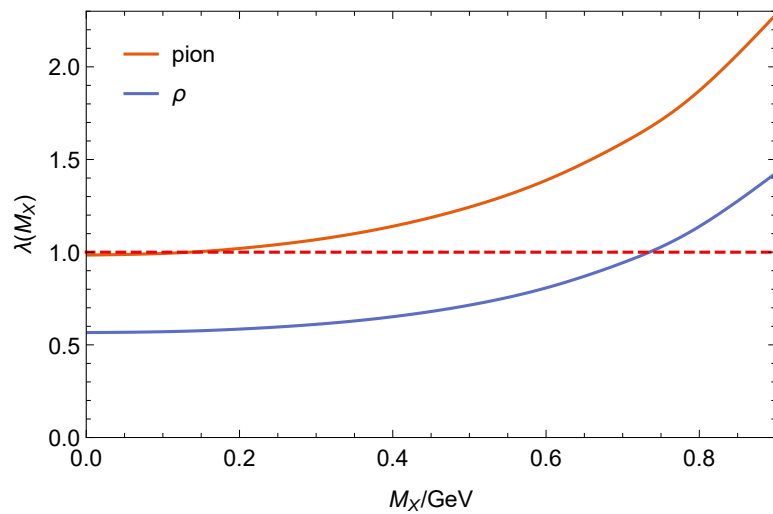


Fig. B-2: Evolution with p^2 of the eigenvalues of Eq. B-10 for pion and ρ -meson channels.

B.3 Bethe-Salpeter equation in the moving frame

To introduce the procedure of solving the BSE in the moving frame, we should start by redefining the meson momentum as

$$P_\mu = (0, 0, a, b), \quad (\text{B-11})$$

where $a^2 + b^2 = -M_X^2$. Hence, there should be one additional dimension in the relative momentum, viz.,

$$p_\mu = (0, \sqrt{1 - y_p^2} \sqrt{1 - z_p^2}, y_p \sqrt{1 - z_p^2}, z_p) \sqrt{p^2}. \quad (\text{B-12})$$

The loop momentum q_μ takes the following form:

$$q_\mu = (\sqrt{1 - y_q^2} \sqrt{1 - z_q^2} \sin(\phi), \sqrt{1 - y_q^2} \sqrt{1 - z_q^2} \cos(\phi), y_q \sqrt{1 - z_q^2}, z_q) \sqrt{q^2}. \quad (\text{B-13})$$

The BS amplitudes can be expressed as:

$$\Gamma_X(p, P) = \sum_i \tau_X^i(p, P) F_X^i(p^2, z_p, y_p, P^2). \quad (\text{B-14})$$

Thus, Eq. (B-9) become

$$\begin{aligned} & F_X^j(p^2, z_p, y_p, P^2) \\ &= \sum_{q^2} \sum_{z_q} \sum_{y_q} (M_X^{i,j})^{-1}(p^2, z_p, y_p; P^2) \mathcal{W}_X^{i,j}(p^2, z_p, y_p, q^2, z_q, y_q; P^2) F_X^j(q^2, z_q, y_q; P^2) \\ &= \sum_{q^2} \sum_{z_q} \sum_{y_q} K_X^{i,j}(p^2, z_p, y_p, q^2, z_q, y_q; P^2) F_X^j(q^2, z_q, y_q; P^2). \end{aligned} \quad (\text{B-15})$$

Analogously, this equation can also be solved as an eigenvalue equation, with two additional dimensions for $K_X^{i,j}$, which will result in huge demand for computing resources.

A more convenient and fast method can be realized by analytic continuation of the results from the rest frame. In the rest frame, BSEs can be solved to obtain the

scalar functions $F_X^i(p^2, z; P^2)$, which can be expanded using the first kind of Chebyshev polynomial $T_m(z)$, viz.,

$$F_X^i(p^2, z; P^2) = \sum_{m=0}^M \zeta_m^i(p^2) T_m(z), \quad (\text{B-16})$$

where $\zeta_m^i(p^2)$ are the series of points. This formula can be used to extend the q^2 and $z = \frac{q \cdot P}{\sqrt{q^2 P^2}}$ dependence to the complex plane. For $\zeta_m^i(p^2)$, the simplest way to extend q^2 is cubic interpolation. Fig. B-3 depicts the $\zeta_m^i(p^2)$ for pion, and in Fig. B-4, the pion elastic form factor obtained via the two methods are compared.

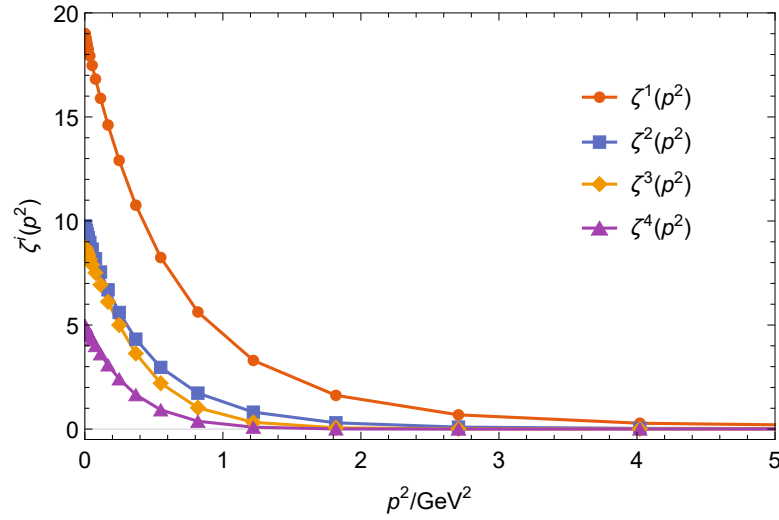


Fig. B-3: $\zeta_m^i(p^2)$ from the pion's BS amplitudes. Here, we employ a convenient normalization for the zeroth Chebyshev moment by setting $T_0 = 1/\sqrt{2}$ [33].

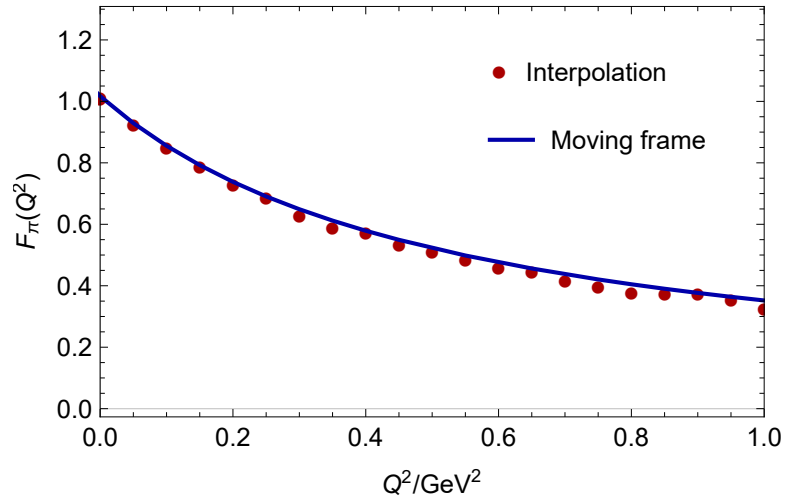


Fig. B-4: Pion elastic form factor obtained via two methods introduced above. The interpolation points are given by Eq. (B-16) - analytic continuation; and the curve is obtained from Eq. (B-15) - direct solution.

Appendix C Schlessinger Point Method

C.1 Introduction of Schlessinger Point Method

For a set of N data points,

$$(x_i, y_i), i = 1, 2 \dots N, \quad (\text{C-1})$$

the SPM constructs the rational interpolation $C_{N,M}(x)$ given by

$$C_N(x) = \frac{P(x)}{Q(x)} = \frac{y_1}{1+} \frac{a_1(x-x_1)}{1+} \frac{a_2(x-x_2)}{1+} \dots \frac{a_{N-1}(x-x_{N-1})}{1}, \quad (\text{C-2})$$

wherein $\frac{1}{1+}\xi := \frac{1}{1+\xi}$, $P(x)$ and $Q(x)$ are polynomials in x which form the numerator and denominator of the fraction respectively. The coefficients a_i can be obtained recursively:

$$\begin{aligned} a_1 &= \frac{y_1/y_2 - 1}{x_2 - x_1}, \\ a_i &= \frac{1}{x_i - x_{i+1}} \left[1 + \frac{a_{i-1}(x_{i+1} - x_{i-1})}{1+} \frac{a_{i-2}(x_{i+1} - x_{i-2})}{1+} \dots \frac{a_1(x_{i+1} - x_1)}{1 - y_1/y_{i+1}} \right]. \end{aligned} \quad (\text{C-3})$$

The order of $[P(x), Q(x)]$ is determined by the following statement:

If N is an even number, then: $[N/2 - 1, N/2]$;

If N is an odd number, then: $[(N - 1)/2, (N - 1)/2]$.

C.2 Examples

As an exemplar, we reconstitute the function $f(x) = e^x$ using the SPM and show the comparison between the function curve and the SPM interpolation, which is depicted in the following figure:

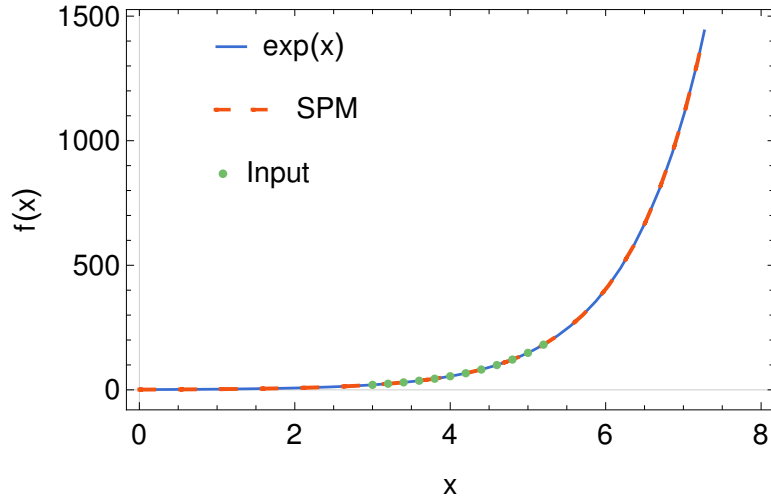


Fig. C-1: Comparison between the function curve and the SPM interpolation. The green points are the input data extracted from the function curve; the red dashed line is the interpolation result from SPM.

One of the examples of the applications of SPM in this work is the prediction of $f_+(t = 0)$ for $B_c \rightarrow \eta_c$, which is shown in Fig. C-2. Evidently, the SPM returns compatible results independent of the method used to approach the physical parameters.

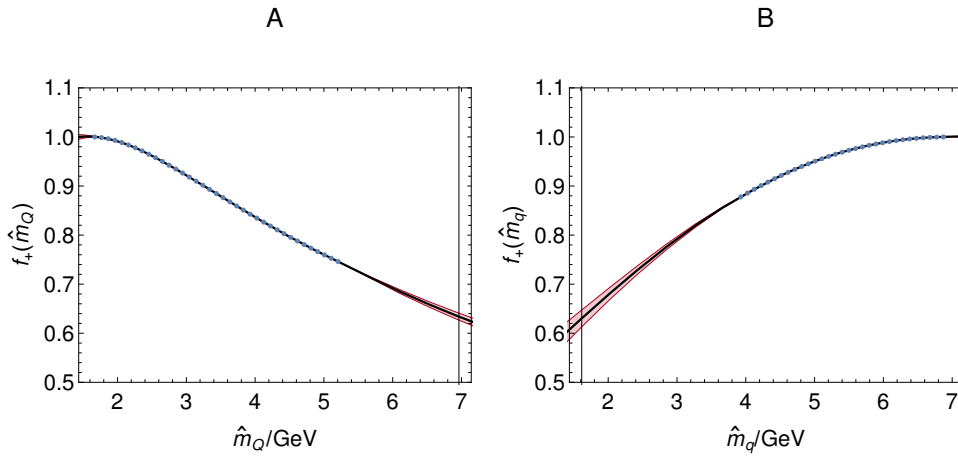


Fig. C-2: Extrapolations in two directions: A. Fix the mass of light quark c and increase the mass of the other quark, initiating from the value of c quark mass (SPM (I)); B. Fix the mass of heavy quark b and decrease the mass of the other quark, initiating from the value of b quark mass (SPM (II)).

References

- [1] Zhu-Fang Cui, Jin-Li Zhang, Daniele Binosi, Feliciano de Soto, Cédric Mezrag, Joannis Papavassiliou, Craig D Roberts, Jose Rodríguez-Quintero, Jorge Segovia, and Savvas Zafeiropoulos. Effective charge from lattice QCD. *Chin. Phys. C*, 44(8):083102, 2020.
- [2] Insights into the emergence of mass from studies of pion and kaon structure. *Prog. Part. Nucl. Phys.*, 120:103883, 2021.
- [3] P.A. Zyla et al. Review of Particle Physics. *PTEP*, 2020(8):083C01, 2020.
- [4] L. Widhalm, et al. Measurement of $D^0 \rightarrow \pi l \nu (K l \nu)$ Form Factors and Absolute Branching Fractions. *Phys. Rev. Lett.*, 97:061804, Aug 2006.
- [5] D. Besson, et al. Improved measurements of D meson semileptonic decays to π and K mesons. *Phys. Rev. D*, 80:032005, Aug 2009.
- [6] J. P. Lees, et al. Measurement of the $D^0 \rightarrow \pi^- e^+ \nu_e$ differential decay branching fraction as a function of q^2 and study of form factor parametrizations. *Phys. Rev. D*, 91:052022, Mar 2015.
- [7] M. Ablikim, et al. Study of dynamics of $D^0 \rightarrow K^- e^+ \nu_e$ and $D^0 \rightarrow \pi^- e^+ \nu_e$ decays. *Phys. Rev. D*, 92:072012, Oct 2015.
- [8] V. Lubicz, L. Riggio, G. Salerno, S. Simula, and C. Tarantino. Scalar and vector form factors of $D \rightarrow \pi(K) \ell \nu$ decays with $N_f = 2 + 1 + 1$ twisted fermions. *Phys. Rev. D*, 96:054514, Sep 2017.
- [9] M. Ablikim, et al. First Measurement of the Form Factors in $D_s^+ \rightarrow K^0 e^+ \nu_e$ and $D_s^+ \rightarrow K^{*0} e^+ \nu_e$ Decays. *Phys. Rev. Lett.*, 122:061801, Feb 2019.
- [10] Yasmine Sara Amhis et al. Averages of b-hadron, c-hadron, and τ -lepton properties as of 2018. *Eur. Phys. J. C*, 81(3):226, 2021.
- [11] P. del Amo Sanchez, et al. Study of $B \rightarrow \pi l \nu$ and $B \rightarrow \rho l \nu$ decays and determination of $|V_{ub}|$. *Phys. Rev. D*, 83:032007, Feb 2011.
- [12] H. Ha, et al. Measurement of the decay $B^0 \rightarrow \pi^- \ell^+ \nu$ and determination of $|V_{ub}|$. *Phys. Rev. D*, 83:071101, Apr 2011.

- [13] J. P. Lees, et al. Branching fraction and form-factor shape measurements of exclusive charmless semileptonic B decays, and determination of $|V_{ub}|$. *Phys. Rev. D*, 86:092004, Nov 2012.
- [14] A. Sibidanov, et al. Study of exclusive $B \rightarrow X_u \ell \nu$ decays and extraction of $|V_{ub}|$ using full reconstruction tagging at the Belle experiment. *Phys. Rev. D*, 88:032005, Aug 2013.
- [15] C. M. Bouchard, G. Peter Lepage, Christopher Monahan, Heechang Na, and Junko Shigemitsu. $B_s \rightarrow K \ell \nu$ form factors from lattice QCD. *Phys. Rev. D*, 90:054506, Sep 2014.
- [16] J. M. Flynn, T. Izubuchi, T. Kawanai, C. Lehner, A. Soni, R. S. Van de Water, and O. Witzel. $B \rightarrow \pi \ell \nu$ and $B_s \rightarrow K \ell \nu$ form factors and $|V_{ub}|$ from 2 + 1-flavor lattice QCD with domain-wall light quarks and relativistic heavy quarks. *Phys. Rev. D*, 91:074510, Apr 2015.
- [17] R. Aaij, et al. First Observation of the Decay $B_s^0 \rightarrow K^- \mu^+ \nu_\mu$ and a Measurement of $|V_{ub}|/|V_{cb}|$. *Phys. Rev. Lett.*, 126:081804, Feb 2021.
- [18] Yue-Liang Wu, Ming Zhong, and Ya-Bing Zuo. $B_{(s)}, D_{(s)} \rightarrow \pi, K, \eta, \rho, K^*, \omega, \phi$ Transition Form Factors and Decay Rates with Extraction of the CKM parameters $|V(ub)|$, $|V(cs)|$, $|V(cd)|$. *Int. J. Mod. Phys. A*, 21:6125–6172, 2006.
- [19] R. N. Faustov and V. O. Galkin. Charmless weak B_s decays in the relativistic quark model. *Phys. Rev. D*, 87:094028, May 2013.
- [20] Zhen-Jun Xiao, Ying-Ying Fan, Wen-Fei Wang, and Shan Cheng. The semileptonic decays of B/B_s meson in the perturbative QCD approach: A short review. *Chin. Sci. Bull.*, 59:3787–3800, 2014.
- [21] A. Bazavov, et al. $B_s \rightarrow K \ell \nu$ decay from lattice QCD. *Phys. Rev. D*, 100:034501, Aug 2019.
- [22] Sergi González-Solís, Pere Masjuan, and Camilo Rojas. Padé approximants to $B \rightarrow \pi \ell \nu_\ell$ and $B_s \rightarrow K \ell \nu_\ell$ and determination of $|V_{ub}|$. *Phys. Rev. D*, 104:114041, Dec 2021.
- [23] R. Aaij et al. Measurement of the ratio of branching fractions $\mathcal{B}(B_c^+ \rightarrow J/\psi \tau^+ \nu_\tau)/\mathcal{B}(B_c^+ \rightarrow J/\psi \mu^+ \nu_\mu)$. *Phys. Rev. Lett.*, 120(12):121801, 2018.

- [24] Judd Harrison, Christine T. H. Davies, and Andrew Lytle. $R(J/\psi)$ and $B_c^- \rightarrow J/\psi \ell^- \bar{\nu}_\ell$ Lepton Flavor Universality Violating Observables from Lattice QCD. *Phys. Rev. Lett.*, 125:222003, Nov 2020.
- [25] Judd Harrison, Christine T. H. Davies, and Andrew Lytle. $B_c \rightarrow J/\psi$ form factors for the full q^2 range from lattice QCD. *Phys. Rev. D*, 102:094518, Nov 2020.
- [26] C. T. Tran, M. A. Ivanov, J. G. Körner, and P. Santorelli. Implications of new physics in the decays $B_c \rightarrow (J/\psi, \eta_c) \tau \nu$. *Phys. Rev. D*, 97:054014, Mar 2018.
- [27] Aidon Issadykov and Mikhail A. Ivanov. The decays $B_c \rightarrow J/\psi + \bar{\ell} \nu_\ell$ and $B_c \rightarrow J/\psi + \pi(K)$ in covariant confined quark model. *Phys. Lett. B*, 783:178–182, 2018.
- [28] Wei Wang and Ruilin Zhu. Model independent investigation of the $R_{J/\psi, \eta_c}$ and ratios of decay widths of semileptonic B_c decays into a P-wave charmonium. *Int. J. Mod. Phys. A*, 34(31):1950195, 2019.
- [29] Domagoj Leljak, Blaženka Melić, and Monalisa Patra. On lepton flavour universality in semileptonic $B_c \rightarrow \eta_c, J/\psi$ decays. *Journal of High Energy Physics*, 2019(5):94, May 2019.
- [30] Xue-Qing Hu, Su-Ping Jin, and Zhen-Jun Xiao. Semileptonic decays $B_c \rightarrow (\eta_c, J/\psi) l \bar{\nu}_l$ in the "PQCD + Lattice" approach. *Chin. Phys. C*, 44(2):023104, 2020.
- [31] Tian Zhou, Tianhong Wang, Yue Jiang, Xiao-Ze Tan, Geng Li, and Guo-Li Wang. Relativistic calculations of $R(D^{(*)})$, $R(D_s^{(*)})$, $R(\eta_c)$ and $R(J/\psi)$. *Int. J. Mod. Phys. A*, 35(17):2050076, 2020.
- [32] Andrew Lytle, Brian Colquhoun, Christine Davies, Jonna Koponen, and Craig McNeile. B_c decays from highly improved staggered quarks and NRQCD. *PoS, LATTICE2016*:281, 2016.
- [33] Martin Oettel. Baryons as relativistic bound states of quark and diquark. Other thesis, 12 2000.
- [34] C. T. H. Davies, C. McNeile, E. Follana, G. P. Lepage, H. Na, and J. Shigemitsu. Update: Precision D_s decay constant from full lattice QCD using very fine lattices. *Phys. Rev. D*, 82:114504, Dec 2010.

- [35] C. McNeile, C. T. H. Davies, E. Follana, K. Hornbostel, and G. P. Lepage. Heavy meson masses and decay constants from relativistic heavy quarks in full lattice QCD. *Phys. Rev. D*, 86:074503, Oct 2012.
- [36] B. Colquhoun, C. T. H. Davies, J. Kettle, J. Koponen, A. T. Lytle, R. J. Dowdall, and G. P. Lepage. B -meson decay constants: A more complete picture from full lattice QCD. *Phys. Rev. D*, 91:114509, Jun 2015.
- [37] Nilmani Mathur, M. Padmanath, and Sourav Mondal. Precise Predictions of Charmed-Bottom Hadrons from Lattice QCD. *Phys. Rev. Lett.*, 121:202002, Nov 2018.
- [38] J. J. Aubert, U. Becker, P. J. Biggs, J. Burger, M. Chen, G. Everhart, P. Goldhagen, J. Leong, T. McCorriston, T. G. Rhoades, M. Rohde, Samuel C. C. Ting, Sau Lan Wu, and Y. Y. Lee. Experimental Observation of a Heavy Particle J . *Phys. Rev. Lett.*, 33:1404–1406, Dec 1974.
- [39] J. E. Augustin, et al. Discovery of a Narrow Resonance in e^+e^- Annihilation. *Phys. Rev. Lett.*, 33:1406–1408, Dec 1974.
- [40] S. W. Herb, D. C. Hom, L. M. Lederman, J. C. Sens, H. D. Snyder, J. K. Yoh, J. A. Appel, B. C. Brown, C. N. Brown, W. R. Innes, K. Ueno, T. Yamanouchi, A. S. Ito, H. Jöstlein, D. M. Kaplan, and R. D. Kephart. Observation of a Dimuon Resonance at 9.5 GeV in 400-GeV Proton-Nucleus Collisions. *Phys. Rev. Lett.*, 39:252–255, Aug 1977.
- [41] M. L. Perl, et al. Evidence for Anomalous Lepton Production in $e^+ - e^-$ Annihilation. *Phys. Rev. Lett.*, 35:1489–1492, Dec 1975.
- [42] Haim Harari. QUARKS AND LEPTONS: THE GENERATION PUZZLE. In *The Jerusalem Einstein Centennial Symposium*, 7 1979.
- [43] H. Albrecht et al. Observation of $B^0 - \bar{B}^0$ mixing. *Phys. Lett. B*, 192(1):245–252, 1987.
- [44] S. Abachi et al. Observation of the Top Quark. *Phys. Rev. Lett.*, 74:2632–2637, Apr 1995.
- [45] F. Abe et al. Observation of Top Quark Production in $\bar{p}p$ Collisions with the Collider Detector at Fermilab. *Phys. Rev. Lett.*, 74:2626–2631, Apr 1995.
- [46] Y. Fukuda, T. Hayakawa, E. Ichihara, K. Inoue, et al. Evidence for oscillation of atmospheric neutrinos. *Phys. Rev. Lett.*, 81:1562–1567, Aug 1998.

-
- [47] Q. R. Ahmad, R. C. Allen, T. C. Andersen, et al. Direct evidence for neutrino flavor transformation from neutral-current interactions in the sudbury neutrino observatory. *Phys. Rev. Lett.*, 89:011301, Jun 2002.
- [48] William J. Marciano and Heinz Pagels. Quantum Chromodynamics: A Review. *Phys. Rept.*, 36:137, 1978.
- [49] Gernot Eichmann, Helios Sanchis-Alepuz, Richard Williams, Reinhard Alkofer, and Christian S. Fischer. Baryons as relativistic three-quark bound states. *Prog. Part. Nucl. Phys.*, 91:1–100, 2016.
- [50] Volker D. Burkert and Craig D. Roberts. Colloquium: Roper resonance: Toward a solution to the fifty year puzzle. *Rev. Mod. Phys.*, 91:011003, Mar 2019.
- [51] Si-xue Qin and Craig D Roberts. Impressions of the Continuum Bound State Problem in QCD. *Chin. Phys. Lett.*, 37(12):121201, 2020.
- [52] Craig D. Roberts. Empirical Consequences of Emergent Mass. *Symmetry*, 12(9), 2020.
- [53] Lei Chang, I. C. Cloet, J. J. Cobos-Martinez, C. D. Roberts, S. M. Schmidt, and P. C. Tandy. Imaging dynamical chiral symmetry breaking: pion wave function on the light front. *Phys. Rev. Lett.*, 110(13):132001, 2013.
- [54] Daniele Binosi, Lei Chang, Minghui Ding, Fei Gao, Joannis Papavassiliou, and Craig D. Roberts. Distribution amplitudes of heavy-light mesons. *Phys. Lett. B*, 790:257–262, 2019.
- [55] Minghui Ding, Khépani Raya, Daniele Binosi, Lei Chang, Craig D Roberts, and Sebastian M. Schmidt. Symmetry, symmetry breaking, and pion parton distributions. *Phys. Rev. D*, 101(5):054014, 2020.
- [56] Minghui Ding, Khépani Raya, Daniele Binosi, Lei Chang, Craig D Roberts, and Sebastian M Schmidt. Drawing insights from pion parton distributions. *Chin. Phys. C*, 44(3):031002, 2020.
- [57] L. Chang, I. C. Cloët, C. D. Roberts, S. M. Schmidt, and P. C. Tandy. Pion Electromagnetic Form Factor at Spacelike Momenta. *Phys. Rev. Lett.*, 111:141802, Oct 2013.
- [58] Minghui Ding, Khépani Raya, Adnan Bashir, Daniele Binosi, Lei Chang, Muyang Chen, and Craig D. Roberts. $\gamma^* \gamma \rightarrow \eta, \eta'$ transition form factors. *Phys. Rev. D*, 99:014014, Jan 2019.

- [59] Makoto Kobayashi and Toshihide Maskawa. CP Violation in the Renormalizable Theory of Weak Interaction. *Prog. Theor. Phys.*, 49:652–657, 1973.
- [60] Nicola Cabibbo. Unitary Symmetry and Leptonic Decays. *Phys. Rev. Lett.*, 10:531–533, 1963.
- [61] I. S. Towner and J. C. Hardy. The evaluation of V_{ud} and its impact on the unitarity of the Cabibbo-Kobayashi-Maskawa quark-mixing matrix. *Rept. Prog. Phys.*, 73:046301, 2010.
- [62] F. Ambrosino et al. Measurement of the $K(L)$ meson lifetime with the KLOE detector. *Phys. Lett. B*, 626:15–23, 2005.
- [63] T. Alexopoulos et al. Measurements of semileptonic $K(L)$ decay form-factors. *Phys. Rev. D*, 70:092007, 2004.
- [64] E. Abouzaid et al. Improved $K_L \rightarrow \pi^\pm e^\mp \nu$ form factor and phase space integral with reduced model uncertainty. *Phys. Rev. D*, 74:097101, 2006.
- [65] F. Ambrosino et al. Measurement of the form-factor slopes for the decay $K(L) \rightarrow \pi^\pm e^\mp \nu$ with the KLOE detector. *Phys. Lett. B*, 636:166–172, 2006.
- [66] A. Lai et al. Measurement of $K^0(e_3)$ form-factors. *Phys. Lett. B*, 604:1–10, 2004.
- [67] O. P. Yushchenko et al. High statistic measurement of the $K^- \rightarrow \pi^0 e^- \nu$ decay form-factors. *Phys. Lett. B*, 589:111–117, 2004.
- [68] D. Babusci et al. Measurement of the absolute branching ratio of the $K^+ \rightarrow \pi^+ \pi^- \pi^+(\gamma)$ decay with the KLOE detector. *Phys. Lett. B*, 738:128–133, 2014.
- [69] M. Ablikim, et al. Analysis of $D^+ \rightarrow \bar{K}^0 e^+ \nu_e$ and $D^+ \rightarrow \pi^0 e^+ \nu_e$ semileptonic decays. *Phys. Rev. D*, 96:012002, Jul 2017.
- [70] Si-xue Qin, Lei Chang, Yu-xin Liu, Craig D. Roberts, and David J. Wilson. Interaction model for the gap equation. *Phys. Rev. C*, 84:042202, Oct 2011.
- [71] Daniele Binosi, Lei Chang, Joannis Papavassiliou, and Craig D. Roberts. Bridging a gap between continuum-QCD and ab initio predictions of hadron observables. *Phys. Lett. B*, 742:183–188, 2015.
- [72] Si-xue Qin, Lei Chang, Yu-xin Liu, Craig D. Roberts, and David J. Wilson. Investigation of rainbow-ladder truncation for excited and exotic mesons. *Phys. Rev. C*, 85:035202, Mar 2012.

- [73] Lei Chang, Yu-Xin Liu, and Craig D. Roberts. Dressed-Quark Anomalous Magnetic Moments. *Phys. Rev. Lett.*, 106:072001, Feb 2011.
- [74] Lei Chang and Craig D. Roberts. Sketching the Bethe-Salpeter Kernel. *Phys. Rev. Lett.*, 103:081601, Aug 2009.
- [75] Lei Chang and Craig D. Roberts. Tracing masses of ground-state light-quark mesons. *Phys. Rev. C*, 85:052201, May 2012.
- [76] Si-Xue Qin and Craig D. Roberts. Resolving the Bethe–Salpeter Kernel. *Chin. Phys. Lett.*, 38(7):071201, 2021.
- [77] Pieter Maris, Craig D. Roberts, and Peter. C. Tandy. Pion mass and decay constant. *Phys. Lett. B*, 420:267–273, 1998.
- [78] Si-Xue Qin, Craig D. Roberts, and Sebastian M. Schmidt. Ward–Green–Takahashi identities and the axial-vector vertex. *Phys. Lett. B*, 733:202–208, 2014.
- [79] Si xue Qin, Craig D. Roberts, and Sebastian M. Schmidt. Spectrum of Light- and Heavy-Baryons. *Few-Body Systems*, 60:1–16, 2019.
- [80] M. S. Bhagwat and P. Maris. Vector meson form factors and their quark-mass dependence. *Phys. Rev. C*, 77:025203, 2008.
- [81] Jing Chen, Minghui Ding, Lei Chang, and Yu-xin Liu. Two Photon Transition Form Factor of $\bar{c}c$ Quarkonia. *Phys. Rev. D*, 95(1):016010, 2017.
- [82] M. S. Bhagwat, A. Krassnigg, P. Maris, and C. D. Roberts. Mind the gap. *Eur. Phys. J. A*, 31:630–637, 2007.
- [83] Stanley J. Brodsky, Craig D. Roberts, Robert Shrock, and Peter C. Tandy. New perspectives on the quark condensate. *Phys. Rev. C*, 82:022201, Aug 2010.
- [84] Pieter Maris and Craig D. Roberts. π - and K -meson Bethe-Salpeter amplitudes. *Phys. Rev. C*, 56:3369–3383, Dec 1997.
- [85] Andreas Windisch. Analytic properties of the quark propagator from an effective infrared interaction model. *Phys. Rev. C*, 95:045204, Apr 2017.
- [86] L. Schlessinger and C. Schwartz. Analyticity as a Useful Computation Tool. *Phys. Rev. Lett.*, 16:1173–1174, 1966.
- [87] Leonard Schlessinger. Use of analyticity in the calculation of nonrelativistic scattering amplitudes. *Phys. Rev.*, 167(5):1411, 1968.

- [88] Zhu-Fang Cui, Daniele Binosi, Craig D. Roberts, and Sebastian M. Schmidt. Hadron and light nucleus radii from electron scattering. 4 2022.
- [89] Zhu-Fang Cui, Daniele Binosi, Craig D. Roberts, and Sebastian M. Schmidt. Fresh Extraction of the Proton Charge Radius from Electron Scattering. *Phys. Rev. Lett.*, 127(9):092001, 2021.
- [90] Chueng-Ryong Ji and Pieter Maris. K_{l3} transition form factors. *Phys. Rev. D*, 64:014032, Jun 2001.
- [91] Chen Chen, Lei Chang, Craig D. Roberts, Sebastian M. Schmidt, Shaolong Wan, and David J. Wilson. Features and flaws of a contact interaction treatment of the kaon. *Phys. Rev. C*, 87:045207, Apr 2013.
- [92] Z.-Q. Yao, D. Binosi, Z.-F. Cui, C. D. Roberts, S.-S. Xu, and H.-S. Zong. Semileptonic decays of $D_{(s)}$ mesons. *Phys. Rev. D*, 102:014007, Jul 2020.
- [93] Zhen-Ni Xu, Zhu-Fang Cui, Craig D. Roberts, and Chang Xu. Heavy + light pseudoscalar meson semileptonic transitions. *Eur. Phys. J. C*, 81(12):1105, Dec 2021.
- [94] Lei Chang, I. C. Cloët, J. J. Cobos-Martinez, C. D. Roberts, S. M. Schmidt, and P. C. Tandy. Imaging Dynamical Chiral-Symmetry Breaking: Pion Wave Function on the Light Front. *Phys. Rev. Lett.*, 110:132001, Mar 2013.
- [95] Tanja Horn and Craig D. Roberts. The pion: an enigma within the Standard Model. *J. Phys. G*, 43(7):073001, 2016.
- [96] Jon. A. Bailey, et al. $|V_{ub}|$ from $B \rightarrow \pi \ell \nu$ decays and $(2+1)$ -flavor lattice QCD. *Phys. Rev. D*, 92:014024, Jul 2015.
- [97] Lu Zhang, Xian-Wei Kang, Xin-Heng Guo, Ling-Yun Dai, Tao Luo, and Chao Wang. A comprehensive study on the semileptonic decay of heavy flavor mesons. *Journal of High Energy Physics*, 2021(2):179, Feb 2021.
- [98] Dmitri Melikhov. Dispersion approach to quark-binding effects in weak decays of heavy mesons. *EPJ direct*, 4:1–154, 2002.
- [99] Amand Faessler, Th Gutsche, Mikhail Ivanov, J. Korner, and V. Lyubovitskij. The exclusive rare decays $B \rightarrow K l \bar{l}$ and $B_c \rightarrow D(D^*) l \bar{l}$ in a relativistic quark model. 05 2002.

- [100] D. Ebert, R. N. Faustov, and V. O. Galkin. Weak decays of the B_c meson to B_s and B mesons in the relativistic quark model. *Eur. Phys. J. C*, 32(1):29–43, Dec 2003.
- [101] Patricia Ball and Roman Zwicky. New results on $B \rightarrow \pi, K, \eta$ decay form factors from light-cone sum rules. *Phys. Rev. D*, 71:014015, Jan 2005.
- [102] Alexander Khodjamirian, Thomas Mannel, and Nils Offen. Form factors from light-cone sum rules with B -meson distribution amplitudes. *Phys. Rev. D*, 75:054013, Mar 2007.
- [103] Cai-Dian Lü, Wei Wang, and Zheng-Tao Wei. Heavy-to-light form factors on the light cone. *Phys. Rev. D*, 76:014013, Jul 2007.
- [104] Mikhail A. Ivanov, Jürgen G. Körner, Sergey G. Kovalenko, and Craig D. Roberts. B -meson to light-meson transition form factors. *Phys. Rev. D*, 76:034018, Aug 2007.
- [105] F. Abe, et al. Observation of B_c mesons in $p\bar{p}$ collisions at $\sqrt{s} = 1.8\text{TeV}$. *Phys. Rev. D*, 58:112004, Nov 1998.
- [106] N. Barik, Sk. Naimuddin, P. C. Dash, and Susmita Kar. Semileptonic decays of the B_c meson. *Phys. Rev. D*, 80:074005, Oct 2009.
- [107] Daryl Scora and Nathan Isgur. Semileptonic meson decays in the quark model: An update. *Phys. Rev. D*, 52:2783–2812, Sep 1995.
- [108] I. P. Gouz, V. V. Kiselev, A. K. Likhoded, V. I. Romanovsky, and O. P. Yushchenko. Prospects for the B_c studies at LHCb. *Physics of Atomic Nuclei*, 67(8):1559–1570, Aug 2004.
- [109] J. P. Lees et al. Measurement of an excess of $\bar{B} \rightarrow D^{(*)}\tau^-\bar{\nu}_\tau$ decays and implications for charged Higgs bosons. *Phys. Rev. D*, 88:072012, Oct 2013.
- [110] M. Huschle et al. Measurement of the branching ratio of $\bar{B} \rightarrow D^{(*)}\tau^-\bar{\nu}_\tau$ relative to $\bar{B} \rightarrow D^{(*)}\ell^-\bar{\nu}_\ell$ decays with hadronic tagging at Belle. *Phys. Rev. D*, 92:072014, Oct 2015.
- [111] R. Aaij et al. Measurement of the Ratio of Branching Fractions $\mathcal{B}(\bar{B}^0 \rightarrow D^{*+}\tau^-\bar{\nu}_\tau)/\mathcal{B}(\bar{B}^0 \rightarrow D^{*+}\mu^-\bar{\nu}_\mu)$. *Phys. Rev. Lett.*, 115:111803, Sep 2015.
- [112] Y. Sato et al. Measurement of the branching ratio of $\bar{B}^0 \rightarrow D^{*+}\tau^-\bar{\nu}_\tau$ relative to $\bar{B}^0 \rightarrow D^{*+}\ell^-\bar{\nu}_\ell$ decays with a semileptonic tagging method. *Phys. Rev. D*, 94:072007, Oct 2016.

- [113] S. Hirose et al. Measurement of the τ Lepton Polarization and $R(D^*)$ in the Decay $\bar{B} \rightarrow D^* \tau^- \bar{\nu}_\tau$. *Phys. Rev. Lett.*, 118:211801, May 2017.
- [114] R. Aaij et al. Measurement of the Ratio of the $B^0 \rightarrow D^{*-} \tau^+ \nu_\tau$ and $B^0 \rightarrow D^{*-} \mu^+ \nu_\mu$ Branching Fractions Using Three-Prong τ -Lepton Decays. *Phys. Rev. Lett.*, 120:171802, Apr 2018.
- [115] Roel Aaij et al. Test of lepton universality in beauty-quark decays. 3 2021.
- [116] Noboru Nakanishi. A General Survey of the Theory of the Bethe-Salpeter Equation. *Progress of Theoretical Physics Supplement*, 43:1–81, 01 1969.
- [117] Xue-Qing Hu, Su-Ping Jin, and Zhen-Jun Xiao. Semileptonic decays $B/B_s \rightarrow (D^{(*)}, D_s^{(*)}) l \nu_l$ in the PQCD approach with the lattice QCD input. *Chin. Phys. C*, 44(5):053102, 2020.
- [118] P. Gambino et al. Challenges in semileptonic B decays. *Eur. Phys. J. C*, 80(10):966, 2020.
- [119] G. Eichmann, R. Alkofer, A. Krassnigg, and D. Nicmorus. Nucleon mass from a covariant three-quark Faddeev equation. *Phys. Rev. Lett.*, 104:201601, 2010.
- [120] Si-Xue Qin, Craig D. Roberts, and Sebastian M. Schmidt. Poincaré-covariant analysis of heavy-quark baryons. *Phys. Rev. D*, 97(11):114017, 2018.
- [121] Shu-Sheng Xu, Zhu-Fang Cui, Lei Chang, Joannis Papavassiliou, Craig D. Roberts, and Hong-Shi Zong. New perspective on hybrid mesons. *Eur. Phys. J. A*, 55(7):113, 2019.
- [122] Judd Harrison, Christine T. H. Davies, and Andrew Lytle. $R(J/\psi)$ and $B_c^- \rightarrow J/\psi \ell^- \bar{\nu}_\ell$ Lepton Flavor Universality Violating Observables from Lattice QCD. *Phys. Rev. Lett.*, 125(22):222003, 2020.
- [123] B. Colquhoun, et al. B_c decays from highly improved staggered quarks and NRQCD. *PoS, LATTICE2016*:281, 2016.
- [124] Judd Harrison, Christine T.H. Davies, and Andrew Lytle. $B_c \rightarrow J/\psi$ Form Factors for the full q^2 range from Lattice QCD. *PoS, Beauty2019*:059, 2020.
- [125] Xue-Qing Hu, Su-Ping Jin, and Zhen-Jun Xiao. Semileptonic decays $B_c \rightarrow (\eta_c, J/\psi) l \bar{\nu}_l$ in the "PQCD + Lattice" approach. *Chin. Phys. C*, 44(2):023104, 2020.

- [126] Chien-Thang Tran, Mikhail A. Ivanov, Jürgen G. Körner, and Pietro Santorelli. Implications of new physics in the decays $B_c \rightarrow (J/\psi, \eta_c)\tau\nu$. *Phys. Rev. D*, 97(5):054014, 2018.
- [127] Aidos Issadykov and Mikhail A. Ivanov. The decays $B_c \rightarrow J/\psi + \bar{\ell}\nu_\ell$ and $B_c \rightarrow J/\psi + \pi(K)$ in covariant confined quark model. *Phys. Lett. B*, 783:178–182, 2018.
- [128] Domagoj Leljak, Blazenka Melic, and Monalisa Patra. On lepton flavour universality in semileptonic $B_c \rightarrow \eta_c, J/\psi$ decays. *JHEP*, 05:094, 2019.
- [129] Thomas D. Cohen, Henry Lamm, and Richard F. Lebed. Precision Model-Independent Bounds from Global Analysis of $b \rightarrow c\ell\nu$ Form Factors. *Phys. Rev. D*, 100(9):094503, 2019.
- [130] Fei Gao, Lei Chang, Yu-Xin Liu, Craig D. Roberts, and Sebastian M. Schmidt. Parton distribution amplitudes of light vector mesons. *Phys. Rev. D*, 90(1):014011, 2014.
- [131] Yu. Kalinovsky, K. L. Mitchell, and Craig D. Roberts. $K(l_3)$ and $\pi(e_3)$ transition form-factors. *Phys. Lett. B*, 399:22–28, 1997.
- [132] A. Holl, A. Krassnigg, P. Maris, C. D. Roberts, and S. V. Wright. Electromagnetic properties of ground and excited state pseudoscalar mesons. *Phys. Rev. C*, 71:065204, 2005.
- [133] Daniele P. Anderle et al. Electron-ion collider in China. *Front. Phys. (Beijing)*, 16(6):64701, 2021.
- [134] Zhao-Qian Yao, Daniele Binosi, Zhu-Fang Cui, and Craig D Roberts. Semileptonic $B_c \rightarrow \eta_c, J/\psi$ transitions. *Phys. Lett. B*, 818:136344, 2021.
- [135] P. Gambino. et al. Challenges in semileptonic B decays. *Eur. Phys. J. C*, 80(10):966, 2020.

Acknowledgements

I am greatly indebted to my supervisor Craig D. Roberts, for giving me the opportunity to work with him, sharing his ideas, and supporting me. It was a great pleasure for me to work in INP, which provides an ideal environment for research, and any questions are taken seriously and discussed with great care. I also want to thank Hong-Shi Zong, for giving me help in my early graduate career in Nanjing U. and I deeply regret his untimely death. I would further like to thank Si-Xue Qin and Daniele Binosi, for giving me huge help in my work especially in the aspect of numerical calculations. In addition, I would like to thank Zhu-Fang Cui, Shu-Sheng Xu, Lang-Tian Liu, Ya Lu, Bo-Lin Li, Jin-Li Zhang, Pei-Lin Yin, Hao Zhao and other senior fellow apprentice who gave me a lot of help in my research. My thanks go to Hao-Xuan Gao, Jin-Han Liang and my other fellow students at the physics department. I also would like to thank Zhen-Ni Xu, for the help of my work and this thesis. Last but not least, my thanks go to my parents.

CURRICULUM VITAE

PERSONAL INFORMATION

Name: Zhao-Qian Yao(姚照千)
Date and place of birth: 1995 in Jiangsu, China
Citizenship: China

EDUCATION

Nanjing Normal University, China 9/2013 - 07/2017
Bachelor Degree of Physics

PUBLICATIONS

1. Semileptonic decays of $D_{(s)}$ mesons

Zhao-Qian Yao, Daniele Binosi*, Zhu-Fang Cui, Craig D. Roberts*, Shu-Sheng Xu, Hong Shi Zong

[Phys.Rev.D 102 \(2020\) 1, 014007](#) arXiv:2003.04420v1 [hep-ph] (2020)

2. Semileptonic $B_c \rightarrow \eta_c, J/\psi$ transitions

Zhao-Qian Yao, Daniele Binosi, Zhu-Fang Cui, Craig D. Roberts*

[Phys.Lett.B 818 \(2021\) 136344](#) arXiv:2104.10261v2 [hep-ph] (2021)

3. Vector-meson production and vector meson dominance

Yin-Zhen Xu, Siyang Chen, **Zhao-Qian Yao**, Daniele Binosi, Zhu-Fang Cui, Craig D. Roberts*

[Eur. Phys. J. C \(2021\) 81:895](#) arXiv:2107.03488v1 [hep-ph] (2021)

4. Semileptonic transitions: $B_{(s)} \rightarrow \pi(K); D_s \rightarrow K; D \rightarrow \pi, K$; and $K \rightarrow \pi$

Zhao-Qian Yao, Daniele Binosi, Zhu-Fang Cui, Craig D. Roberts*

[Phys.Lett.B 824 \(2022\) 136793](#) arXiv:2111.06473 [hep-ph] (2021)